University of Alaska

Coastal Marine Institute

Modeling the Circulation of the Chukchi Sea Shelf

Thomas J. Weingartner, Principal Investigator
Tatiana Proshutinsky
University of Alaska Fairbanks

Final Report

June 1998

OCS Study MMS 98-0017

This study was funded in part by the U.S. Department of the Interior, Minerals Management Service (MMS), through Cooperative Agreement No. 14-35-001-30661, Task Order No. 13211, between the MMS, Alaska Outer Continental Shelf Region, and the University of Alaska Fairbanks.

OCS Study MMS 98-0017

Final Report

Modeling the Circulation of the Chukchi Sea

by

Thomas J. Weingartner, Principal Investigator

and

Tatiana Proshutinsky

Institute of Marine Science
University of Alaska Fairbanks
Fairbanks, Alaska 99775-7220

June 1998

Table of Contents

List of Figures

List of Figures (continued)

Abstract

We used a two-dimensional, non-linear, coupled ice-ocean barotropic model to examine the circulation of the northern Bering and Chukchi shelves. The model was run on a grid size of 21 and 7 km and was forced by the mean sea level gradient between the Arctic and Pacific oceans and a proxy surface wind field derived from six-hourly atmospheric pressure fields. The model was integrated for 15 years; using proxy wind fields for the period of January 1981 through December 1996. The mean flow field agrees with historical depictions of the circulation on this shelf and corroborates inferences drawn from more recently obtained observations. For example, the model shows that the mean northward flow through Bering Strait splits along three branches: 1) a flow to the northwest through Hope Valley and Herald Canyon, 2) a northward transport along the depression to the east of Herald Shoal, and 3) a northeastward drift along the northwest Alaskan coast. Flow along the outer shelf is easterly and is strongly influenced by Hanna and Herald shoals. Portions of the flow through Herald Valley veer clockwise around the northern flank of Hanna Shoal and continue eastward where it commingles with waters moving northward along the east flank of Herald Shoal. A portion of this mixture continues northeastward around the north flank of Hanna Shoal while the remainder moves eastward along the southern edge of the shoal. (Both shoals are regions of relatively stagnant flow and could therefore concentrate pollutants.) The latter branch eventually joins with the flow along the northwest Alaskan coast and exits the shelf through Barrow Canyon. Chukchi shelf waters cross the shelfbreak and feed the eastward flowing subsurface boundary current. In winter, the model suggests an alternate circulation pattern that includes southwesterly flow over the northeast shelf and a northward transport through Bering Strait. The latter is diverted northwestward through Herald Valley.

The model also suggests that there is a clockwise circulation around Wrangel Island forced by the mean sea-level difference between the Pacific and Arctic oceans. While current measurements from this area are largely lacking, there are several lines of circumstantial evidence suggesting that this circulation feature is real.

Comparisons between time-dependent, wind-forced modeled currents and observations show that the model performs best in Bering Strait and the northeast Chukchi Sea, but poorly in the western Chukchi Sea. We suggest that the poor disagreement in the western Chukchi Sea is due to the neglect of baroclinic processes (which could be substantial over this part of the shelf) in the model. While the model characterizes the wind-forced variability well, it overestimates the magnitude and duration of wind-forced reversals over the northeast shelf in winter. We suspect that the winds used to force the model overestimate the true winds. Consequently, transit times for water parcels to cross the Chukchi shelf are too long on average.

In spite of these shortcomings, the model is useful in explaining the dynamics of wind-forced reversals over the shelf. These are a consequence of divergence of the Siberian and Alaskan coasts and the interaction between the secular pressure gradient and the wind-induced sea level setdown. In general, this results in alongshore convergence in the vicinity of Cape Lisburne and

the diversion of the strait throughflow towards Herald Valley. Similar arguments are applicable to the wind- and buoyancy-forced Siberian Coastal Current, which turns away from the Siberian Coast in the western Chukchi Sea. The offshore deflection of the Siberian Coastal Current provides one means by which its waters mix with the inflow from Bering Strait. The resulting mixture can be subsequently distributed throughout the Chukchi and Beaufort seas by the flow paths described above. This coastal current transits nearly 2000 km of Siberian coastline before (frequently) terminating in the Chukchi Sea. Consequently it is a potentially important contaminant transport pathway that connects the Laptev and East Siberian shelves with the Alaskan portions of the Chukchi and Beaufort seas.

We recommend that further analyses be performed on comparing various atmospheric pressure fields and the approximations used to approximate the surface winds that force such models.

1. Introduction

The Chukchi Sea is unique among the arctic shelf seas in that its circulation and physical properties are strongly influenced by waters of Pacific Ocean origin. The mean pressure gradient between the Pacific and Arctic Oceans, referred to herein as the secular pressure gradient, forces a northward flow through Bering Strait and across the Chukchi shelf (Shtokman, 1957; Gudkovich, 1961; Coachman and Aagaard, 1966; Coachman *et al.*, 1975; Tiguntsev, 1976; Nikiforov and Shpaikher, 1980; Stigebrandt, 1984). The sea level difference between these two basins in on the order of 10^{-6} and is attributed to the water density difference between the North Pacific Ocean and the Arctic Ocean (Coachman et al., 1975). This pressure gradient is substantial because the mean northward flow persists throughout the year (Weingartner et al., 1998), even though the average winds are northeasterly and tend to establish an opposing flow.

Although the Chukchi shelf is shallow (~ 50 m depth) and flat, the bathymetric relief (Figure 1) is large relative to the total depth; for example, broad areas of Hanna and Herald shoals have depths less than 30 m. Bathymetric variations play a crucial role in "steering" both the mean and varying components of the circulation field. The bathymetry causes a splintering of the Bering Strait throughflow into three branches having distinctly different water mass properties. The differences in water masses and their circulation patterns greatly affect regional productivity patterns and the distribution and abundance of marine organisms (Walsh et al., 1989; Grebmeier, 1993; Grebmeier et al., 1989a; 1989b; 1988). One branch, consisting of the high-salinity, nutrient-rich (Bering Shelf Water) fraction of the inflow through the strait, flows northwestward through Hope Valley and thence northward through Herald Valley in the western part of the basin (Coachman et al., 1975; Walsh et al., 1989; Hansell et al.; 1993). Weingartner et al. (in prep. a) argue that some of this water spreads northeastward around the northern flank of Herald Shoal and thence across the outer part of the Chukchi shelf before entering the Arctic Ocean. A second branch transports the low-salinity and nutrient-poor (Alaska Coastal Water) fraction of the Pacific inflow across the Chukchi shelf (Coachman et al., 1975; Walsh et al., 1989) in a relatively swift coastal current (the Alaska Coastal Current). A third branch carries a mixture of these two water masses northward through the depression to the east of Herald Shoal (Weingartner et al., in prep.a). Some of this flow commingles with water flowing eastward from Herald Valley. North of Herald Shoal the subsurface waters move eastward and appear to be deflected around Hanna Shoal. One portion flows northeastward along the shelfbreak, while a second moves eastward along the southern flank of Hanna Shoal to eventually join the coastal current flowing into Barrow Canyon.

The other important circulation feature of the Chukchi shelf is the Siberian Coastal Current. This current is a wind and density driven coastal current that enters the western Chukchi Sea through Long Strait (Figure 1) and flows southeastward along the Siberian coast. The buoyancy-forcing is supplied by the large freshwater inflows from the Kolyma and Indigirka rivers into the East Siberian Sea and possibly the Lena River into the Laptev Sea (Pavlov et al., 1996).

Flow variations about the mean are large; in some regions the speeds associated with current fluctuations are 5 - 10 times greater than the mean speed. Current variations are primarily forced by the winds (Weingartner et al., 1998; Coachman and Aagaard, 1988; Johnson, 1989) and they tend to be coherent over broad spatial scales (Weingartner et al., 1998; Weingartner et al., in prep. a). Further, the principal axes of the current ellipses are aligned with the local isobaths thereby underscoring the importance of topography in steering the currents.

The emerging circulation description of the Chukchi shelf is based upon limited hydrographic data sets, current meter measurements (which were widely distributed in time and space), and shipboard shipboard acoustic Doppler current profile measurements. In aggregate, the data sets suggest that the flow is primarily barotropic and that the regional circulation dynamics can be economically explored using relatively simple (barotropic and vertically averaged) numerical models. Such models have been applied to the Chukchi Sea in the past (Proshutinsky, 1986, Spaulding et al., 1987, Overland and Roach, 1987). These studies primarily emphasized the flow through Bering Strait and over the southern Chukchi shelf but were less concerned with the flow over the middle and northern portions of the shelf. Because data from the southern Chukchi Sea are relatively abundant compared to the northern Chukchi Sea, we felt a model would be valuable in providing insight into the circulation in these data sparse regions.

2. Methods

2.1 The Two-Dimensional Coupled Ice-Ocean Model

The ocean model is formulated on a stereographic polar coordinate system centered at the North Pole. This system is very similar to a rectangular coordinate system except for the presence of the map coefficient, m, which varies from 1 at the North Pole to 1.071 at 60°N. This coefficient describes a correction from a spherical to a polar stereographic projection. The model is based on the vertically averaged momentum and continuity equations are:

$$\frac{d\mathbf{U}}{dt} + f\mathbf{k}\times\mathbf{U} = -gDm\nabla\zeta + N_h m^2\left(\frac{\partial^2 U}{\partial x^2} + \frac{\partial^2 V}{\partial y^2}\right) + \frac{c\mathbf{T}_i + (1-c)\mathbf{T}_s - \mathbf{T}_b}{\rho} \tag{1}$$

$$\frac{\partial\zeta}{\partial t} = m^2\nabla\left(\frac{\mathbf{U}}{m}\right) \tag{2}$$

In these equations t is time, $\mathbf{U} = u\mathbf{i} + v\mathbf{j}$ is the vertically-averaged horizontal velocity vector, f is the Coriolis parameter, g is gravity, ρ is water density, ζ is the sea surface elevation, $D = (H + \zeta)$ is the total water depth and $\mathbf{k}$ is the unit vector in the vertical direction. Lateral friction is parameterized by the Laplacian of the horizontal velocity vector multiplied by a constant horizontal eddy viscosity coefficient ($N_h = 5 \times 10^5$ m^2 s^{-1}). This value for N_h is close to the threshold of numerical stability $N_h = 5 \times 10^4$ m^2 s^{-1} (Kowalik, 1981). Momentum is transferred vertically through stresses between the ice and water $\mathbf{T}_i$, the atmosphere and the water, $\mathbf{T}_s$, and

from the water column to the sea bottom, $\mathbf{T_b}$. The variable c, which ranges from 0 to1, denotes the ice concentration within the grid element.
The sea ice model contains an analogous set of equations for the momentum balance and for mass conservation are:

$$\frac{d\mathbf{u}_i}{dt} + f\mathbf{k}\times\mathbf{u}_i = -gDm\nabla\zeta + \frac{\mathbf{T}_{is} - \mathbf{T}_i}{\rho_i h_i} + \mathbf{F}_i \tag{3}$$

Here $\mathbf{u}_i$ is the ice velocity vector, h_i, is the ice thickness, $\mathbf{T}_{is}$, is the vector describing the stress

$$\frac{\partial c}{\partial t} = -m^2\nabla\left(\frac{\mathbf{u}_i c}{m}\right) \tag{4}$$

between the atmosphere and sea ice, $\mathbf{F}_i$, is the internal ice force vector. In equations 1 and 3 the operator, $\frac{d}{dt} = \frac{\partial}{\partial t} + m\left[\frac{U\partial}{D\partial x} + \frac{V\partial}{D\partial y}\right]$
The stress between the atmosphere and the ocean is defined to be:

$$\mathbf{T_S} = \rho_a R_a \mathbf{W}|\mathbf{W}| \tag{5}$$

where $\mathbf{W}$ is the surface wind vector, ρ_a is air density, and R_a is the drag coefficient. Following Proshutinsky (1978, 1986, 1993), the drag coefficient depends upon the wind speed accordingly: $R_a = (1.1 + 0.04|\mathbf{W}|) \times 10^{-3}$. The surface wind was determined from the geostrophic wind after applying empirical corrections to approximate the winds in the atmospheric boundary layer. These corrections involve a reduction in the geostrophic wind speed given by C_a, and a rotation of the geostrophic wind vector through the veering angle A_a. Following Proshutinsky (1978, 1986, 1993), the corrections are dependent upon the geostrophic wind speed ($|\mathbf{W}_g|$) accordingly:

$C_a = 0.7$ and $A_a = 30^o$ (counterclockwise) if $|\mathbf{W}_g| < 15$ m s^{-1} and
$C_a = 0.8$ and $A_a = 20^o$ (counterclockwise) if $|\mathbf{W}_g| > 15$ m s^{-1}.

Bottom stress is prescribed to be:

$$\mathbf{T_b} = \rho R_b|\mathbf{U}|\mathbf{U}/D^2 \tag{6}$$

with the bottom drag coefficient $R_a = 2.6 \times 10^{-3}$. The vector describing the stress between the atmosphere and the ice is:

$$\mathbf{T}_{is} = \rho_a R_{ia}|\mathbf{W}|\mathbf{W} \tag{7}$$

with the ice-atmosphere drag coefficient R_{ia}, assumed equal to the air-water drag coefficient R_a. The vector describing the stress between the ice and water is:

$$\mathbf{T}_i = \rho R_i|\mathbf{u}_i - \mathbf{U}/D|(\mathbf{u}_i - \mathbf{U}/D) \tag{8}$$

with the ice-water drag coefficient $R_i = 5.5 \times 10^{-3}$ following McPhee (1980).

The internal ice force vector, $\mathbf{F}_i$, follows the nonlinear, viscous constitutive law proposed by Rothrock (1975):

$$\mathbf{F}_i = \eta m^2 \nabla^2 \mathbf{u}_i + \Lambda m^2 \nabla(\nabla \mathbf{u}_i) - m \nabla p \qquad (9)$$

where the bulk viscosity ( ) and the shear viscosity (η) equals 10^3 m^2 s^{-1}. Rothrock (1975) suggested that the tensile stress in ice is negligible compared to compressive stress so that the pressure, p, in equation 9 is given by:

$$p = -A_p m \nabla \mathbf{u}_i \text{ if } \nabla \mathbf{u}_i < 0, \text{ and } p = 0 \text{ if } \nabla \mathbf{u}_i \geq 0 \qquad (10)$$

where $A_p = 10^4$ m^2 s^{-1} is the ice pressure coefficient. Note that this ice model does not provide for thermodynamic effects so ice growth and ice melting cannot occur.

The particle paths are determined from the Lagrangian velocity. At an initial time ($t = t_0$) the particle is at a point $\mathbf{r}_o$ and at a later time ($t = t_1$) its new position is $\mathbf{r}_o + d\mathbf{r}$. To first order the particle velocity is given by:

$$\frac{d\mathbf{r}}{dt} = \mathbf{u}(\mathbf{r},t) = \mathbf{u}(\mathbf{r}_o,t) + \frac{\partial \mathbf{u}}{\partial \mathbf{r}} \cdot d\mathbf{r} \qquad (11)$$

Because, $d\mathbf{r} = \int_{t_o}^{t_1} \mathbf{u}(\mathbf{r}_o,t)dt$, equation 11 can be written as,

$$\frac{d\mathbf{r}}{dt} = \mathbf{u}(\mathbf{r},t) = \mathbf{u}(\mathbf{r}_o,t) + \frac{\partial \mathbf{u}}{\partial \mathbf{r}} \cdot \int_{t_o}^{t_1} \mathbf{u}(\mathbf{r}_o,t)dt \qquad (12)$$

From (12), the Lagrangian velocity is defined as the superposition of the Eulerian velocity and a Stokes velocity. That is, $\mathbf{u}_L = \mathbf{u}_E + \mathbf{u}_S$, where $\mathbf{u}_E = \mathbf{u}(\mathbf{r}_o,t)$ and $\mathbf{u}_S = \frac{\partial \mathbf{u}}{\partial \mathbf{r}} \cdot \int_{t_o}^{t_1} \mathbf{u}(\mathbf{r}_o,t)dt$. The change in horizontal position of a specified particle is computed as:

$$dx = udt + 0.5(u\frac{\partial u}{\partial x} + v\frac{\partial u}{\partial y})(dt)^2 \qquad (13)$$

$$dy = vdt + 0.5(u\frac{\partial v}{\partial x} + v\frac{\partial v}{\partial y})(dt)^2 \qquad (14)$$

where (x,y) are the horizontal coordinate axes and (u,v) are the velocity components along these axes. The velocities at the particle position are estimated by bilinear interpolation. Displacements are computed at each model time step (~10 min.).

Figure 3 shows the computational domain. The bathymetry is based on Russian and US navigation charts and supplemented with US Navy supplied ETOPO5 data. The model was run using both a 21-km and 7-km grid size. The former was obtained by subsampling the 14 km spatial grid and bathymetry prepared by Kowalik and Proshutinsky (1994). The bathymetry for the 7-km grid spacing was obtained by digitizing navigation charts in regions of high bathymetric change. In many areas of the model domain the bathymetric data on these scales are lacking and so depths were interpolated. However, the bathymetric data coverage for the Chukchi Sea is considerably better than elsewhere in the Arctic Ocean portion of the model domain.

Initial conditions are that ζ, U, and u_i are set equal to zero throughout the integration domain. The boundary conditions along the (solid) coasts are U = 0 and $u_i = 0$. Along the southern (open) boundary in the Bering Sea, we prescribe the sea level $\zeta_o = (x,y,t) = 1.0$ m for the model with a 21 km grid and $\zeta_o = 0.5$ m for the model using the 7 km grid. These values force a transport (in the absence of any wind forcing) of about 1.0 Sv (1 Sv = 1 Sverdrup = 10^6 m^3 s^{-1}) northward through Bering Strait. Note that the most recent estimate, based on observations, of the long-term mean transport is 0.8 Sv (Roach et al., 1995). Of course, this estimate includes the effects of the winds, which are southward on average and oppose the mean northward flow. Hence our choice of a secular sea level gradient that forces a northward flow of 1.0 Sv in the absence of winds is reasonable. As will be shown the model-predicted transport under the influence of winds agrees quite well with the observations. Note also that, the qualitative behavior of the model does not change if a different secular pressure gradients are imposed. A radiation condition is prescribed at the northern open boundaries (e.g., $\mathbf{U} = \pm \zeta_{in}(gH)^{1/2}$; where ζ_{in} is sea level along the first line parallel to the open boundary). At the open boundaries the conditions on the ice cover are: $\partial \mathbf{u}_i / \partial n = \partial c / \partial n = 0$; where n is normal to the open boundary.

In ice-free areas, equations (1) and (2) are solved subject to the boundary conditions at the surface (5) and bottom (6) with $\mathbf{T}_i = 0$ and $c = 0$. Elsewhere the full system of equations is used. We have also prescribed the ice concentration and thickness as external parameters using data from the NAVY-NOAA Joint Ice Center, Naval Polar Oceanography Center, Suitland.

The model domain includes the shelves of the East Siberian Sea and the Mackenzie sector of the Beaufort Sea. Both regions receive large volumes of river discharge. This discharge is a source of buoyancy forcing for the shelf resulting in the formation of cross-shelf density gradients. Because the model treats density as a constant everywhere, these baroclinic processes cannot be represented. Instead, the river inflow is specified as a time-varying volume flux on the East Siberian Sea shelf at the location of the Kolyma River and on the Beaufort Sea shelf at the location of the Mackenzie River. This inflow causes a barotropic flow and sea-level slope whose dynamical balance consists of friction, Coriolis, pressure (sea-level gradient) and inertial forces. This representation of the river inflow is a gross over-simplification and the neglect of these baroclinic effects causes several inaccuracies discussed below. While retained in the model results shown here, the modeled Chukchi Sea circulation differed very little between model runs with and without the "runoff" prescribed here.

The model is forced by winds generated from the surface atmospheric pressure fields predicted from forecast models run by the US Navy's Fleet Numerical Meteorology and Oceanography Center (FNMOC). These fields are generated every six hours onto a 2.5 degree grid. The geostrophic winds were computed from these pressure fields and then corrected for as described above.

We ran the model for 15 years after allowing one month for it to spin up. We present the results in a traditional manner (figures and tables) and by means of a video that shows the modeled mean monthly current vectors for each month between January 1981 and December 1995. The

results shown in the video are best appreciated after reading the results presented below. (A copy of the video was provided to MMS with the Final Report).

3. Results

3.1 Steady-State Circulation

We first present model results obtained for forcing by the secular pressure gradient only and without any ice. This approach serves as a basis for understanding the wind-induced circulation, which modifies the background (or steady state) circulation field. We begin by discussing several broad features of this model run and then compare mean current vectors based on measurements and this steady state flow field.

Figure 4 shows isopleths of sea level, the mean current vector from the model (dashed arrows) and the mean observed current vector (solid arrows). Under steady state conditions the isopleths are streamlines and trajectory paths so that the flow at a particular point is also parallel to the streamline. Figure 5 is the companion plot showing the current vectors for the steady state circulation field. (Both of these figures are based on the 7 km grid.) Note that current speeds are inversely proportional to the horizontal distance between contours of the sea surface elevation. The flow is swiftest in Bering Strait and Barrow Canyon where the sea surface elevation contours are closely packed. Comparing Figure 4 with Figure 1 shows that the isopleths of sea surface elevation approximately parallel the isobaths. This tendency is a consequence of barotropic geostrophic flow (Pedlosky, 1987) and implies that the nonlinear and friction terms in equation 1 are small over much of the model domain.

One important implication of this result is that the transport through Bering Strait is geostrophically controlled (Toulany and Garrett, 1984) such that $Q = gD\Delta\zeta/f$, where Q is the mass transport and $\Delta\zeta$ is the cross-strait sea level difference. (If the flow through the strait is geostrophically controlled then the sea-level difference across the strait cannot exceed the sea level difference between the Pacific and Arctic oceans. Figure 4 shows that this situation holds.) This result also implies that friction and nonlinear terms are relatively unimportant in Bering Strait dynamics. We assess the significance of both of these. Following Toulany and Garrett (1984) the ratio of the Bernoulli setdown, $B = 0.5u^2/g$, (associated with the nonlinear acceleration terms in the strait) to the sea surface elevation difference, $\Delta\zeta$, (which drives the flow through the strait) between the two basins is: $B/\Delta\zeta = 0.5gh(Wf)^{-2}(\Delta\zeta/h)$. For $\Delta\zeta \sim 0.5$ - 1.0 m this ratio is about .04 - .08, indicating that the non-linear terms are unimportant in the strait momentum balance. Similarly the Rossby number, $R_O = U/fL$, where L is the width of the strait (80 km), for current speeds of 1 m s^{-1} is ~0.1. We can define a frictional time scale as $\lambda = (L/W)R_b|\mathbf{U}|/D$, where L and W are the length and width of the strait both set equal to 80 km. For typical current speeds ($|\mathbf{U}| = 0.25$ m s^{-1}) and $D = 50$ m, then $\lambda = 5 \times 10^{-5}$ s^{-1}, which is a factor of 7 smaller than f. However wind-driven flows can be as large as 1.0 m s^{-1} (Roach et al., 1995) such

that $\lambda/f \sim 0.5$. Hence at high current speeds bottom friction is important in the strait momentum balance. Our finding that the flow is geostrophically controlled agrees with that of Overland and Roach (1987). In principle, the results imply that the transport through Bering Strait could be monitored using two pressure gauges; one deployed on the western side and the other on the eastern side of the strait. While our results agree with those of Overland and Roach, Spaulding et al. (1987) state that transport through the strait is not geostrophically controlled. However, it is not clear on what basis they make this claim.

Note from Figure 4 that north of Bering Strait the secular sea level gradient between Alaska and Siberia diminishes as the distance between these coasts increases. This decrease is a consequence of the continuity equation (and geostrophic control) and it has important implications for the wind-induced circulation. As we will show northerly winds must increase in strength from the northern to the southern Chukchi Sea for southerly flow to occur over the whole shelf. The divergence of the coastlines also has consequences for the Siberian Coastal Current; this current will encounter an increasingly adverse pressure gradient as it flow southeastward along the Siberian coast. Indeed, the model suggest that the cross-shore (secular) sea level gradient, as measured within 100 km of the Siberian coast, increases by an order of magnitude between Long Strait and Bering Strait. If the magnitude of the wind- and buoyancy-induced pressure gradients that force the southeastward flowing Siberian Coastal Current are not large enough to overcome the effects of the secular pressure gradient, then this current will be blocked at some point and it will turn offshore (retroflect). These competing effects are one reason why the Siberian Coastal Current is prevented from flowing onto the northern Bering shelf (Weingartner et al., in prep.b).

The isopleths of sea level south of Bering Strait show that the gradient across Anadyr Strait is about 2.5 times larger than the gradient across Shpanberg Strait. Since the transports through these straits are proportional to these gradients, the results imply that the flow through Anadyr Strait contributes about 70% of the transport that feeds Bering Strait. Overland and Roach (1987) reached a similar conclusion based on their model results. Note that sea level isopleths and the flow emanating from Anadyr Strait trend eastward across the north coast of St. Lawrence Island before bending northward to Bering Strait. This tendency is also reflected in hydrography (Gawarkiewicz et al., 1994) and a single drifter track (Overland et al., 1996).

North of Bering Strait, sea level isopleths extend northward to about 70°N and then trend eastward across the outer shelf. Note how the 20 cm isopleth swings clockwise around the northeast corner of Herald Shoal while the 10 cm isopleth behaves similarly around the northeast side of Hanna Shoal. Figure 5 shows that the velocities are relatively weak over these bathymetric features. Martin and Drucker (1997) showed that ice tends to circulate clockwise around these shoals and they argued that these were regions of Taylor column formation. Weingartner et al. (in prep. a) compiled hydrography, moored current meter, and shipboard acoustic Doppler current profiler data and showed an apparent clockwise circulation around the northern flanks of both shoals. They also showed that water remnant from the previous winter persists over these shoals well into summer and early fall even though adjacent regions are well-flushed with summer water. These various observations support the model results and imply that pollutants would tend to be trapped over these shoal regions.

The sea level isopleths extend eastward (and imply eastward flow) along the Chukchi and Alaskan Beaufort shelfbreak. Although the surface flow (e.g., < 50 m depth) here is westward on average, the subsurface flow along the slope and outer shelf is eastward in the mean (Aagaard et al., 1989). This subsurface flow is composed of both water of Bering Sea and Atlantic Ocean origin (Carmack, 1986) and comprises the circumpolar boundary current. The Atlantic water enters the Arctic Ocean through Fram Strait and across the Barents Sea shelf and then proceeds counterclockwise around the Arctic Ocean. Bering Sea water joins this current and is eventually carried along the continental slope north of Greenland where it enters the Atlantic Ocean through Fram Strait (Newton and Sotirin, 1997). The dynamics of this boundary current are not well-understood and such a study is beyond the scope of this model. However, our results clearly imply that the flow through Bering Strait can influence the dynamics of this current. We will speculate on this issue later.

The steady state circulation depicts a northwesterly flow along the Siberian coast in the western Chukchi Sea. This flow enters the East Siberian Sea through Long Strait, continues clockwise around Wrangel Island, and then feeds the relatively weak southward flow along the west wall of Herald Valley. The model suggests that some of this southward flow converges with water moving northward through Herald Valley. There are few direct measurements to corroborate the flow around Wrangel Island but there are several lines of circumstantial evidence that lend some credence to the model results. First, some Russian atlases do suggest that there is a clockwise circulation around the north shore of Wrangel Island (Pavlov; 1996). Second, there is geochemical evidence that Bering Shelf water is carried into the East Siberian Sea (Codispoti and Richards, 1968). Third, the observed flow within Herald Valley is strongly sheared horizontally; swift northward flow along the east flank separates weak northward or even southward flow along the west wall (Weingartner et al., in prep.a; Aagaard et al., pers. comm.). Moreover, the water masses on either side of the canyon are distinctly different from one another (Weingartner et al., in prep.a; Aagaard et al., pers. comm.). In fall, water along the east wall of the canyon is relatively warm attesting to its recent arrival from the Bering Sea. However, water along the west wall of the canyon is enriched in silica but its temperatures are at or near the freezing point. The high silica content but low temperatures suggest these waters are of Bering Sea origin but have spent at least one winter on the shelf. In the western Chukchi Sea such waters are often found adjacent to Wrangel Island (Coachman et al., 1975; Coachman and Shigaev, 1992 ; Münchow et al., submitted, Weingartner et al., in prep. b).

Figure 6 shows the steady state circulation using a 21 km grid field. While the gross characteristics of the shelf circulation are evident with this resolution, many of the finer scale circulation aspects discussed above are obscured using the coarser grid. In particular the 21 km grid fails to capture the detailed structure of the flow around Hanna and Herald shoals and the clockwise circulation about Wrangel Island. For each of these regions we believe that there are observations which tend to corroborate the model results. Moreover, the high resolution model results suggest that pollutants would have a tendency to be trapped about these region features because of the local bathymetric influence on the circulation field. We would probably not have reached this conclusion using the results of the model with a 21-km grid scale.

3.2 Comparison of Observed and Simulated Currents

The preceding discussion included a qualitative comparison of the model with observations. Here we provide a more quantitative comparison beginning with a comparison of the observed and modeled mean vectors shown in Figure 4. Overall there is generally good agreement between the observed (solid arrows) and modeled mean vectors (dashed arrows) with respect to magnitude and direction. The flow is weak (< 5 cm s^{-1}) over most of the model domain but in channels or canyons it is strong. For example the mean currents in Bering Strait and Barrow Canyon are about 30 cm s^{-1} while those in Herald Valley and along the east flank of Herald Shoal are about 10 - 15 cm s^{-1}. There are discrepancies in vector orientation in topographically complicated regions (Bering Strait, Herald and Barrow canyons). These are most likely related to discretization errors in the gridded bathymetry. In other regions the discrepancies are due to the absence of important physics in the model. For example, the simulated flow along the Siberian coast northwest of Bering Strait is strong and to the northwest while the observed mean flow is negligible. Baroclinic effects associated with the Siberian Coastal Current influence currents at this mooring. These include a southwestward flow tendency forced by cross-shore density gradients and baroclinic instability of the coastal current (Weingartner et al., in prep. b). Thus the discrepancy between the model and observed results must is partly due to the neglect of baroclinic processes in the model.

The final point to emphasize in this comparison is that while the modeled vectors are based upon forcing solely by the secular pressure gradient the observed vectors include the integrated effects of the wind over the (one-year) deployment period. The reason for this choice in comparison is that the mean annual currents from the model with wind-forcing are small in comparison with the observed currents. We believe that the winds used in this study over estimate the real wind field and give rise to prolonged and frequent current reversals in the model in winter. However, the comparison of the observations with the results of the model run without wind forcing suggests that the annual observed mean field is predominantly a reflection of forcing by the secular pressure gradient. Indeed, this appears to be the case as shown by Weingartner et al. (1998).

Statistical comparison of the time series of modeled and observed currents are summarized by the correlation coefficients shown in Table 1 and by comparison time series plots of the observed and modeled time series shown in Figures 7 through 22. The figures include both velocity components with the modeled currents derived from the 21 km (upper panel of each figure) and the 7 km grid (lower panel of each figure). In viewing these comparisons it must be remembered that the current measurements are made at one depth (usually within 10 m of the bottom) whereas the modeled currents represent those averaged over the whole water column. In constructing these comparisons we selected model data from the grid point closest to the current meter location. In most cases, this makes very little difference in the results. However, in regions of rapidly varying bathymetry (Barrow Canyon and Herald Canyon) the current field can change substantially over the distance of a grid cell. In most cases the results from the 7 km grid are better than those obtained using the 21 km grid. although the improvement in the correlation coefficient is not statistically significant at the 95% confidence level. Overall, the correlation between the observed currents and those from the 7 km grid model indicate that in most places

from 35-65% of the observed variance is explained by the model. This fraction of explained variance is about the same as obtained by directly correlating the winds with the currents (Weingartner et al., 1998). The magnitudes of the observed currents agree much better with the currents modeled using the 7 km gird than with those obtained from the 21 km grid. The best agreement (in terms of the magnitude of the correlation coefficient) between the model and observations occurs in Bering Strait and Barrow Canyon where the current signals are enhanced due to the relatively strait and narrow topography.

Overall the correlations are higher in the eastern Chukchi Sea than on the western shelf. Indeed the lowest correlations are at moorings mc190, mc290, me290, and mf290 which are all in the western Chukchi Sea. The poor agreement for mc190 and mc290 is very likely due to baroclinic processes associated with the Siberian Coastal Current. Weingartner et al., (in prep. b) shows that highly energetic eddies and squirts are shed due to baroclinic instability of this coastal current. They show that even under calm conditions that the current speeds associated with these features can be equal 50 cm s^{-1}. Currents of this magnitude occur under strong wind-forcing elsewhere on the shelf. Baroclinic effects associated with the Siberian Coastal Current also influence moorings me290 along the south coast of Wrangel Island and in Long Strait. Further, a polynya often forms along the south cost of Wrangel Island in winter in which strong baroclinic forcing associated with dense water production possibly occurs (Gawarkiwiecz and Chapman, 1995). Finally currents at mooring mf290 on the west wall of Herald Valley are also poorly correlated with those from the model. Again baroclinic processes might be involved here as there is a large density gradient across this canyon in fall (Weingartner et al., in prep. A) and in winter (Aagaard, pers. comm.).

Table 1.Correlation between observed and modeled currents. (U is the east-west current component and V is the north-south current component. The critical value of the correlation coefficient at the 95% significance level is ~.22 for 80 degrees of freedom. The latter is based on an integral time scale of about 5 days as determined from the current meter records. Italicized correlation coefficients indicate that more than 75% of the observed total current variance is accounted for by this component.)

Mooring Identifier	Latitude	Longitude	Meter Depth/ Bottom depth	Beginning date	Ending Date	r for U 21km/7km	r for V 21km/7km
Bering Strait							
BSE	65.78	-168.60	45/53	9/28/91	9/20/92	.06/.10	*.63/.76*
BSN	66.30	-169.98	45/53	9/28/91	9/22/92	-.49/-.12	*.65/.78*
MA190	65.95	-169.42	41/50	9/25/90	9/23/91	-.62/.74	*.59/.69*
MA290	65.77	-168.58	44/52	9/11/90	9/15/91	-.33/.40	*.70/.76*
MA390	66.29	-168.95	47/58	9/5/90	9/4/91	-.56/.51	*.83/.88*
Barrow Canyon							
AP18	71.33	-158.17	117/122	10/1/91	9/31/92	.79/.82	.77/.79
BP12	71.05	-159.55	82/85	10/1/91	9/4/92	.79/.83	.63/-.53
MK190	71.03	-159.69	71/79	9/17/90	9/21/91	.66/.75	.55/-.60
Cape Lisburne							
EP3	69.02	-166.97	42/45	9/29/91	9/23/92	-.11/-.09	*.65/.66*
MC690	69.02	-166.95	38/45	9/9/90	9/21/91	.12/.11	*.64/.62*
Hope Sea Valley							
MC490	68.85	-169.59	44/52	9/23/90	9/3/91	.15/.52	*.58/.63*
MC390	68.60	-171.07	47/54	9/23/90	9/24/91	.24/.45	.45/.60
MC290	68.33	-172.49	42/50	9/23/90	9/18/91	.22/.41	.02/.10
MC190	67.94	-174.55	35/42	9/23/90	10/4/91	.37/.40	.31/.36
South Coast Wrangel Island							
ME290	70.49	-178.44	37/44	9/21/90	9/29/91	.48/.05	0.0/.26
Herald Valley							
MF290	70.95	-174.18	40/48	9/22/90	9/29/91	.18/.22	-.12/-.07
East Flank Herald Shoal							
CP3	70.67	-167.03	49/54	10/2/91	9/27/92	0.0/.01	*.60/.59*

3.3 Time-Dependent Variations

We will illustrate the temporal variability in the model by means of plots of the monthly mean circulation. These not only provide the basis for our description of the annual cycle, but they also mimic circulation modes that vary on synoptic time scales as well. Prior to describing temporal variations annual cycle in the circulation field, we summarize aspects of the wind field upon which the circulation depends. Furey (1996) reviewed the statistical properties of the FNMOC-derived surface wind field between 145°E and 130°W (essentially the longitudinal extent of our the arctic portion of the model domain used here). He focused on the wind field along 72.5°N, thus his results apply to the East Siberian, northern Chukchi, and Beaufort seas. Winds are northeasterly over this whole region. Mean monthly wind speeds and monthly wind speed variability are largest in late fall and winter. In all months, these variables are largest in the northeast Chukchi Sea and smallest in the East Siberian Sea. Winds are polarized in the east-west direction and the polarization is a maximum in winter and over the Chukchi and Beaufort shelves. Winds are only weakly polarized in summer and over the East Siberian Sea. These patterns of spatial and temporal variability reflect the tendency for low pressure systems to propagate northeastward from the Bering Sea to the Beaufort Sea (Overland and Pease; 1982). Similar seasonal transitions in these wind field properties occur over the southern Chukchi and northern Bering shelf (Brower et al., 1988). However, wind speeds over this region are larger than those further north and the directions tend to be more northerly than northeasterly. Because of the wind has much greater variability in fall and winter than summer, interannual variations in the wind field are primarily dictated by the fall and winter wind field.

We begin our discussion of the annual cycle by consideration the model-predicted mean monthly transports in Bering Strait. These means are derived from the 15 year model integration and shown in Figure 23. On average the transport is northward in all months of the year with a maximum of about 1.4 Sv in June and a minimum of 0.4 Sv in January. The model annual cycle is similar to that estimated from winds by Coachman and Aagaard (1988) although our maximum transport is higher and our minimum transport is lower than their estimates. The differences might be related to our wind estimates and/or a model artifact. However, they could also be real because the Coachman and Aagaard (1988) estimate is based on wind data for the period of 1946 - 1982 while our results are based on the winds since 1981. Figure 24 shows the mean transport for each month of the 15 year integration period. The results provide an idea of the range in monthly transports during this period. There is a distinct annual cycle evident in each year. Note that the range in the summertime transport maxima is narrow and between 1.3 - 1.6 Sv while the range in winter transport minima is large. The latter varies from -0.7 Sv (February 1985) to 0.5 (March 1994). Figure 25 is a plot of the mean daily transport over this same time period and it shows that transport variations can range from -3 and +3 Sv on time scales of days to weeks. All of these features of the model are reflected in the observations discussed by Roach et al. (1995). The broader range of transports in winter compared to summer reflects the higher variability of the wind field in this season. The reduction in northward transport in winter is due to the strong northerly winds which set up a sea-level (pressure) field that opposes the secular pressure gradient.

Figures 26 through 29 show the mean January, May, August, and November circulation field over the northern Bering and Chukchi seas. These maps were computed by averaging the monthly circulation field over the 15-year integration period of the model. These figures include the sea surface elevation field (black contours) and the atmospheric pressure field upon which the wind fields are dependent (color-shaded contours). These figures were constructed using the 21 km grid model and the vectors are shown at every third grid point for clarity of presentation. The video results are displayed in a manner similar to these figures.

The model annual cycle on the Chukchi Sea shelf suggests two circulation modes that vary seasonally. In winter and fall (Figures 26, 27, and 29), the flow is relatively steady and northward in the western Chukchi Sea (e.g., toward the Arctic Ocean) and weak or southwesterly in the northeastern Chukchi Sea. By contrast, in summer (Figure 28) the circulation on the shelf clearly resembles the steady state circulation shown in Figure 5 in which there is outflow through both Herald Valley and Barrow Canyon. Weingartner et al., (1998) inferred that the winter pattern lasted for 1.5 months in the winter of 1991/92. Other current meter records from Barrow Canyon (Aagaard, 1988; Aagaard and Roach, 1989; Weingartner, unpub. data) suggest that the reversals in the northeast Chukchi Sea are not so long-lived. The 15-year composited results suggest that the reversals last for several months in the winter (November - April). As a consequence the model captures the flow variations reasonably well but underestimates the mean flow. Particle trajectory maps and calculations show that particles released in Bering Strait in January will take about 7 months to reach Barrow Canyon while particles released in July require only about 3 months. The latter estimate is much closer to the 2.5 months estimated by Weingartner et al. (1998). Their estimate was based on tracking the arrival time of warm water flowing northward from the Bering Sea in summer and so it is biased toward summer conditions. The model predicted advective time scale for a parcel between Being Strait and Herald Valley is shorter; about 5 months for a parcel leaving Bering Strait in January and 3 months if it leaves in July. We used unpublished temperature time series data from Herald Valley to estimate an advective time scale between Bering Strait and Herald Valley. This was done as mentioned above and yields a time scale of about 3 months in agreement with the summer transit time given by the model. There is reasonably good agreement between the model and observations in the summer when winds are weak. However, we believe that our winter winds consistently overestimate the real wind field and thus lead to more frequent and prolonged reversals in the northeast Chukchi Sea.

While the duration of the current reversals predicted by the model appear to be too long, they do occur and the model is helpful in discerning the dynamics responsible for them. The low-frequency basin-wide circulation adjustments depends upon the evolution of the shelf-wide net (wind-induced plus secular) sea level gradient. North of Bering Strait the secular sea level gradient between Alaska and Siberia diminishes as the distance between these coasts increases. The model shows that this decrease occurs rapidly near Cape Lisburne (see Figure 4 and Figures 26 - 29). For the coastal flow to locally reverse, the sea level setup by northeasterly winds along the northwest Alaskan coast must be greater than the secular gradient here. To effect a complete current reversal from Barrow Canyon to Bering Strait the alongshore wind speeds must be large everywhere or increase from the northern Chukchi Sea to Bering Strait. For example, Weingartner et al. (1998) suggested that current reversals in Barrow Canyon occurred for northeasterly winds exceeding 6 m s^{-1} and Coachman (1993) suggested that the flow in Bering

Strait would reverse if local wind speeds were greater than 8 m s^{-1}. If the wind speeds over the southern Chukchi Sea are less than ~8 m s^{-1}, we would expect a transition region of negligible net sea level gradient to be established between the northern and southern portions of the shelf. North of this transition zone the net sea level gradient is dominated by the wind setup and southerly flow is established. South of the transition zone the net sea level gradient is dominated by the secular pressure gradient and northerly flow is maintained. The alongshore flow will be convergent on either side of the transition zone. Just such a transition zone separates the southward coastal flow on the northeast shelf from northwestward flow on the southern shelf. As seen in Figures 26, 27, and 29, the transition zone occurs in the vicinity of Cape Lisburne. The model result supports the conclusion of Weingartner et al. (1998), which was based on data from a limited number of current meter moorings. Because of the convergence in the vicinity of Cape Lisburne, the transport through Bering Strait is diverted northwestward through Hope Valley and exits the Chukchi Sea through Herald Valley. Hence under these conditions the outflow into the Arctic Ocean proceeds along a single branch rather than three branches.

The strong northeasterly winds that force these current reversals are also responsible for the formation of coastal polynyas along the northwest coast of Alaska (Weingartner et al., 1998). These are areas of vigorous ice production where up to 20 cm day^{-1} of ice grows (Cavalieri and Martin, 1994). Salt rapidly drains from this newly formed ice and increases the salinity of the seawater from which the ice grows. Ice production leads to the formation of dense (cold, salty) shelf water. Strong horizontal density gradients are created along the polynya boundary that can force a vigorous baroclinic circulation (Gawarkiewicz and Chapman, 1995; Weingartner et al., in prep. a), because the density of the polynya waters is much greater than the shelf water outside the polynya boundaries (but at the same depth). (Note that such effects cannot be considered with the barotropic model used here. Moreover, the dense water formed in winter on the shelf is usually much denser than the water along the shelfbreak and slope. As it flows off the shelf it sinks to contribute to the subsurface waters of the Arctic Ocean. This process is important to the thermohaline structure of the Arctic Ocean (Aagaard et al., 1981)).

The formation and subsequent transport of this dense shelf water mass is probably enhanced by the weakening of the circulation on the northeast shelf for several reasons. First, according to Coachman et al. (1975) and Roach et al. (1995) freshwater content on the northern Bering shelf increases from May through September, but is completely flushed by late December. Thus, the late fall diversion of the Bering Strait transport through Hope Valley implies that some of this freshwater is prevented from reaching the northeast shelf. This leads to higher fall salinities along the northwest coast of Alaska. Second, because of the weakened circulation along the northwest cost of Alaska, the salt rejected from sea ice produced within the polynyas accumulates within the same reservoir of shelf water throughout the period of maximum ice production. The first two points are analogous to Melling's (1993) suggestion that dense water production on the Mackenzie portion of the Beaufort Sea shelf requires a two-step process in which wind-driven circulation elevates shelf salinities in fall (before freeze-up) and prolongs shelf water residence time in winter. Finally, the alongshore convergence in the vicinity of Cape Lisburne results in a compensatory offshore flow that should advect the dense water formed along the coast into the central Chukchi Sea. Indeed, Weingartner et al. (1998) and Weingartner et al. (in prep. a) observed dense water masses on the central Chukchi shelf (between Herald and

Hanna shoals) far from the coastal polynyas. As a consequence of the shelf-wide circulation pattern influence the salinity of the dense water formed and the trajectory that this water follows en route to the Arctic Ocean.

The wind-driven basin-wide circulation variations discussed above in the context of the annual cycle also occur on much shorter time scales. In fact, most of the variance in the wind field occurs on time scales of from several days to one month (Furey, 1996). At these time scales the wind field over the northern Bering shelf and Chukchi Sea are coherent (Furey, 1996; Weingartner et al., 1998) as are the currents (Weingartner et al., 1998). With this in mind, we comment on two potentially interesting consequence of these shorter period variations. We illustrate these with the preceding figures insofar as they mimic "snapshots" of the shorter period circulation fields. The features discussed herein are also most easily seen in the video supplied with this report.

The first point to note is the role of the wind-forced variations on the Siberian Coastal Current. As mentioned in section 3.1, this current is forced by cross-shore pressure gradients associated with horizontal density gradients (baroclinic pressure gradients) As it flows southeastward along the Siberian coast it will encounter an increasingly adverse (secular) pressure gradient as it nears Bering Strait. At the point where the baroclinic pressure gradient is equal and opposite to the secular pressure gradient the net pressure gradient vanishes. Geostrophy breaks down approaching this point and the nonlinear terms becoming increasing important in the momentum balance. We expect that the current should breakup and turn away from the Siberian coast (retroflect) into the central Chukchi Sea. Under steady-state conditions the retroflection point could be determined. However, stochastic wind-forcing will change this location, because the winds will effect a sea level setup and/or setdown whose effects add to the baroclinic and secular pressure gradients. Thus the net pressure gradient across the Siberian Coastal Current is a function of the secular pressure gradient, the wind-induced sea level gradient, and the baroclinic pressure gradient established by the river runoff.

Northwesterly winds establish a sea level setup that augments the baroclinic pressure gradient so the current should penetrate further to the southeast before retroflecting. Under sufficiently strong winds, the current can flow through Bering Strait (Weingartner et al., in prep. b). Southeasterly winds result in a sea level setdown along the Siberian coast that augments the secular pressure gradient so that the current could be blocked from penetrating southeastward along this coast. In the extreme, this current can be prevented from entering the Chukchi Sea (Weingartner et al., in prep. b; Münchow et al., submitted). Thus, the retroflection point for southeasterly winds will generally occur further to the west than the retroflection under northwesterly winds.

The winds along the Siberian coast vary primarily in the alongshore direction (Weingartner et al., in prep. b) so that we expect the retroflection point to vary on synoptic time scales. Both the winds and runoff vary tremendously throughout the year, thus we expect comparable variations in the structure of the Siberian Coastal Current. Changes in the retroflection point are readily seen in the video, although in this case only the wind-forcing, secular pressure gradient and a sea level slope associated with runoff from the Kolyma River are involved. (The latter is small and

limited to the vicinity of the Kolyma River delta). This variability needs to be appreciated when designing field programs intended to define the extent and transport of the Siberian Coastal Current. Retroflection implies that Siberian Coastal Current waters are mixed with the inflow through Bering Strait, primarily in Hope Valley. As described previously some of the water in Hope Valley is transported eastward over the north central Chukchi shelf. Thus retroflection has implications for contaminants carried into the Chukchi Sea by this current for it represents an efficient means by which these materials can be dispersed over the shelf.

A second, and more speculative point, is that fluctuations in transport through Bering Strait might be reflected as transport fluctuations in the boundary current along the Beaufort Sea shelfbreak. (The video gives this impression.) Although our model is not appropriate for studying this possibility, there is both theoretical (Huthnance, 1986) and observational (Aagaard, 1984) evidence to suggest that this might in fact occur.

3.4 Storm Surge

Figures 31 - 35 show the frequency of occurrence of positive and negative storm surge events for Pt. Barrow, Pt. Lay, Pt. Hope, Kivalina, Shishmaref, and Wales based upon the 15 year model time series. (The locations of these communities are shown in Figure 2). The most destructive surges are positive storm surges which could cause flooding and enhance coastal erosion. Negative surges while less destructive could hinder vessel traffic and the loading and unloading of barges. (C. George, of the North Slope Borough believes that both types of storm surges might represent a human safety issue by predisposing the shorefast ice to cracking. This issue is of particular concern to subsistence hunters especially during spring when the shorefast ice serves as a platform for hunting whales.) Positive storm surges greater than 1 meter occur about 1% of the time and mainly between September and December (but in some cases in January also). The relative paucity of positive storm surges in other months is mainly due to the inhibiting effects of the ice cover (in winter) and the more moderate winds in summer. Negative storm surges of 1 m or more occur more frequently than positive storm surges because the prevailing northeasterly winds favor a sea level setdown.

4.0 Conclusions

We have used a vertically-averaged two-dimensional, non-linear, coupled ice-ocean barotropic model to examine the circulation of the Chukchi Sea. The model was forced with winds derived from the FNMOC surface atmospheric pressure fields for 15 years. The model was run on 21 km and 7 km grids. The principal conclusions of this study are:

The model predicted currents account for as much variance in the observed currents as does the wind itself. This result is encouraging insofar as it suggests that the model has (limited) applicability as a predictive tool. However, the model predicts prolonged (several months) flow reversals in winter whereas the observations suggest that these are much briefer (1 - 2 months). We believe that this discrepancy arises because the wind field used to drive the model

overestimates the true winds. This overestimate could be especially severe in winter when winds speeds are large. Consequently, the model-predicted mean annual current speeds underestimate the observed current speeds.

At this level of development, the model does a better job of predicting current variability in the eastern Chukchi Sea than in the western Chukchi Sea. Indeed there are some locations where the observed and modeled currents are virtually uncorrelated. We believe that baroclinic processes in the western Chukchi Sea are most likely responsible for this failure. These processes are associated with energetic eddies shed by instability of the buoyancy forced Siberian Coastal Current and perhaps also by the production of dense water in winter in the polynyas surrounding Wrangel Island.

The model proved valuable in diagnosing the basin wide dynamics associated with flow reversals on the northeast Chukchi Sea shelf. It has been useful in developing heuristic arguments as to why the Siberian Coastal Current generally turns offshore (away from the Siberian coast) on the Chukchi shelf and mixes with the Bering inflow in Hope Valley. This mixture is eventually transported through Herald Valley. From here it is carried northward into the Arctic Ocean or eastward across the north central shelf and into the coastal zone adjacent to Alaska. The Siberian Coastal Current transports water from as far west as the Laptev Sea. Thus, the model suggests that contaminants from these regions could be advected in to Alaskan waters by the transport pathways outlined here.

The model corroborates observational evidence that suggests a relatively stagnant circulation over Hanna and Herald shoals and a weak clockwise circulation around Wrangel Island. These regions would tend to retain pollutants released or advected into the area. Although Wrangel Island lies within Russian waters, it supports large numbers of walrus that migrate between the Bering and Chukchi seas. These animals are an important subsistence food source for native Alaskans. Similarly the ice edge of the northern Chukchi Sea is crucial habitat to large numbers of marine mammals. The model and observations imply that pollutants discharged into the western and southern Chukchi Sea would likely be distributed over a broad area of the northern shelf.

5.0 Recommendations

The scope of this project did not allow comparison between the proxy wind fields used to force the model and the real winds. We recommend that some effort be expended on just such a comparison so that a better formulation of the surface wind field can be obtained. This vertically-averaged model is likely to perform reasonably well on portions of the Chukchi shelf. A slightly more sophisticated model that solves for the velocity at different water depths could be implemented with little additional cost. Presumably, the main advantage of such a model is that it would allow better tracking of surface trapped (or bottom trapped contaminants) than the vertically averaged model.

6.0 References

Aagaard, K. 1984: The Beaufort undercurrent. p. 47-71 *In* P. Barnes and E. Reimnitz (eds.), The Alaskan Beaufort Sea: Ecosystems and Environment. Academic Press.

Aagaard, K. 1988: Current, CTD, and pressure measurements in possible dispersal regions of the Chukchi Sea. OCSEAP Final Rept. Princ. Investigators 57: 255-333. DOI/MMS Anchorage, Alaska.

Aagaard, K. 1989. A synthesis of the Arctic Ocean circulation. Rapp. P.-v. Reun. Cons. int. Explor. Mer. 188: 11-22.

Aagaard, K. and A. T. Roach. 1990. Arctic Ocean-shelf exchange: measurements in Barrow Canyon. J. Geophys. Res. 95: 18163-18175.

Aagaard, K., L. K. Coachman and E. C. Carmack. 1981. On the halocline of the Arctic Ocean. Deep-Sea Res. 28: 529-545.

Aagaard, K, C. H. Pease, A. T. Roach and S. A. Salo. 1990. Beaufort Sea mesoscale circulation study. Final Report. NOAA Tech. Memo ERL-PMEL-90. 114 pp. Pac. Mar. Environ. Lab, Seattle, Wash.

Brower, W. A., Jr., R. G. Baldwin, C. N. Williams, Jr., J. L .Wise, and L.D. Leslie. 1988. Climate atlas of the outer continental shelf waters and coastal regions of Alaska, volume III, Chukchi-Beaufort Sea. National Climatic Data Center, Asheville, NC, 28801. 497 pp.

Carmack, E. C. 1986. Circulation and mixing in ice-covered waters. pp.641-712 *In* N. Untersteiner, (ed.), The Geophysics of Sea Ice. Plenum, New York.

Cavalieri, D. J. and S. Martin. 1994. The contribution of Alaskan, Siberian, and Canadian coastal polynyas to the cold halocline layer of the Arctic Ocean. J. Geophys. Res. 99: 18343-18362.

Coachman, L. K. 1993. On the flow field in the Chirikov Basin. Cont. Shelf Res. 13: 481-508.

Coachman, L.K., and K. Aagaard. 1988. Transports through Bering Strait: annual and interannual variability. J. Geophys. Res. 93: 15535-15539.

Coachman, L.K., K. Aagaard, and R. B. Tripp. 1975: Bering Strait: The Regional Physical Oceanography. University of Washington Press, Seattle, Washington. 172 pp.

Coachman, L. K. and V.V. Shigaev. 1992. Northern Bering-Chukchi sea ecosystem: the physical basis. pp. 17-27 *In* P.A. Nagel (ed) Results of the third joint U.S.-U.S.S.R. Bering and Chukchi seas expedition (BERPAC). U. S. Fish and Wildlife Service, Washington, DC.

Codispoti, L. and F. A. Richards. 1968. Micronutrient distributions in the East Siberian and Laptev seas during summer 1963. Arctic 21:67-83.

Furey, P. 1996. The large-scale surface wind field over the western Arctic Ocean, 1981-1993. Unpubl. M. Sc. thesis. University of Alaska, Fairbanks, AK. 121 pp.

Gawarkiewicz, G. and D. C. Chapman. 1995. A numerical study of dense water formation and transport on a shallow, sloping continental shelf. J. Geophys. Res. 100: 4489-4508.

Gawarkiewicz, G., J. C. Haney, and M. J. Caruso. 1994. Summertime synoptic variability of frontal systems in the northern Bering Sea. J. Geophys. Res. 99: 7617-7626.

Gudkovich, Z.M. 1961. On the nature of Pacific currents in the Bering Strait and the causes of seasonal variations in their intensity. Okeanologiya 1: 608-612. (in Russian).

Grebmeier, J. 1993. Studies on pelagic-benthic coupling extended onto the Russian continental shelf in the Bering and Chukchi Seas. Cont. Shelf Res. 13: 653-668.

Grebmeier, J. M., and C. P. McRoy. 1989. Pelagic-benthic coupling on the shelf of the northern Bering and Chukchi Seas. III. Benthic food supply and carbon cycling. Mar. Ecol. Prog. Ser. 53: 79-91.

Grebmeier, J. M., C. P. McRoy, and H. M. Feder. 1988. Pelagic-benthic coupling on the shelf of the northern Bering and Chukchi Seas. I. Food supply source and benthic biomass. Mar. Ecol. Prog. Ser. 48: 57-67.

Grebmeier, J. M., H. M. Feder, and C. P. McRoy. 1989. Pelagic-benthic coupling on the shelf of the northern Bering and Chukchi Seas. II. Benthic community structure. Mar. Ecol. Prog. Ser. 51: 253-268.

Hakkinen, S. 1986. Coupled ice-ocean dynamics in the marginal ice zones: up/downwelling and eddy generation. J. Geophys. Res. 87: 5853-5859.

Hansell, D., T. E. Whitledge, and J. J. Goering. 1993. Patterns of nitrate utilization and new production over the Bering-Chukchi shelf. Cont. Shelf Res. 13: 601-627.

Huthnance, J. M. 1986. The subtidal behavior of the Celtic Sea - III. A model of shelf waves and surges on a wide shelf. Cont. Shelf Res. 5:347-377.

Johnson, W. R. 1989: Current response to wind in the Chukchi Sea: a regional coastal upwelling event. J. Geophys. Res. 94: 2057-2064.

Kowalik, Z. 1981. A study of the M_2 tide in the ice-covered Arctic Ocean. Modeling, Identification and Control. 2: 210-223.

Kowalik, Z. and A. Y. Proshutinsky. 1993. Diurnal tides in the Arctic Ocean, J. Geophys. Res., 98: 16449-16468.

Martin, S, and R. Drucker. 1997. The effect of possible Taylor columns on the summer ice retreat in the Chukchi Sea. J. Geophys. Res. 102:10473-10482.

McPhee, M. 1980. Analysis and prediction of short term ice-drift. Proc. Inst., Offshore Mech., Arctic Eng. Symp. 5:385-393.

Melling, H. 1993. The formation of a haline shelf front in wintertime in an ice-covered arctic sea. Cont. Shelf Res. 13: 1123-1147.

Münchow, A., T. Weingartner and L. Cooper. (submitted). On the summer subinertial surface circulation of the East Siberian Sea. (submitted to J. Phys. Oceanogr.).

Newton, J. L. and B. Sotirin. 1997. Boundary undercurrent and water mass changes in the Lincoln Sea, J. Geophys. Res. 102: 3393-3403.

Nikiforov, Y. G. and A. O. Shpaikher. 1980. Features of the formation of the hydrological regime and large scale variations in the Arctic Ocean. Gidrometeizdat, Leningrad. 269 pp. (in Russian).

Overland, J. E. and C. H. Pease. 1982. Cyclone climatology of the Bering Sea and its relation to sea ice extent. Mon. Wea. Rev. 110:5-13.

Overland, J. E. and A. T. Roach. 1987. Northward flow in the Bering and Chukchi seas. J. Geophys. Res. 92: 7097-7105.

Overland, J. E., P. Stabeno and S. A. Salo. 1996. Direct evidence for northward flow on the northwestern Bering Sea shelf. J. Geophys. Res. 101: 8971-8976.

Pavlov, V., L. A. Timokhov, G. A. Baskalov, M. Yu. Kulakov, V. K. Kurazhov, P. V. Pavlov, S. V. Pivovarov and V.V. Stanovoy. 1996. Hydrometeorological regime of the Kara, Laptev, and East-Siberian seas. Applied Physics Laboratory, U. Washington, Seattle, WA. 179 pp.

Pedlosky, J. 1987. Geophysical Fluid Dynamics. Springer-Verlag, New York. 551 pp.

Proshutinsky, A. Y. 1986. On the problem of calculating storm surge fluctuations: numerical simulation of storm surges in the shelf zone of the Arctic seas. Soviet Meteorology and Hydrology 1: 72-79. (Translated from Russian by Allerton Press., Inc.).

Proshutinsky, A. Y. 1988. Modeling seasonal fluctuations of the level of the Arctic Ocean. Soviet Meteorology and Hydrology 2: 57-65. (Translated from Russian by Allerton Press., Inc.).

Roach, A. T., K. Aagaard, C. H. Pease, S.A. Salo, T. Weingartner, V. Pavlov and M. Kulakov. 1995. Direct measurements of transport and water properties through the Bering Strait. J. Geophys. Res. 100: 18443-18457.

Romanov, I. P. 1993. Atlas of morphometric characteristics of ice and snow in the Arctic basin. St. Petersburg. 152 pp.

Rothrock, D. A. 1975. The mechanical behavior of pack ice. Annual Review of Earth and Planetary Sciences 3: 317-342.

Shtokman, V. B. 1957. Wind influence on the currents in Bering Strait and causes of its high velocities and prevailing north direction. Trudy Inst. Oceanology, Acad. Sci, USSR, 25: 171-197. (in Russian)

Spaulding, M., T. Isaji, D. Mendelsohn and A.C. Turner. 1987. Numerical simulation of wind-driven flow through Bering Strait. J. Phys. Oceanogr. 17: 1799-1816.

Stigebrandt, A. 1984. The North Pacific: a global scale estuary. J. Phys. Oceanogr. 14: 464-470.

Tiguntsev, L. 1976. Transport of Pacific water through the northern part of the Bering Sea. Trudy Arctic and Antarctic Research Institute, St. Petersburg. 316: 164-174.

Toulany, B. and C. Garrett. 1984. Geostrophic control of fluctuating barotropic flow through straits. J. Phys. Oceanogr. 14: 649-655.

Walsh, J. J., C. P. McRoy, L. K. Coachman, J. J. Goering, J. J. Nihoul, T. E. Whitledge, T. H. Blackburn, A. M. Springer, R. D. Tripp, D. A. Hansell, S. Djenidi, E. Deleersnijder, K. Henriksen, B. A. Lund, P. Andersen, F. E. Muller-Karger and K. K. Dean. 1989: Carbon and nitrogen cycling within the Bering/Chukchi Seas: source regions for organic matter effecting AOU demands of the Arctic Ocean. Progr. Oceanogr. 22: 277-359.

Weingartner, T. J., K. Aagaard, Y. Sasaki and D Cavalieri. [in prep. a] Circulation and winter baroclinic processes on the north central Chukchi Sea shelf.

Weingartner, T. J., D. J. Cavalieri, K. Aagaard and Y. Sasaki. 1998. Circulation, dense water formation, and outflow on the northeast Chukchi Sea shelf. J. Geophys. Res. 103: 7647-7661.

Weingartner, T. J., S. Danielsen, Y. Sasaki, V. Pavlov, T. Proshutinsky and M, Kulakov. [in prep. b] The Siberian Coastal Current in the Chukchi Sea: a wind and buoyancy forced arctic coastal current.

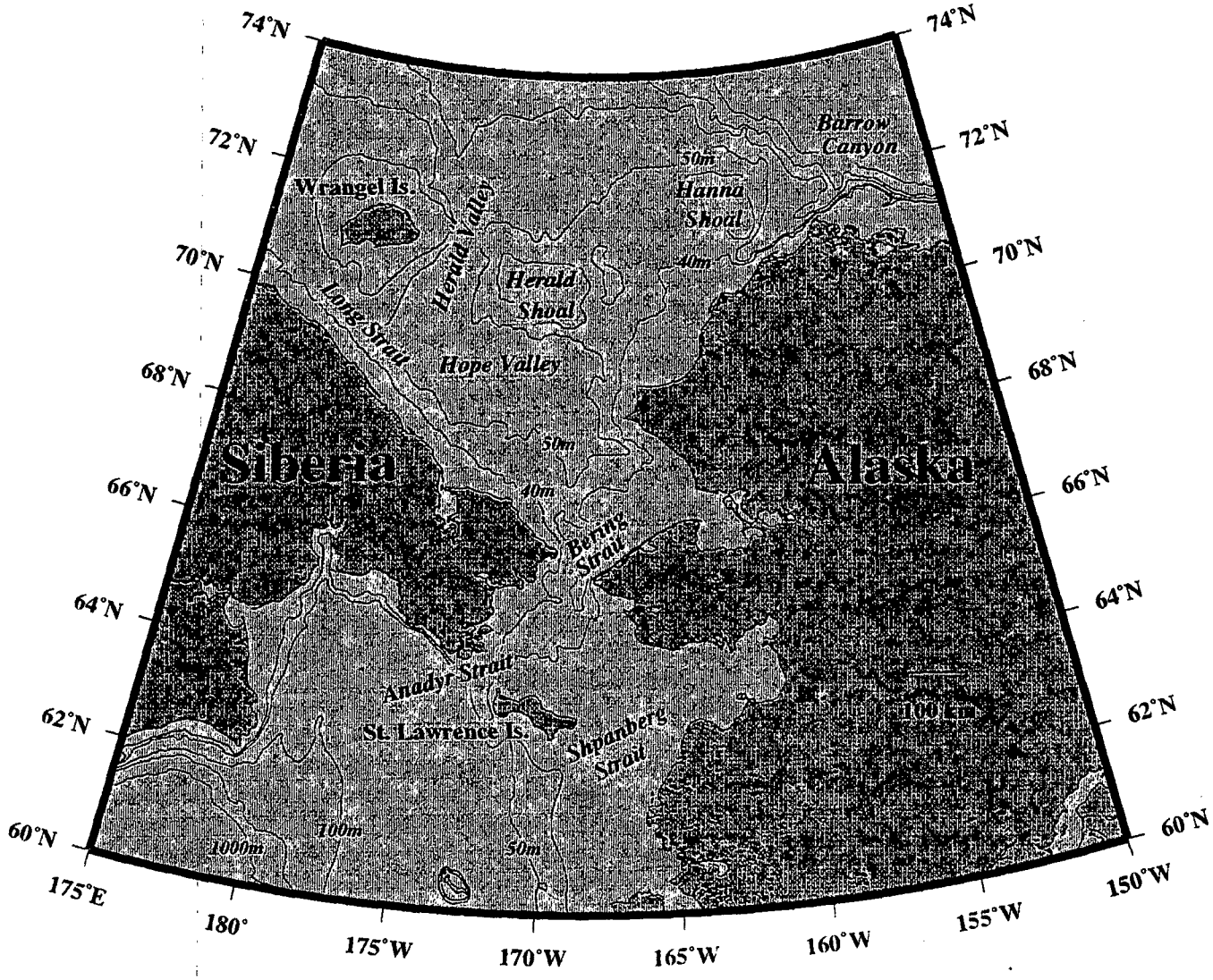

Figure 1. Bathymetric map of the Chukchi Sea.

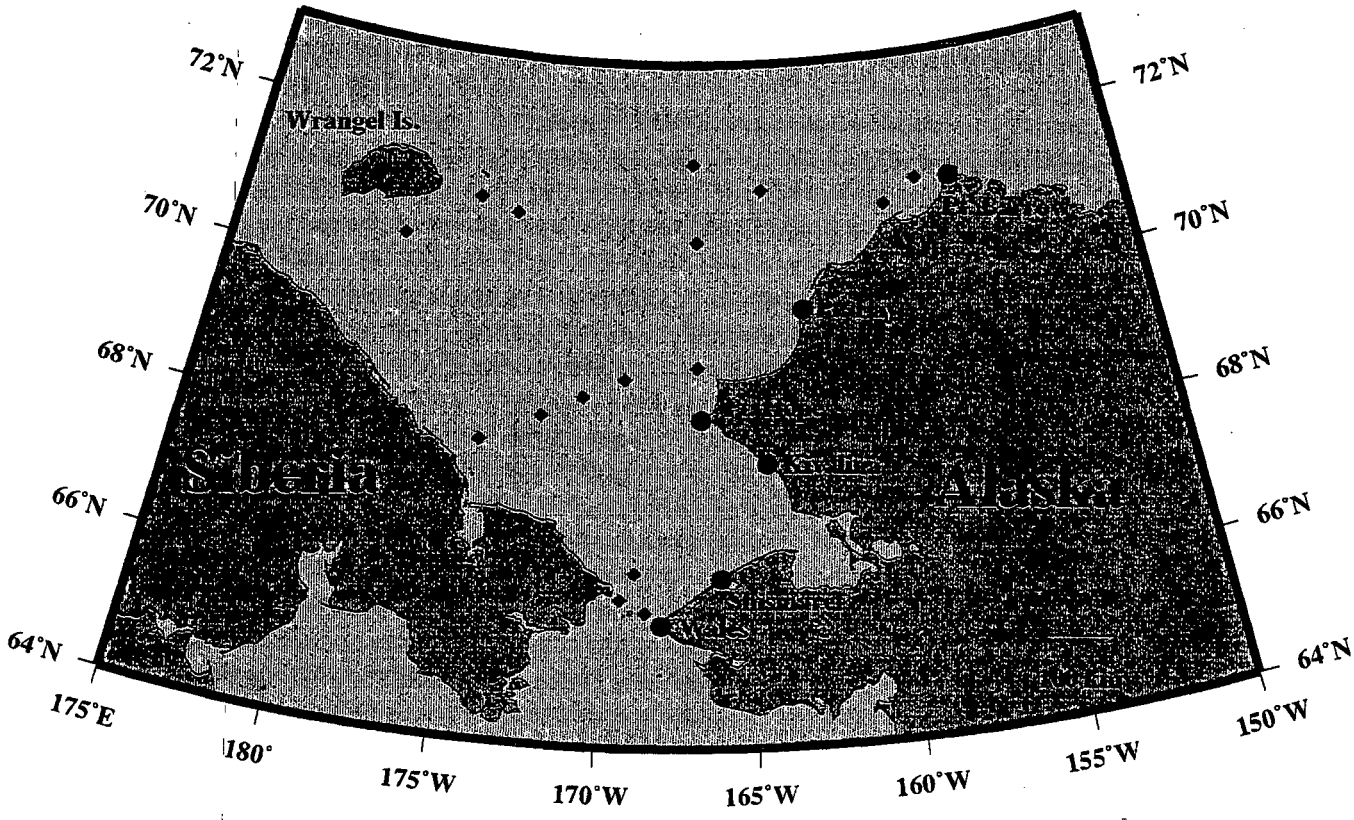

Figure 2. Location of moorings used for comparison with the model results. Locations of coastal communities for calculation of storm surge statistics.

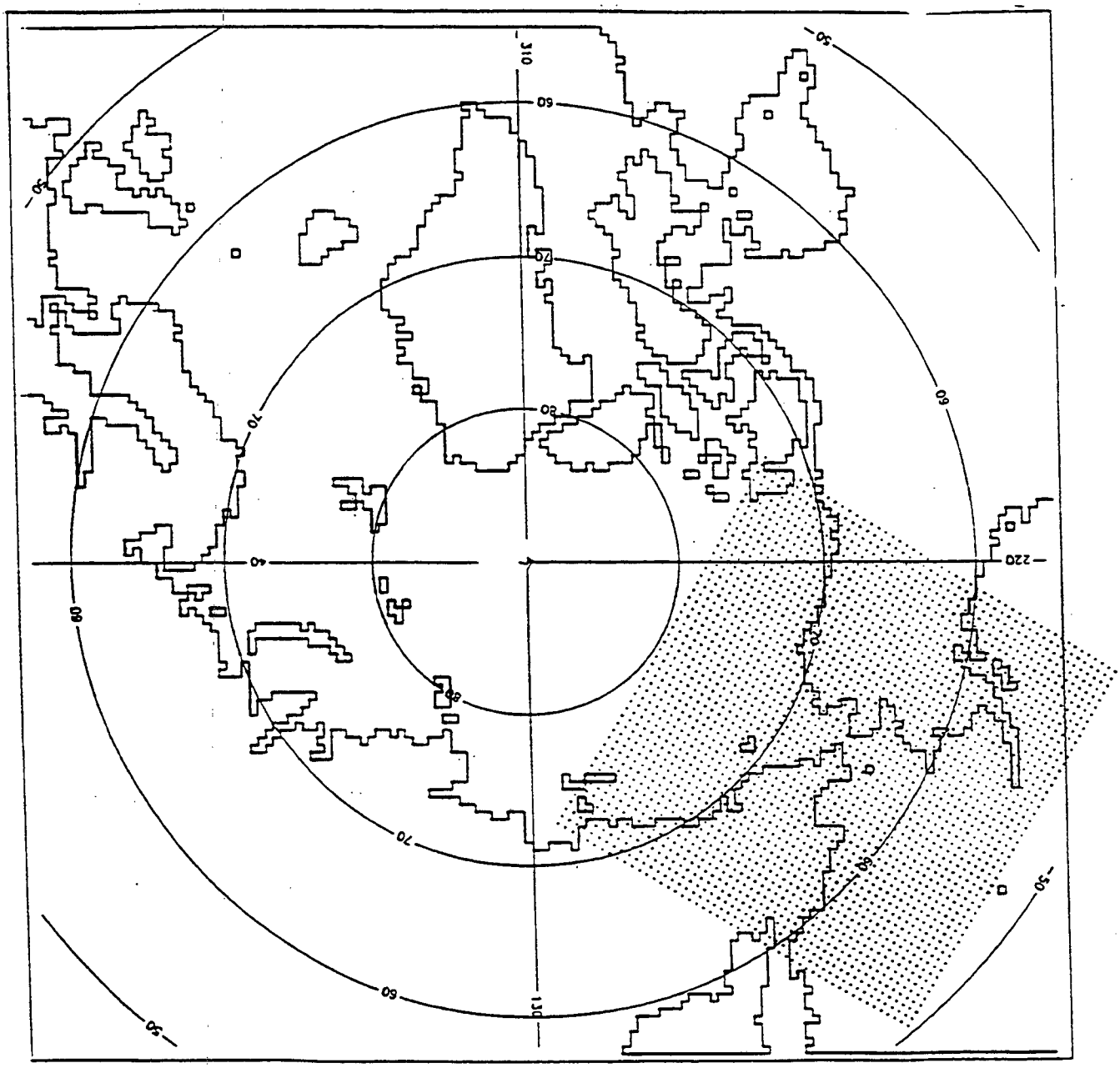

Figure 3. Computational domain (dotted area) of the numerical model.

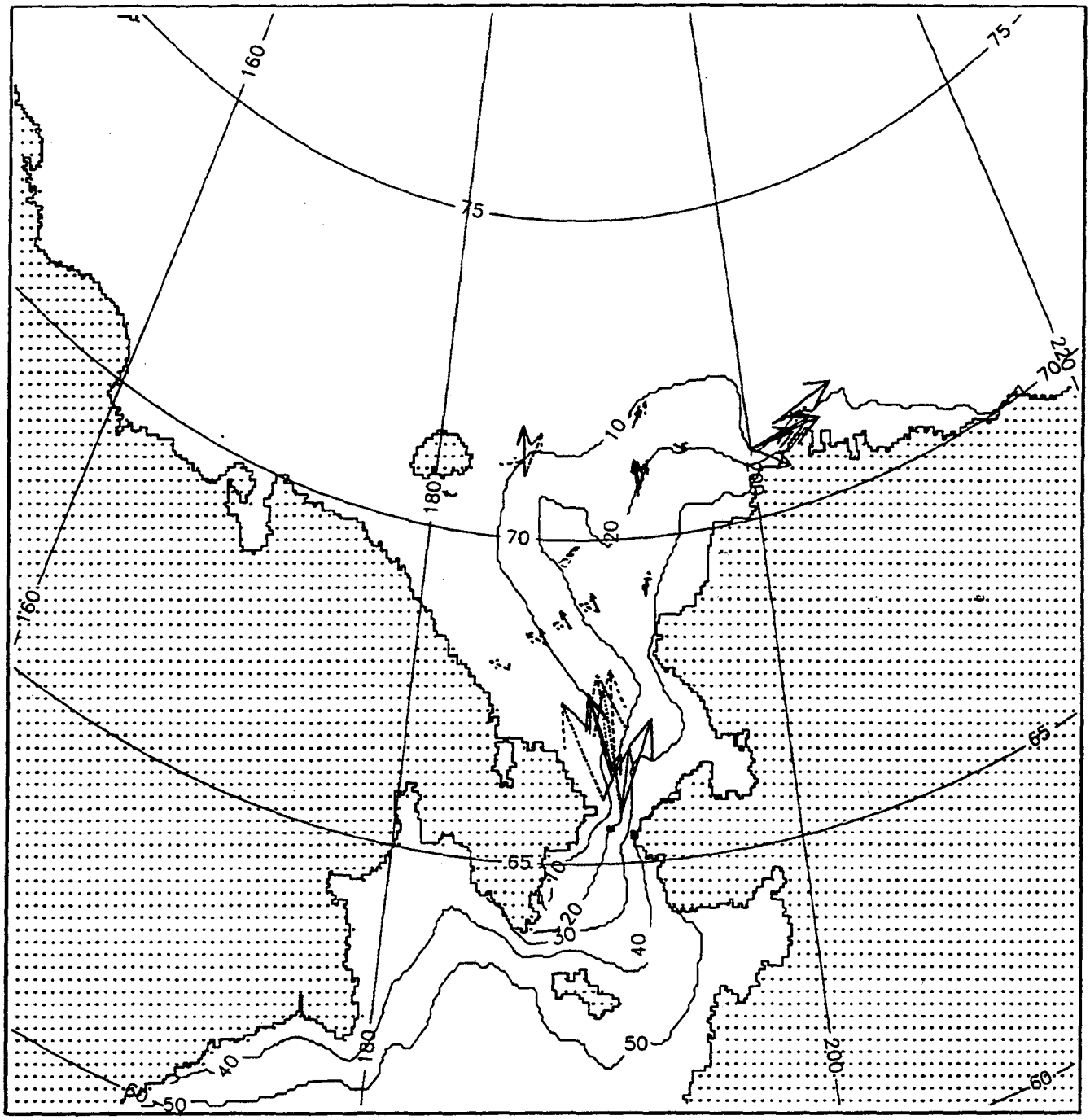

Figure 4. Sea level (cm) isopleths over the northern Bering and Chukchi Sea for the steady state condition of forcing on the 7 km grid model by the secular pressure gradient only. Observed (solid arrows) and modeled (dashed arrows) current vectors are superimposed.

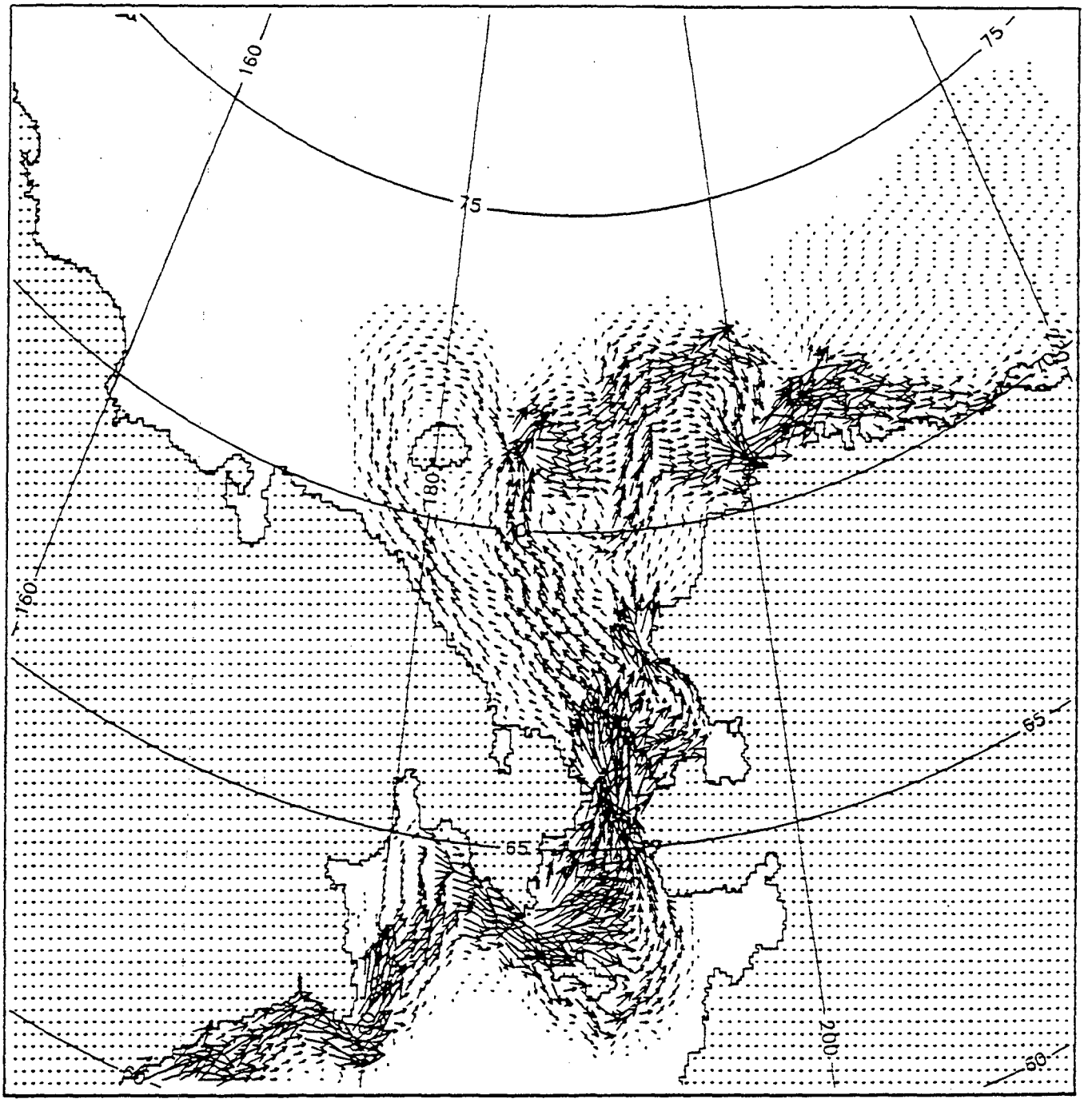

Figure 5. Steady-state velocity vectors under forcing by the secular pressure gradient only on the 7km grid. The large arrows in Bering Strait show a velocity of ~30 cm s^{-1}.

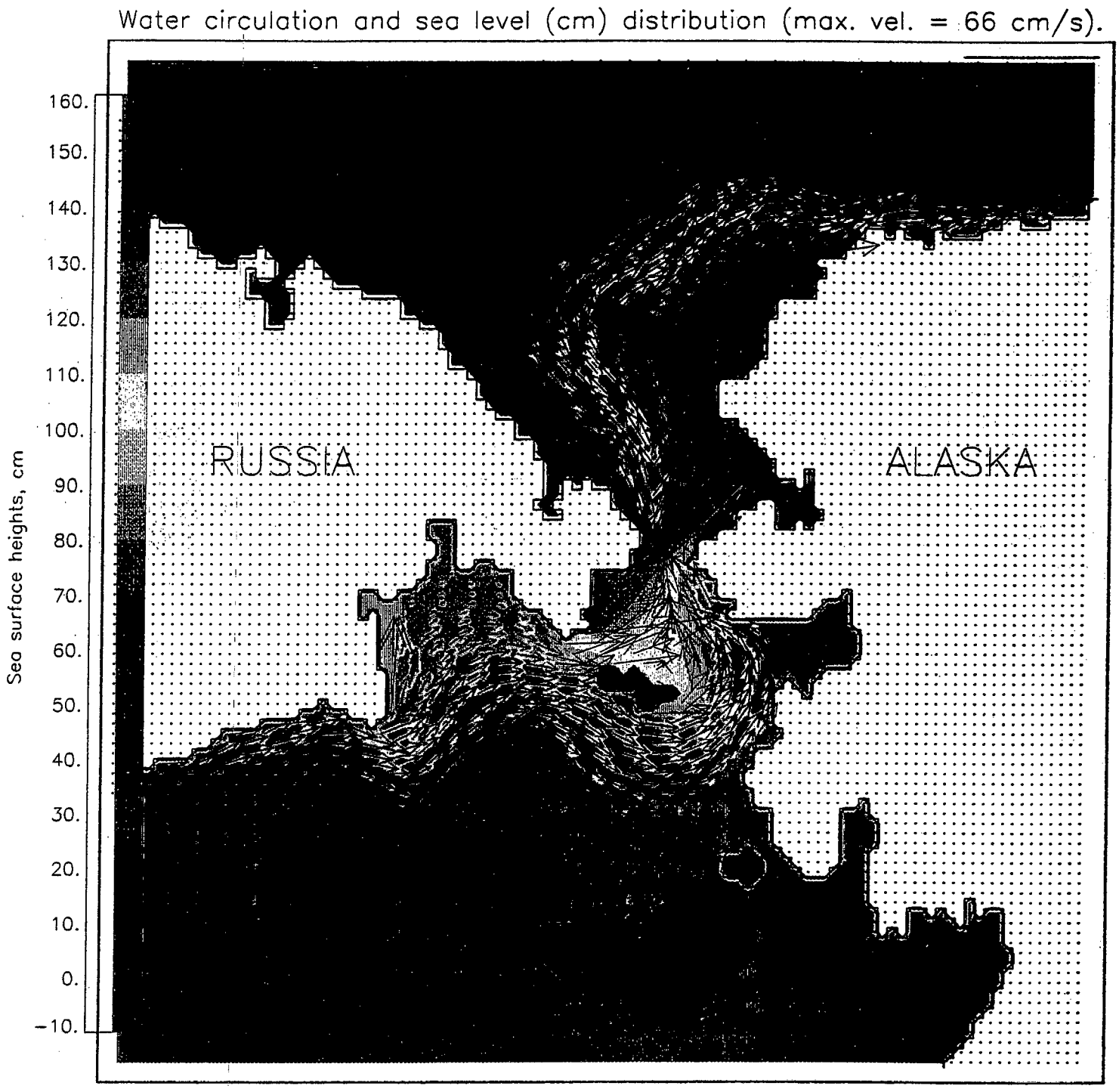

Figure 6. Steady-state velocity vectors under forcing by the secular pressure gradient only on the 21km grid. The large arrows in Bering Strait show a velocity of ~30 cm s^{-1}.

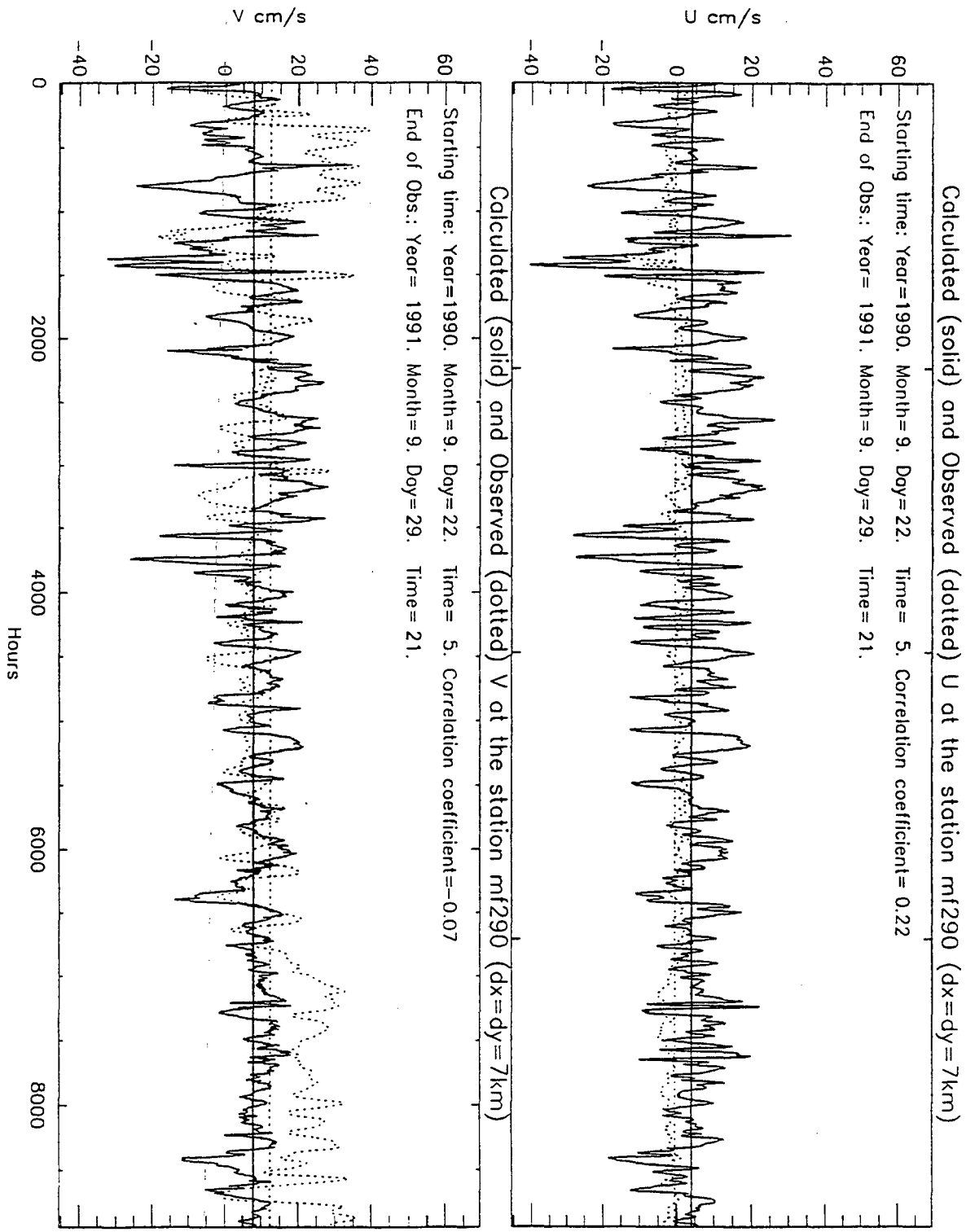

Figure 7. Comparison of the modeled (solid line) and observed (dotted line) current time series using the 21 km grid (a) and the 7 km grid (b) at mooring station BSE. The upper panel in each plot shows the east-west (u) velocity component and the lower panel shows the north-south (v) velocity component.

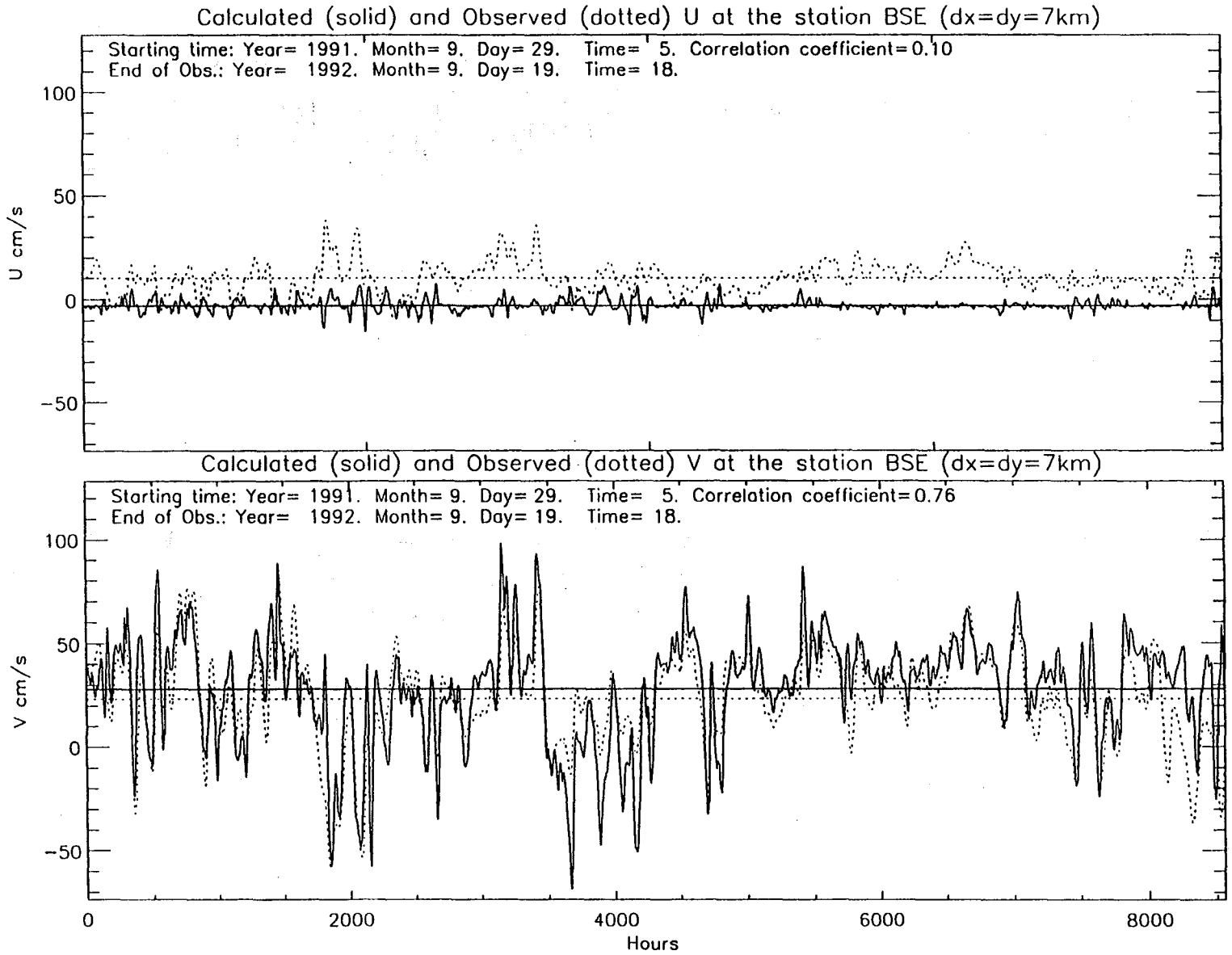

Figure 7b. Station BSE for the 7 km grid.

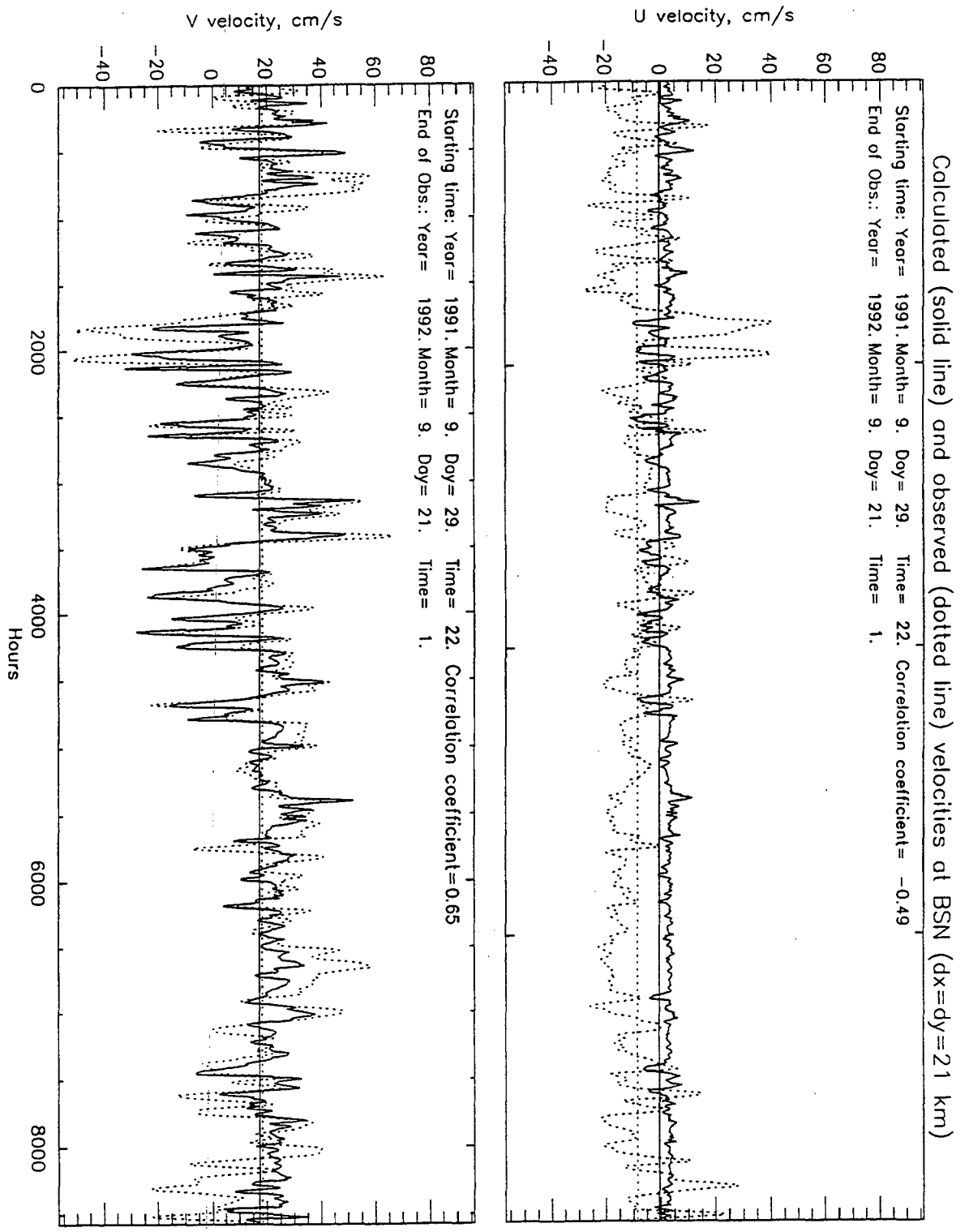

Figure 8. Comparison of the modeled (solid line) and observed (dotted line) current time series using the 21 km grid (a) and the 7 km grid (b) at mooring station BSN. The upper panel in each plot shows the east-west (u) velocity component and the lower panel shows the north-south (v) velocity component.

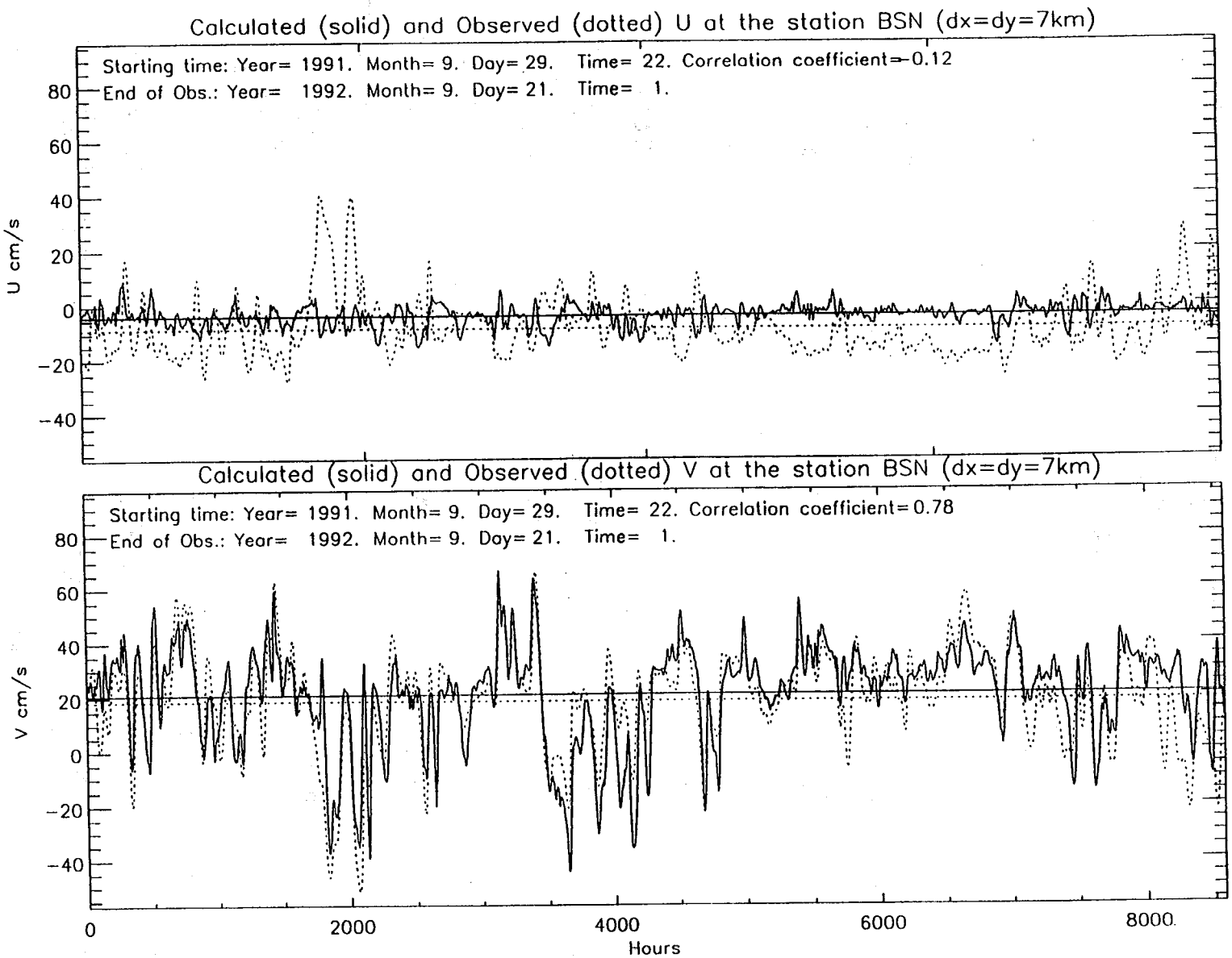

Figure 8b. Station BSN for the 7 km grid.

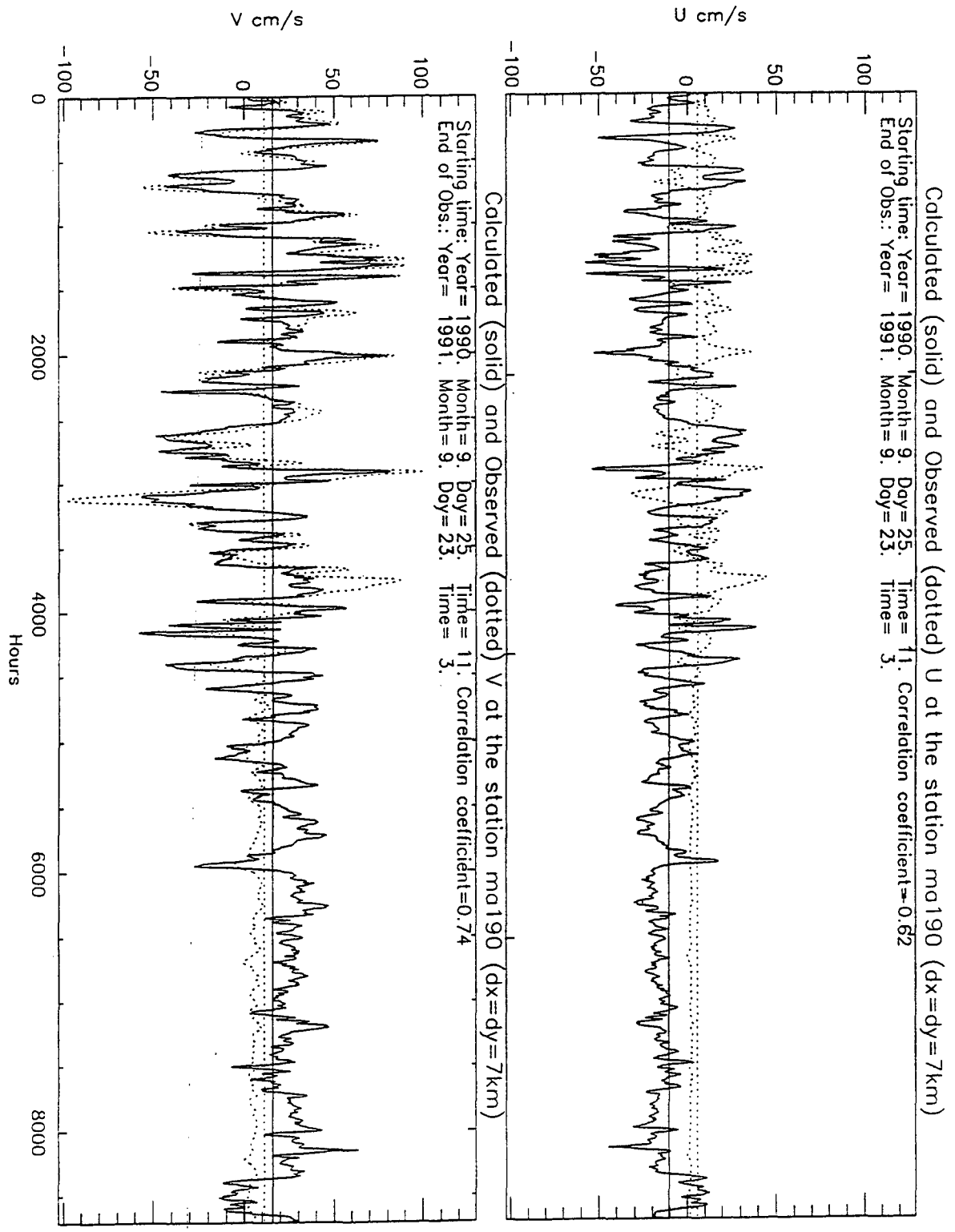

Figure 9. Comparison of the modeled (solid line) and observed (dotted line) current time series using the 21 km grid (a) and the 7 km grid (b) at mooring station MA190. The upper panel in each plot shows the east-west (u) velocity component and the lower panel shows the north-south (v) velocity component. (Current meter velocities after hour 4000 are invalid.)

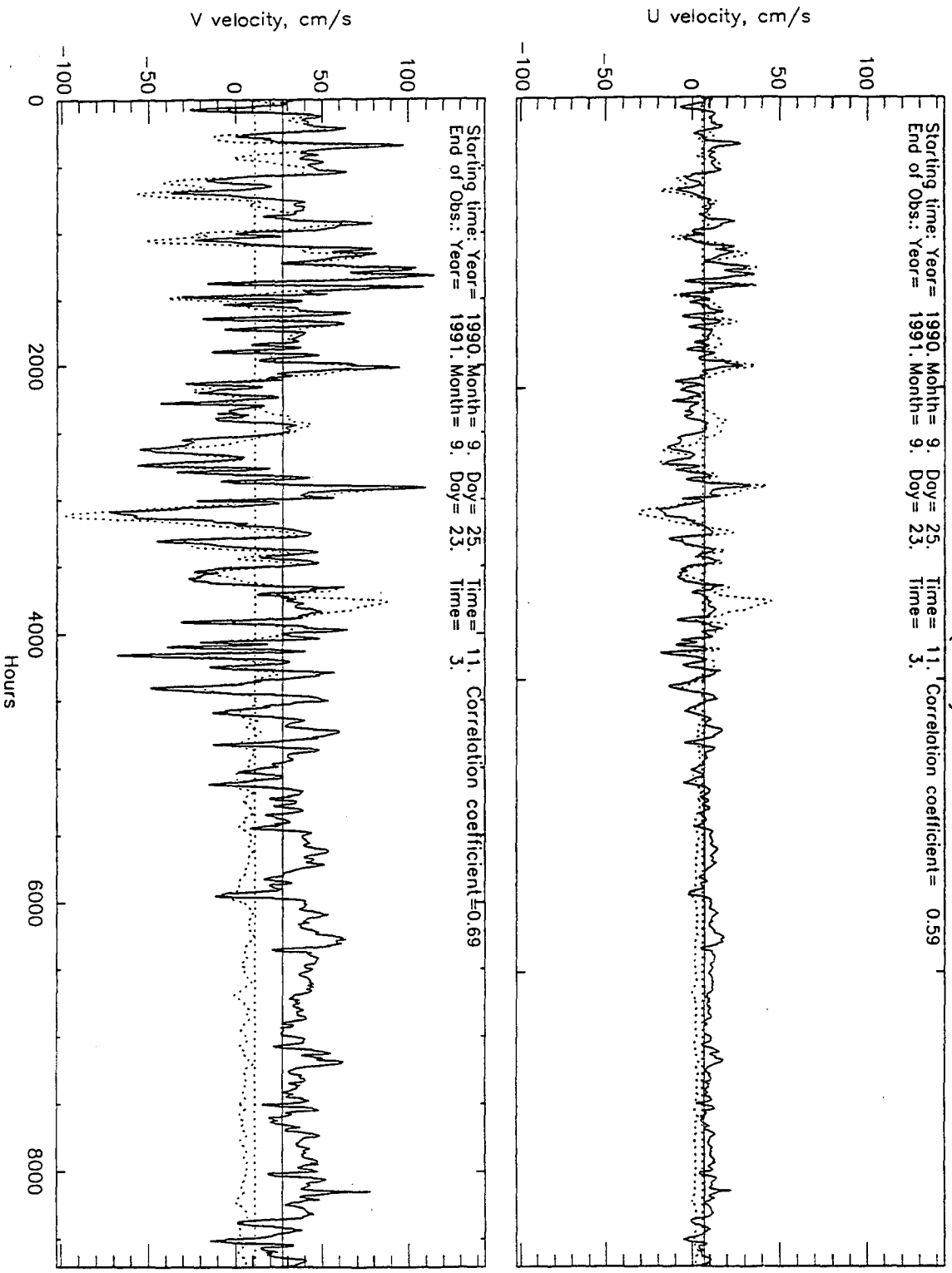

Figure 9b. Station MA190 for the 7 km grid.

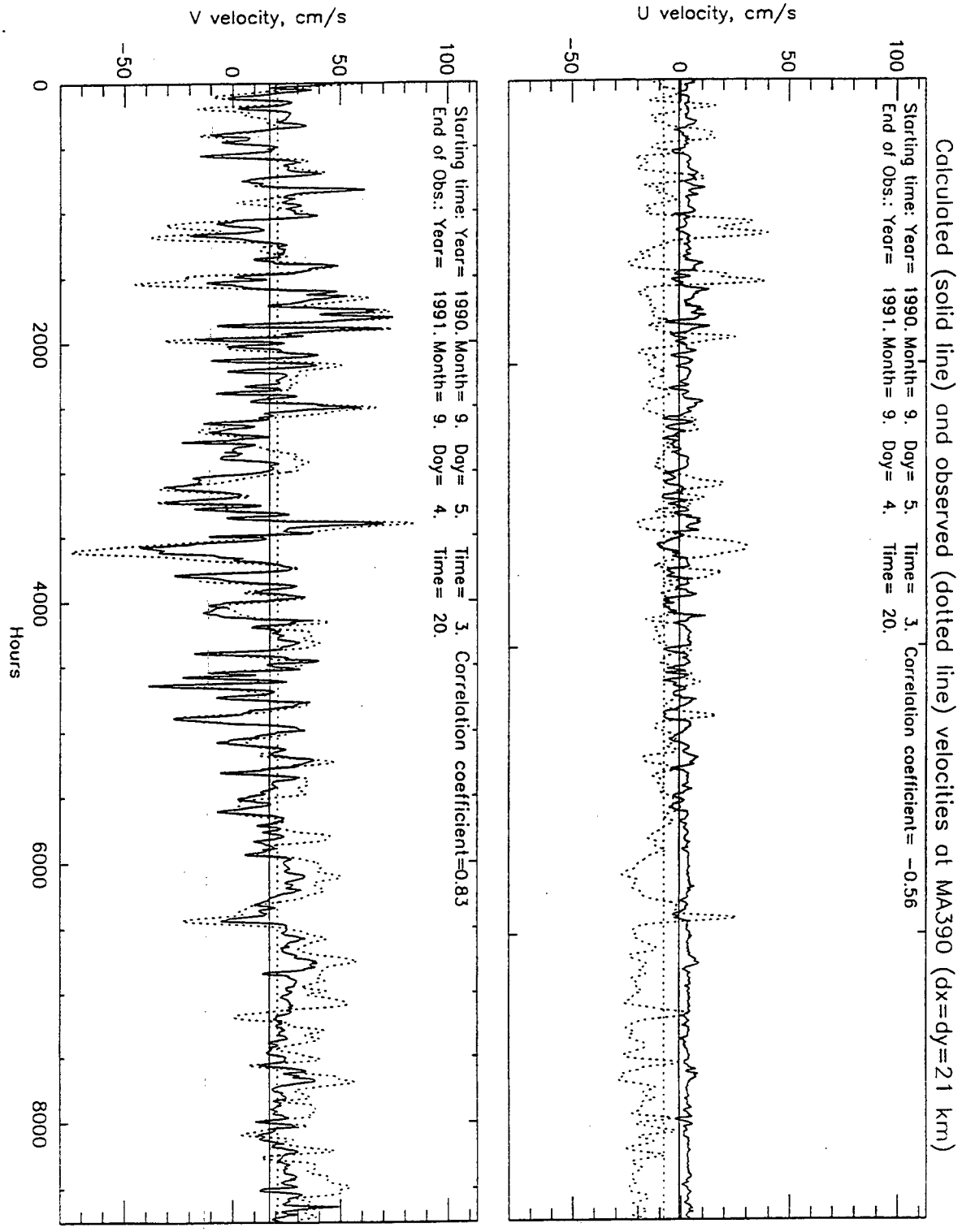

Figure 10. Comparison of the modeled (solid line) and observed (dotted line) current time series using the 21 km grid (a) and the 7 km grid (b) at mooring station MA390. The upper panel in each plot shows the east-west (u) velocity component and the lower panel shows the north-south (v) velocity component.

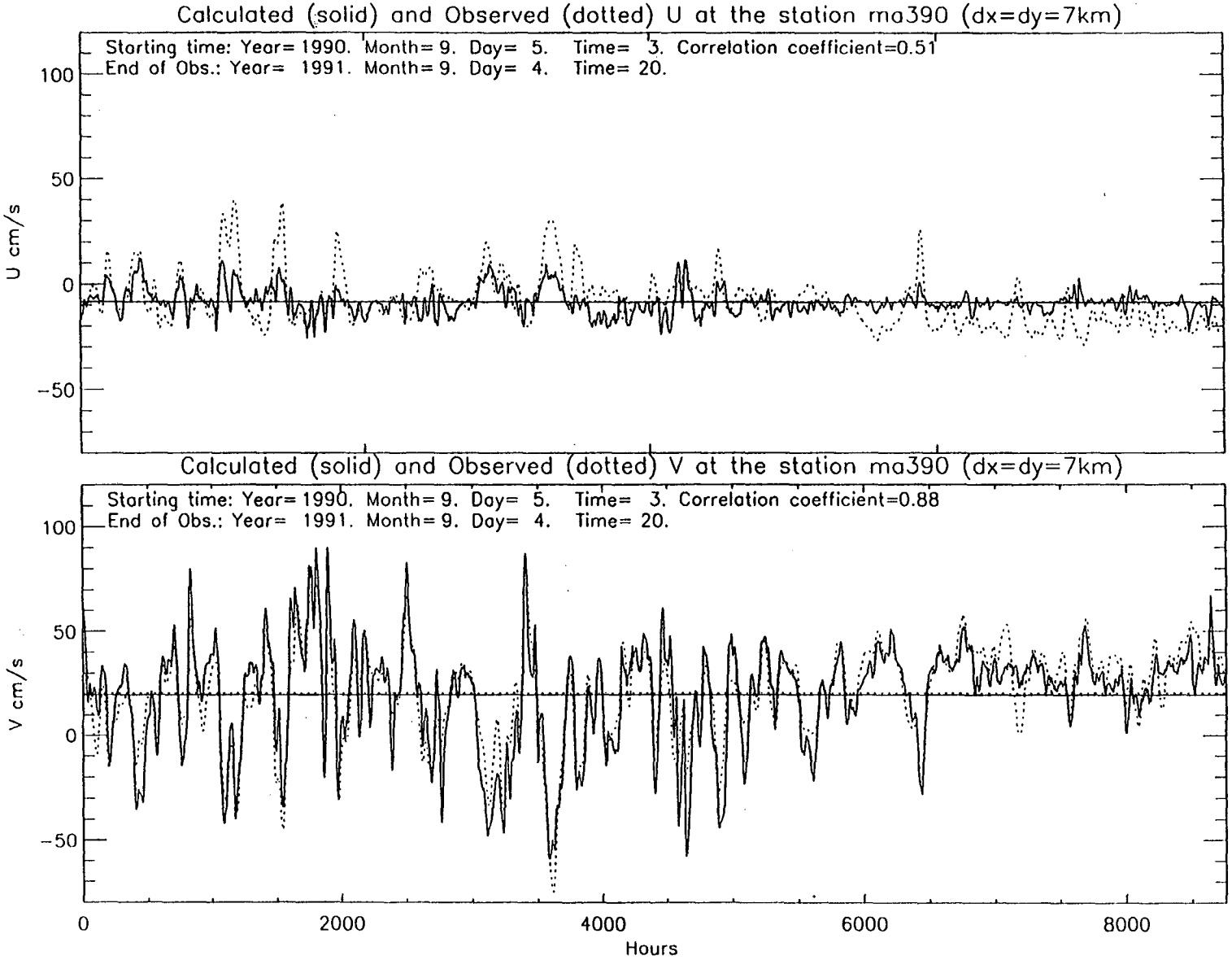

Figure 10b. Station MA390 for the 7 km grid.

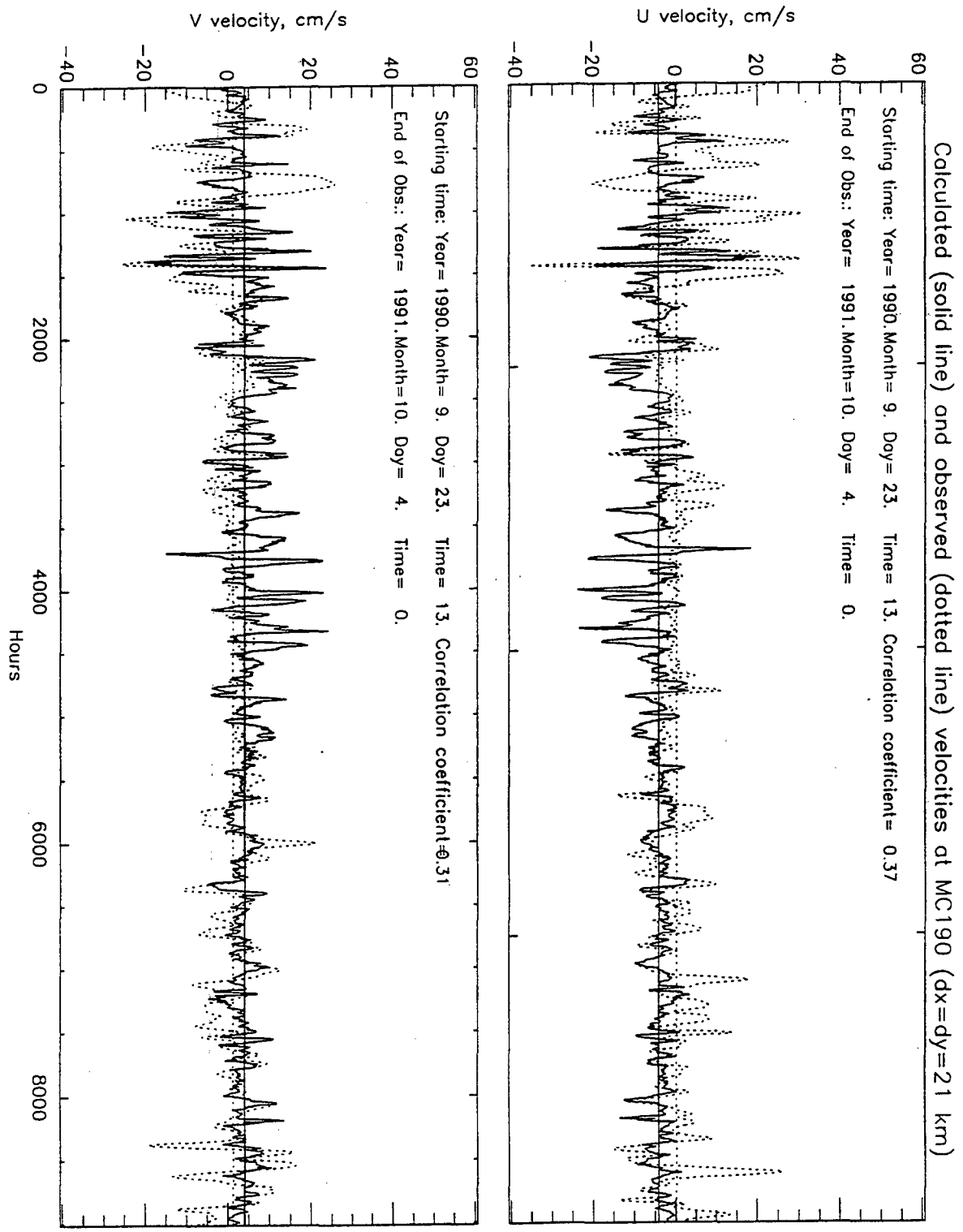

Figure 11. Comparison of the modeled (solid line) and observed (dotted line) current time series using the 21 km grid (a) and the 7 km grid (b) at mooring station MC190. The upper panel in each plot shows the east-west (u) velocity component and the lower panel shows the north-south (v) velocity component.

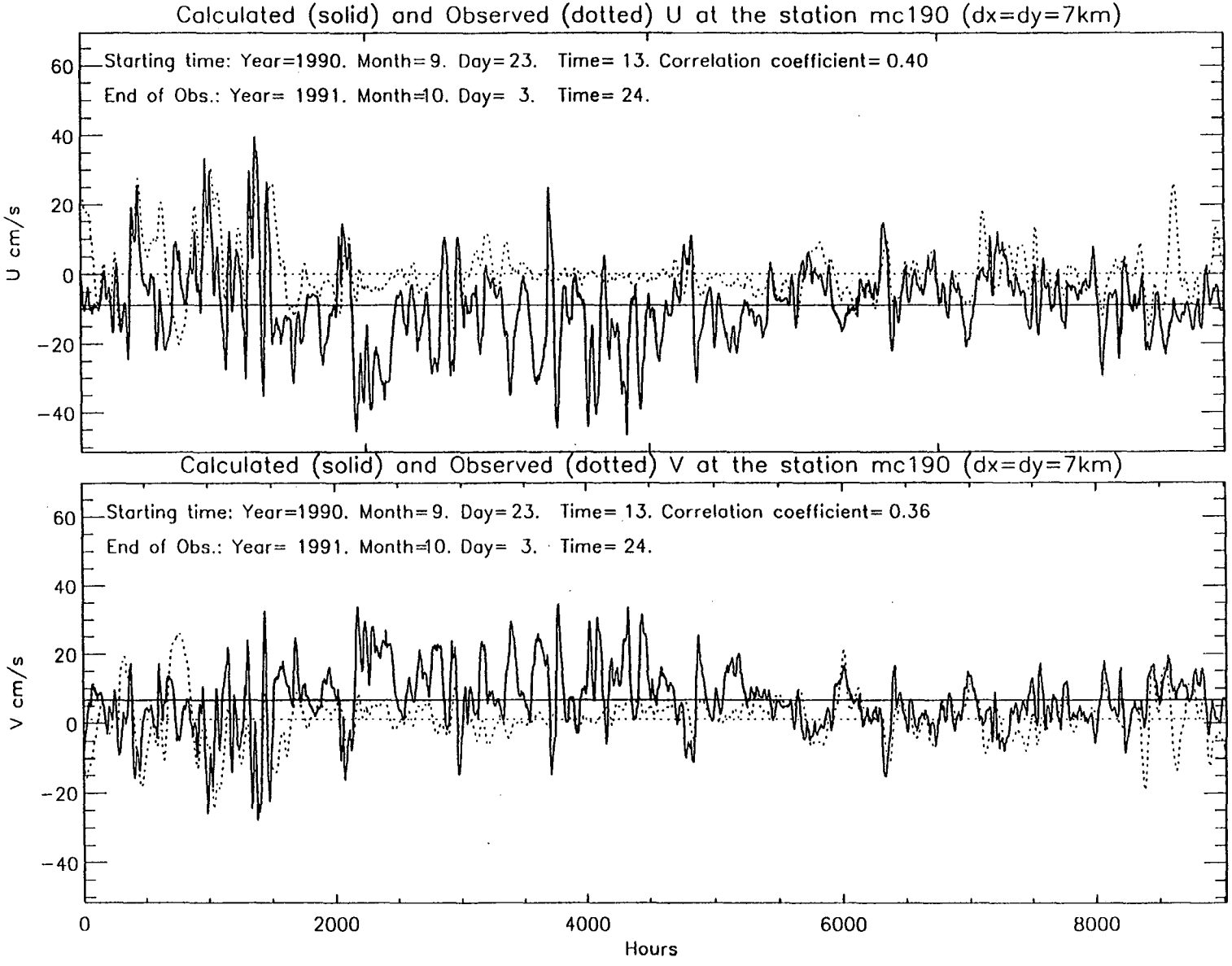

Figure 11b. Station MC190 for the 7 km grid.

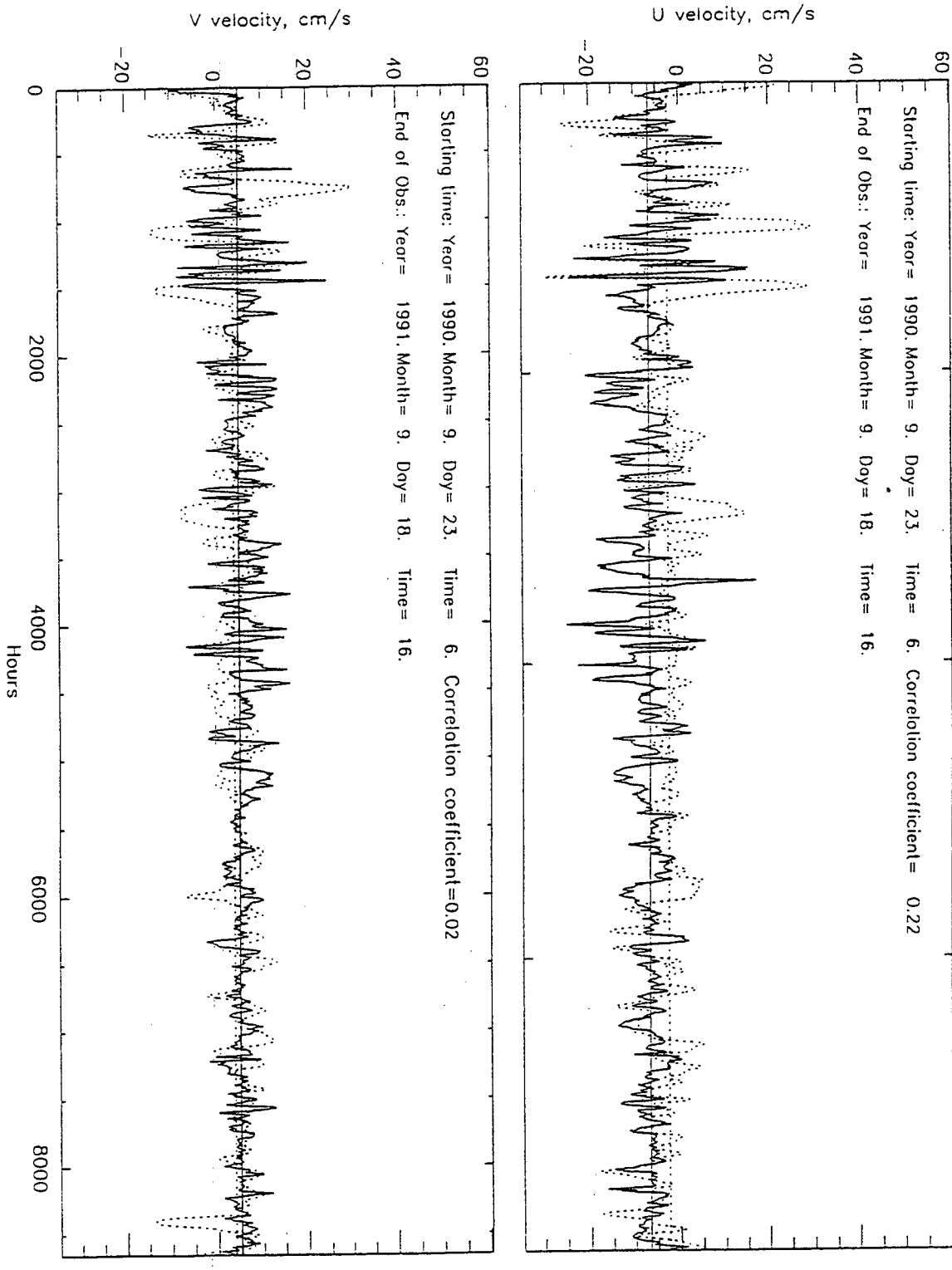

Figure 12. Comparison of the modeled (solid line) and observed (dotted line) current time series using the 21 km grid (a) and the 7 km grid (b) at mooring station MC290. The upper panel in each plot shows the east-west (u) velocity component and the lower panel shows the north-south (v) velocity component.

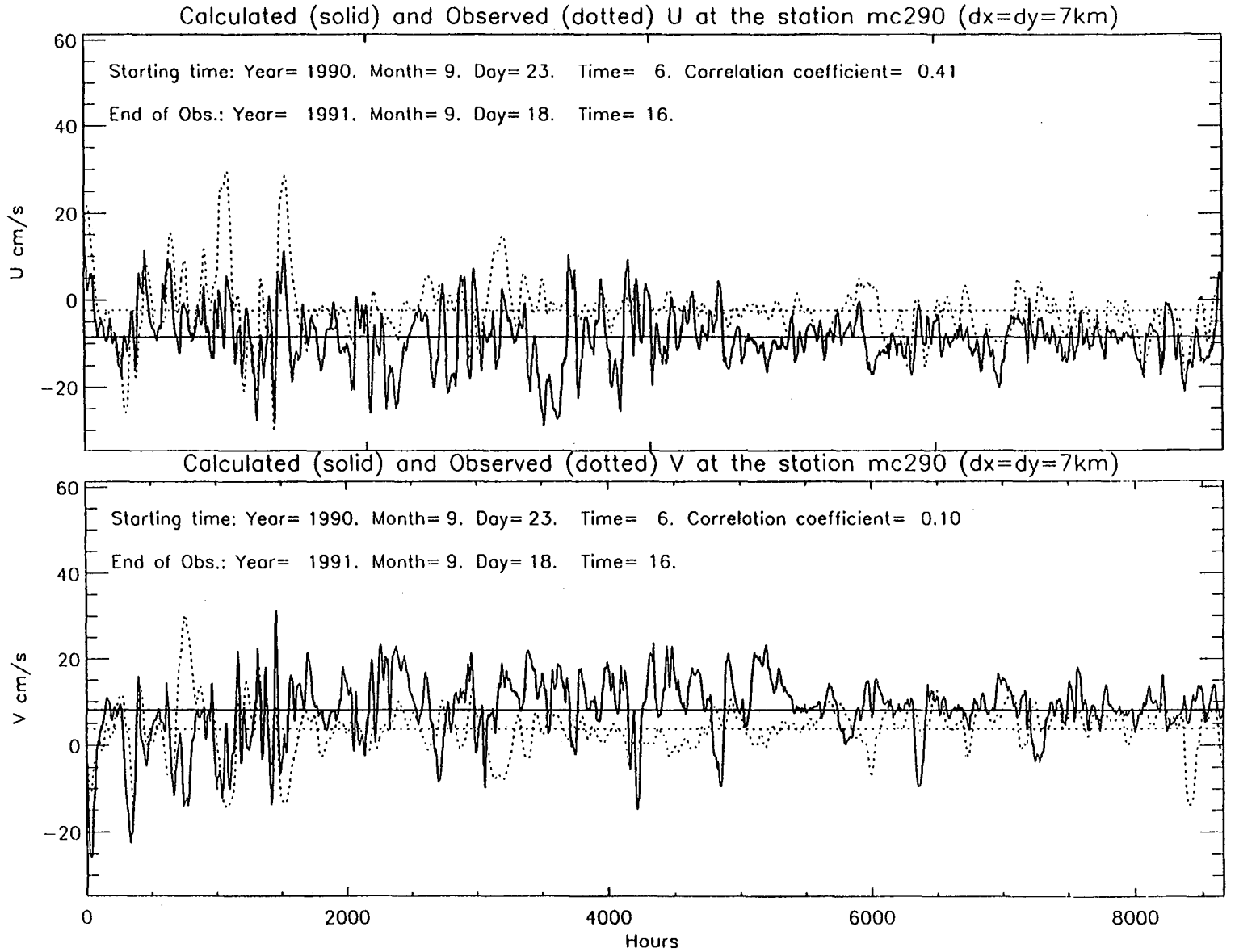

Figure 12b. Station MC290 for the 7 km grid.

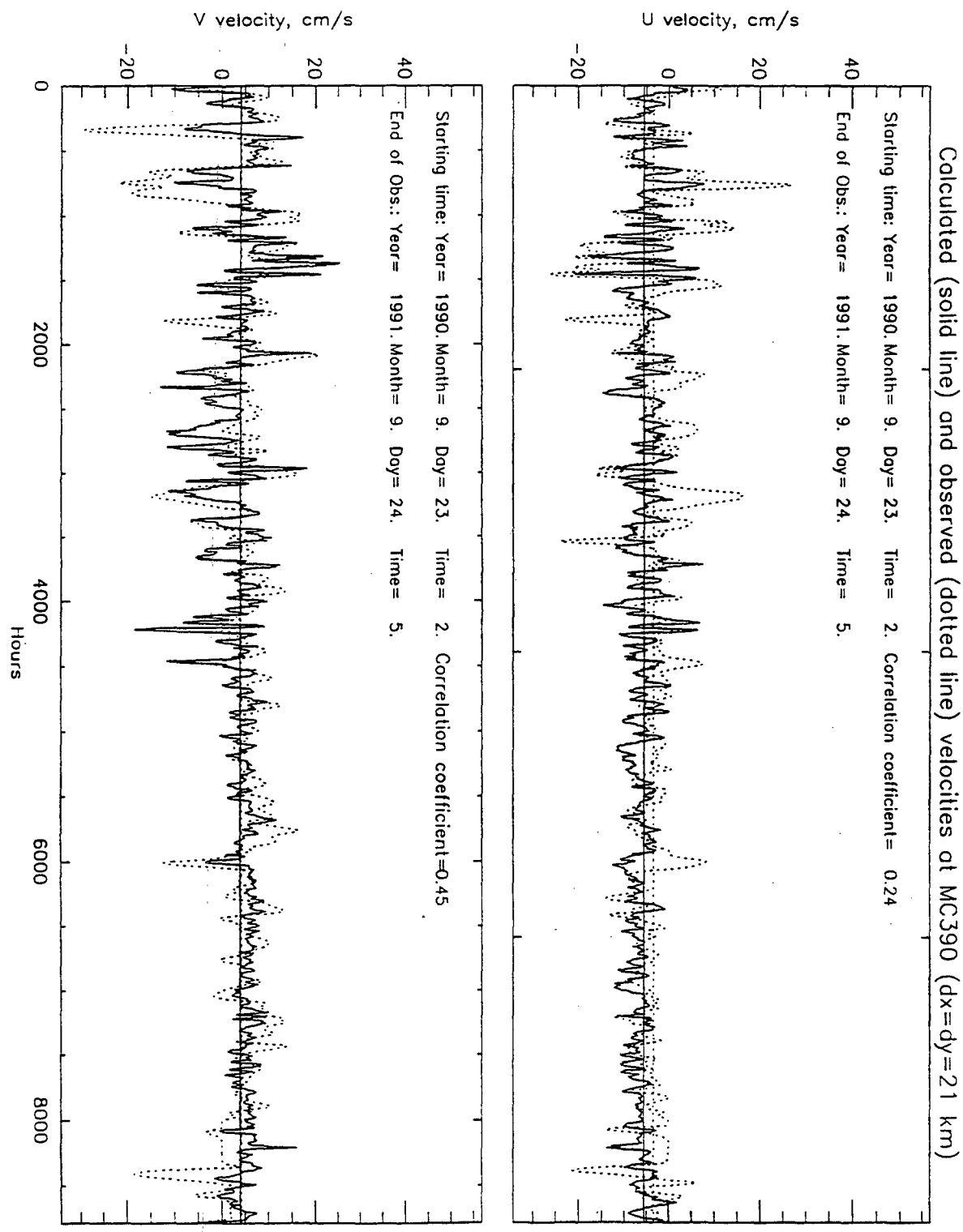

Figure 13. Comparison of the modeled (solid line) and observed (dotted line) current time series using the 21 km grid (a) and the 7 km grid (b) at mooring station MC390. The upper panel in each plot shows the east-west (u) velocity component and the lower panel shows the north-south (v) velocity component.

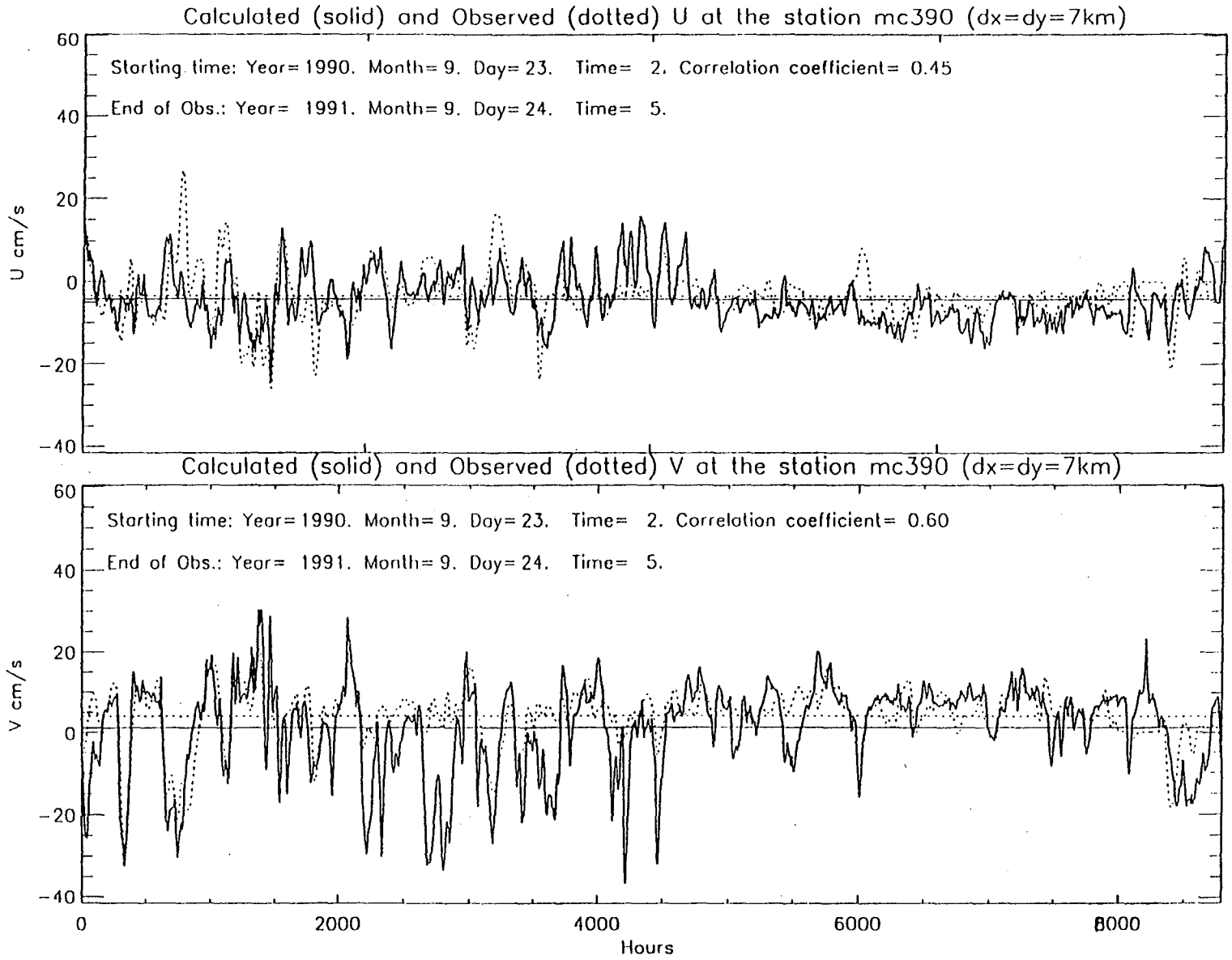

Figure 13b. Station MC390 for the 7 km grid.

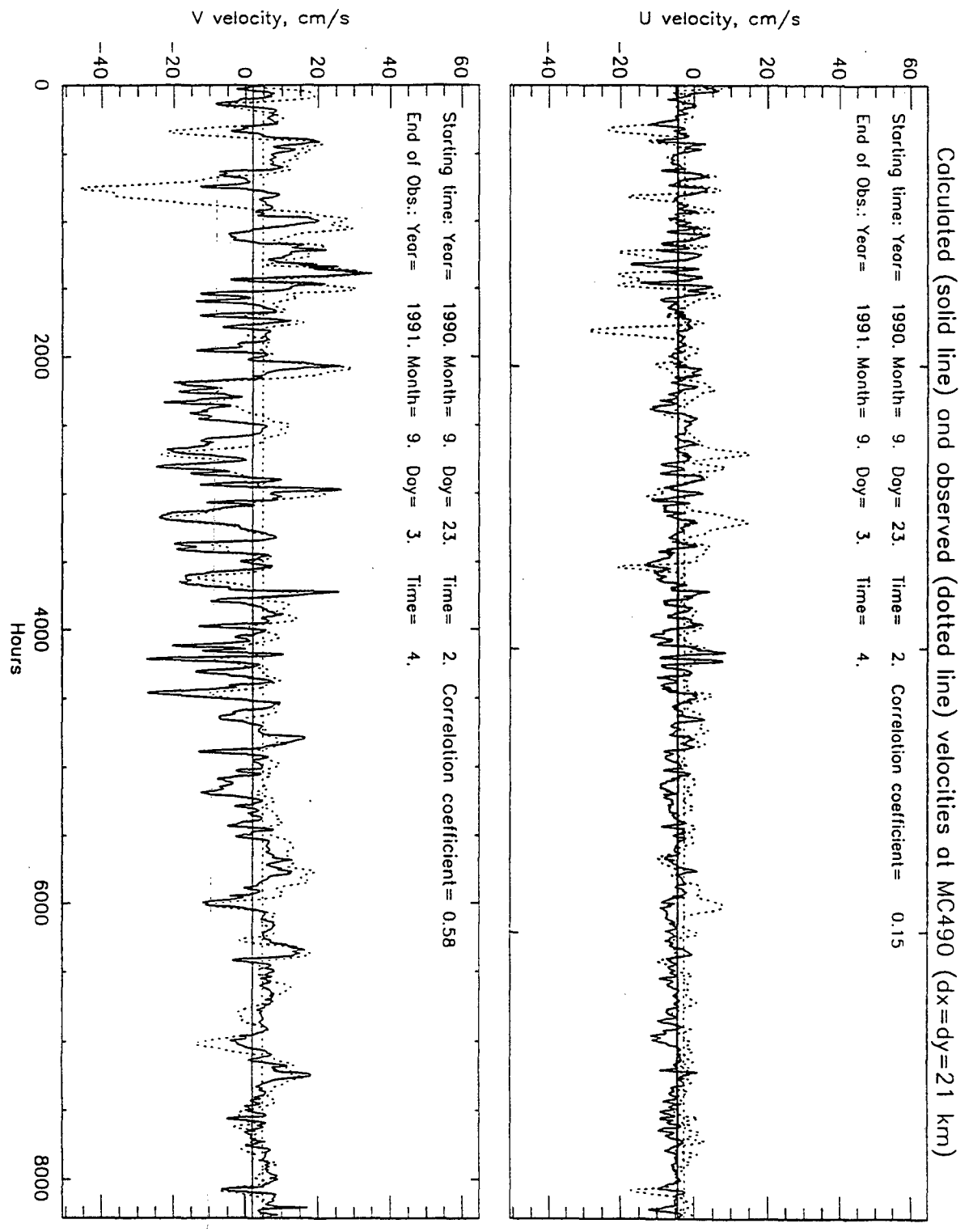

Figure 14. Comparison of the modeled (solid line) and observed (dotted line) current time series using the 21 km grid (a) and the 7 km grid (b) at mooring station MC490. The upper panel in each plot shows the east-west (u) velocity component and the lower panel shows the north-south (v) velocity component.

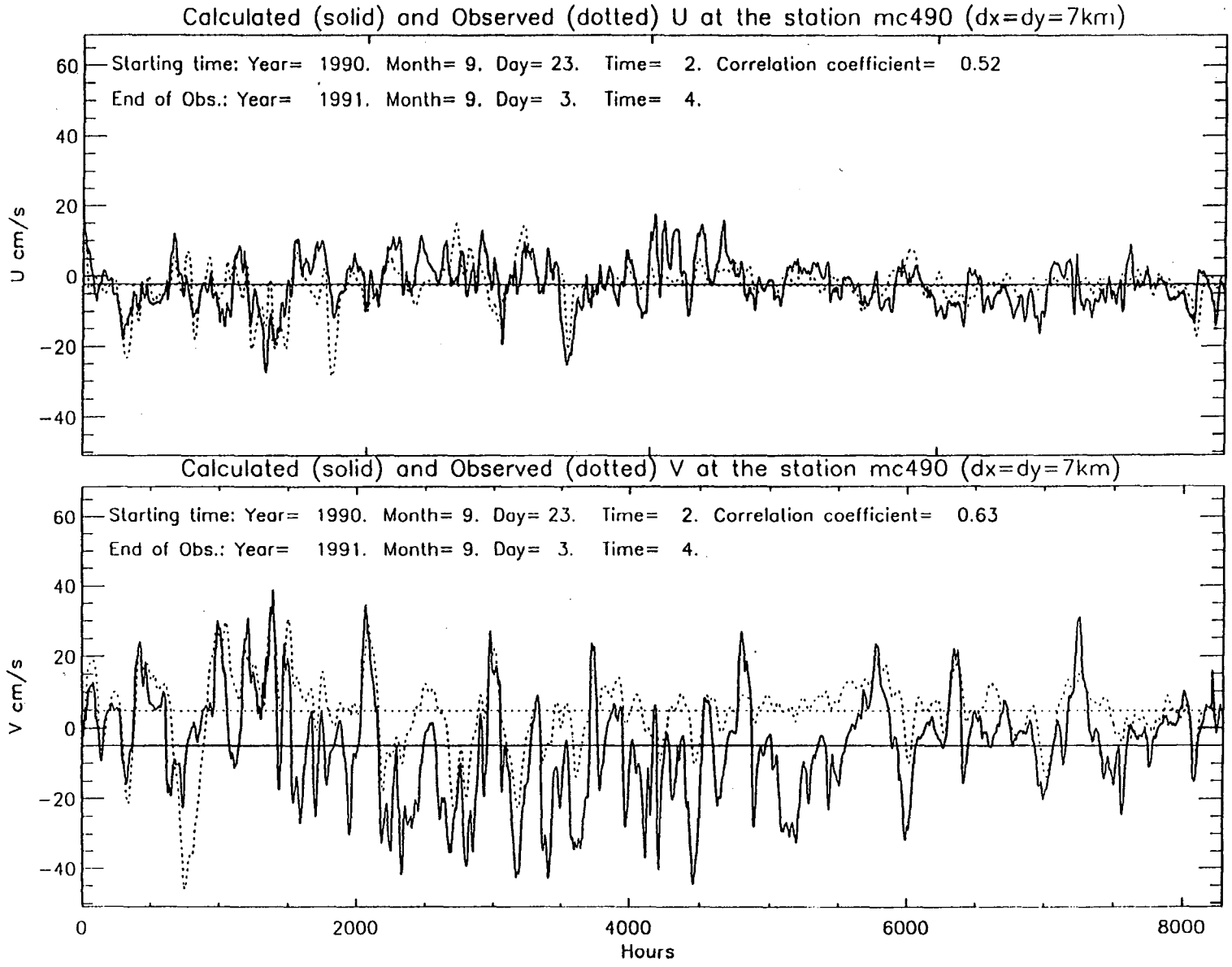

Figure 14b. Station MC490 for the 7 km grid.

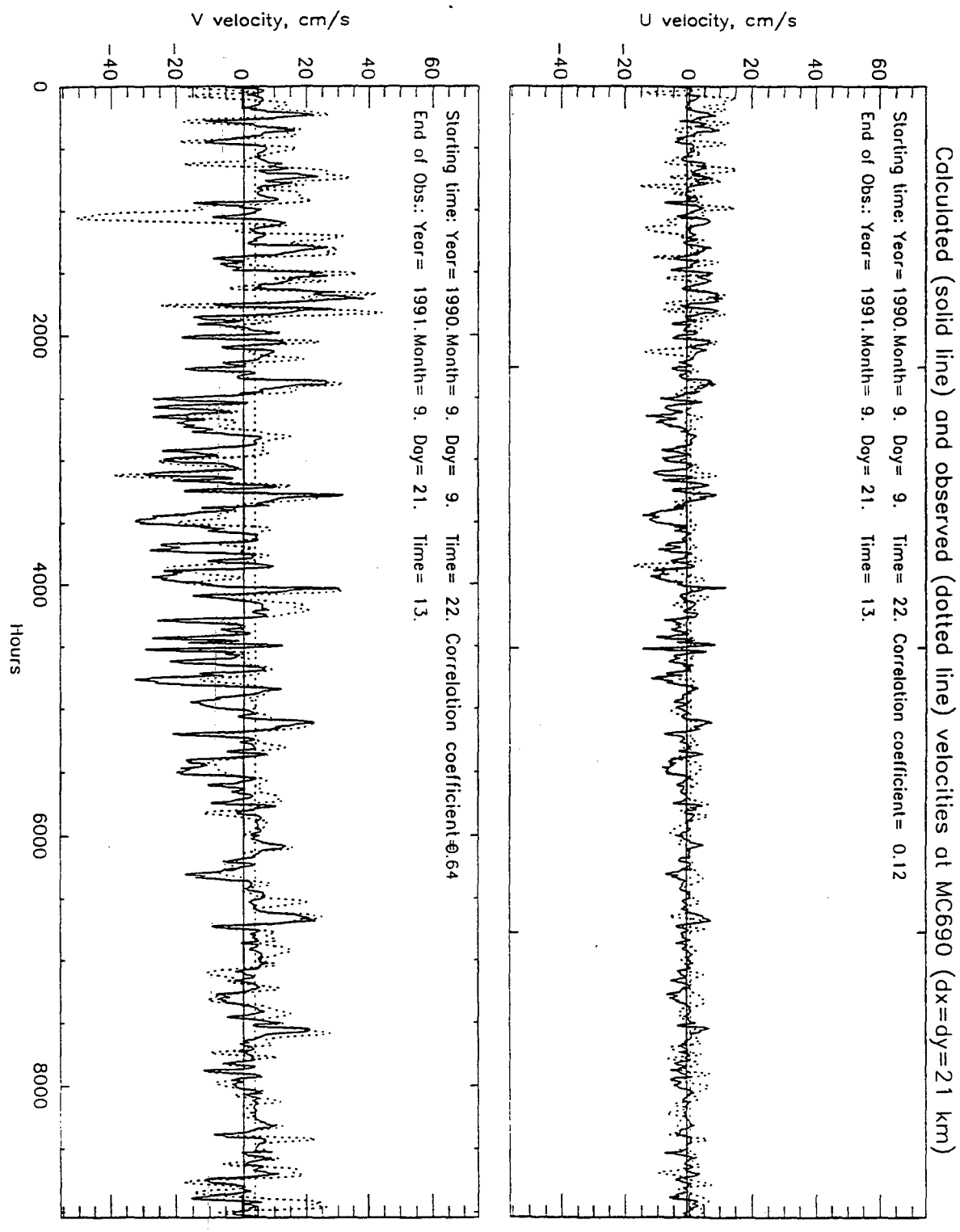

Figure 15. Comparison of the modeled (solid line) and observed (dotted line) current time series using the 21 km grid (a) and the 7 km grid (b) at mooring station MC690. The upper panel in each plot shows the east-west (u) velocity component and the lower panel shows the north-south (v) velocity component.

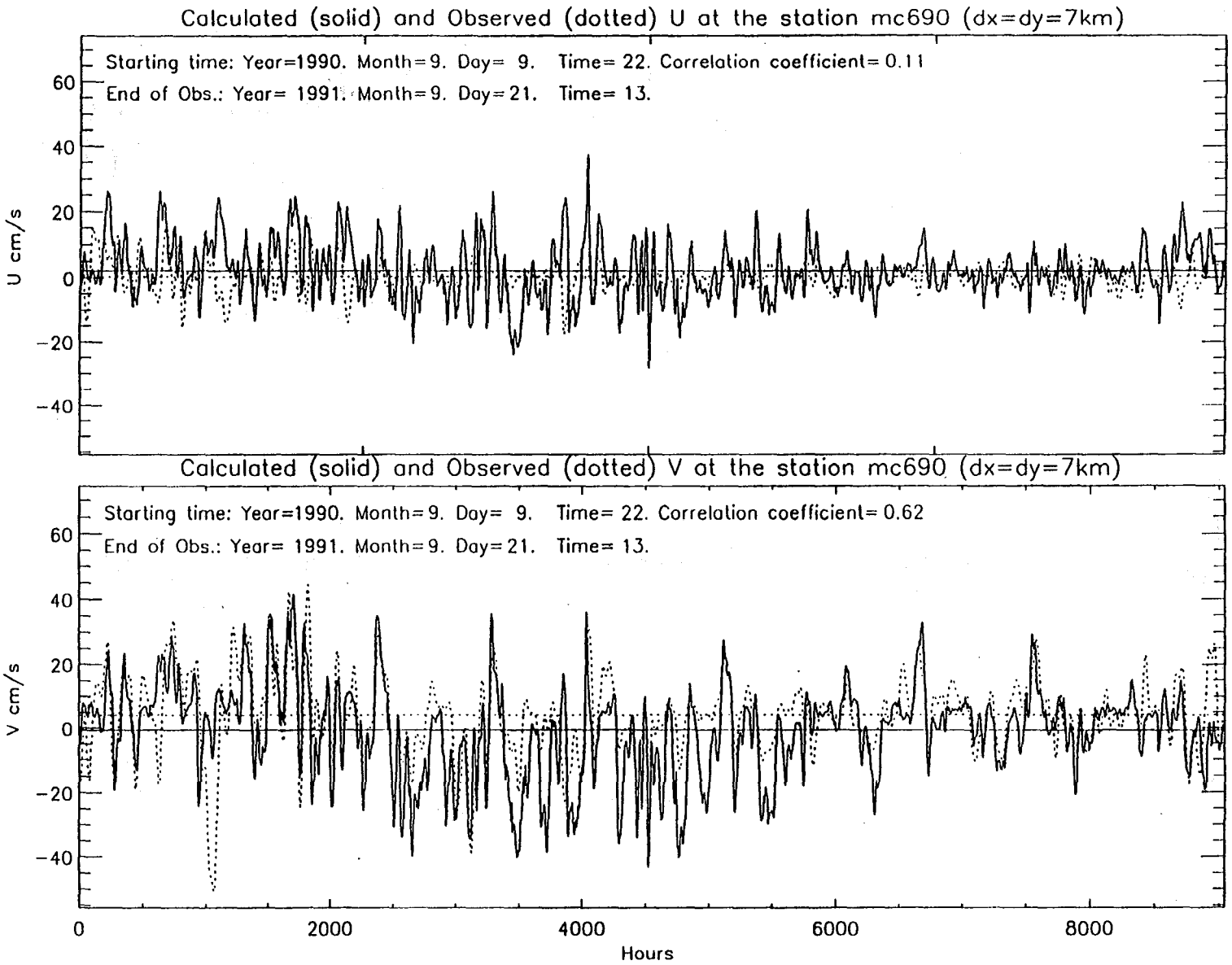

Figure 15b. Station MC690 for the 7 km grid.

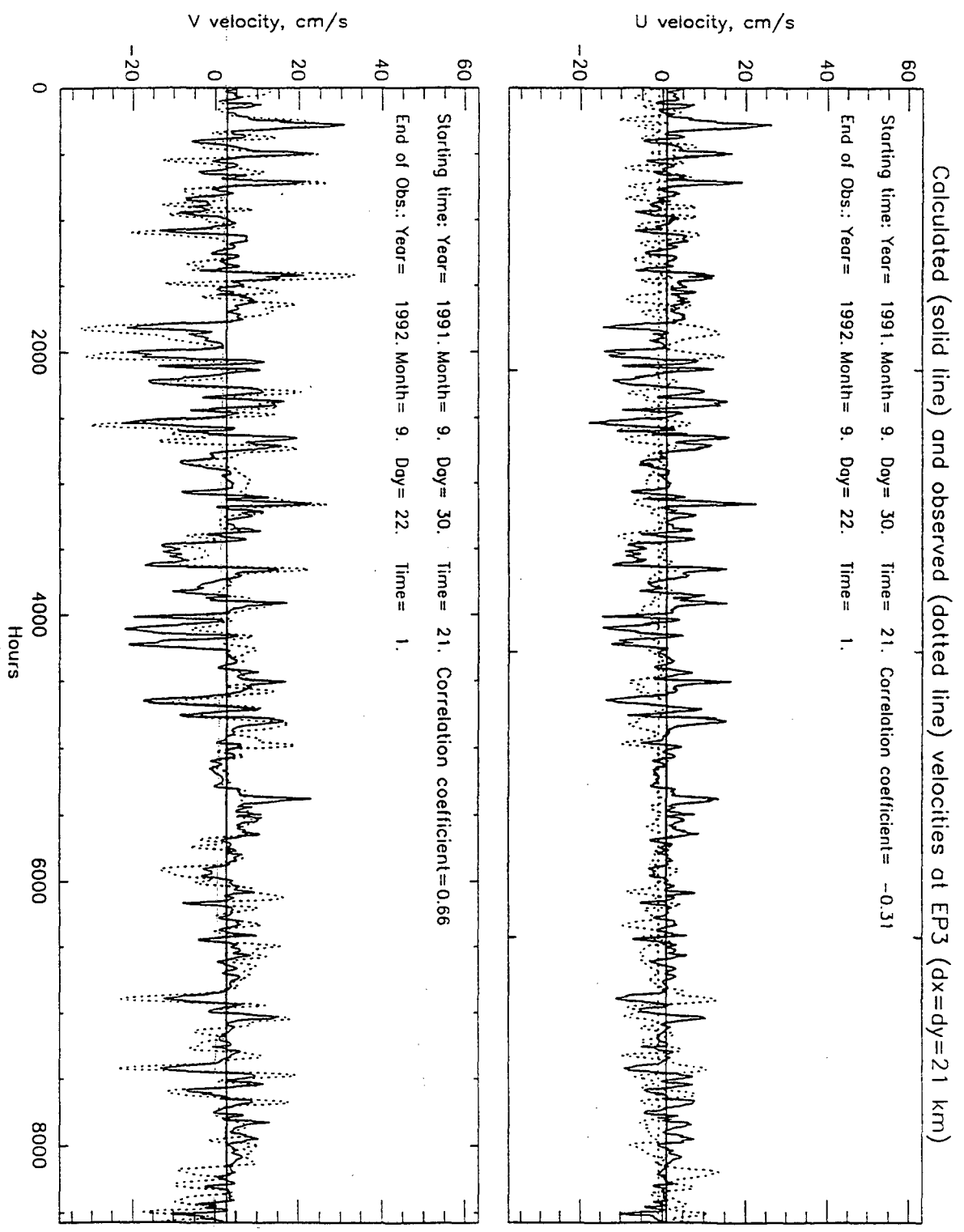

Figure 16. Comparison of the modeled (solid line) and observed (dotted line) current time series using the 21 km grid (a) and the 7 km grid (b) at mooring station EP3. The upper panel in each plot shows the east-west (u) velocity component and the lower panel shows the north-south (v) velocity component.

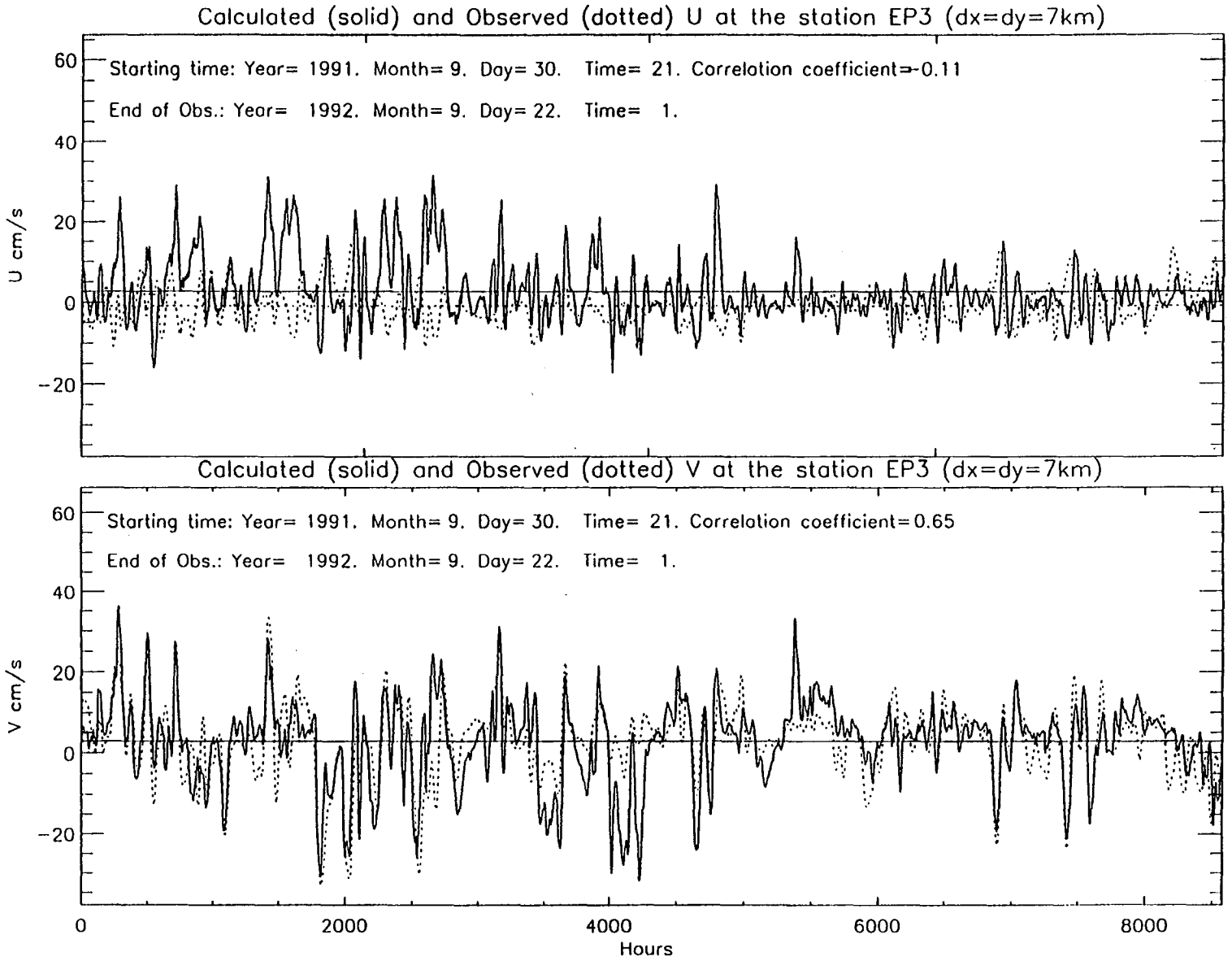

Figure 16b. Station EP3 for the 7 km grid.

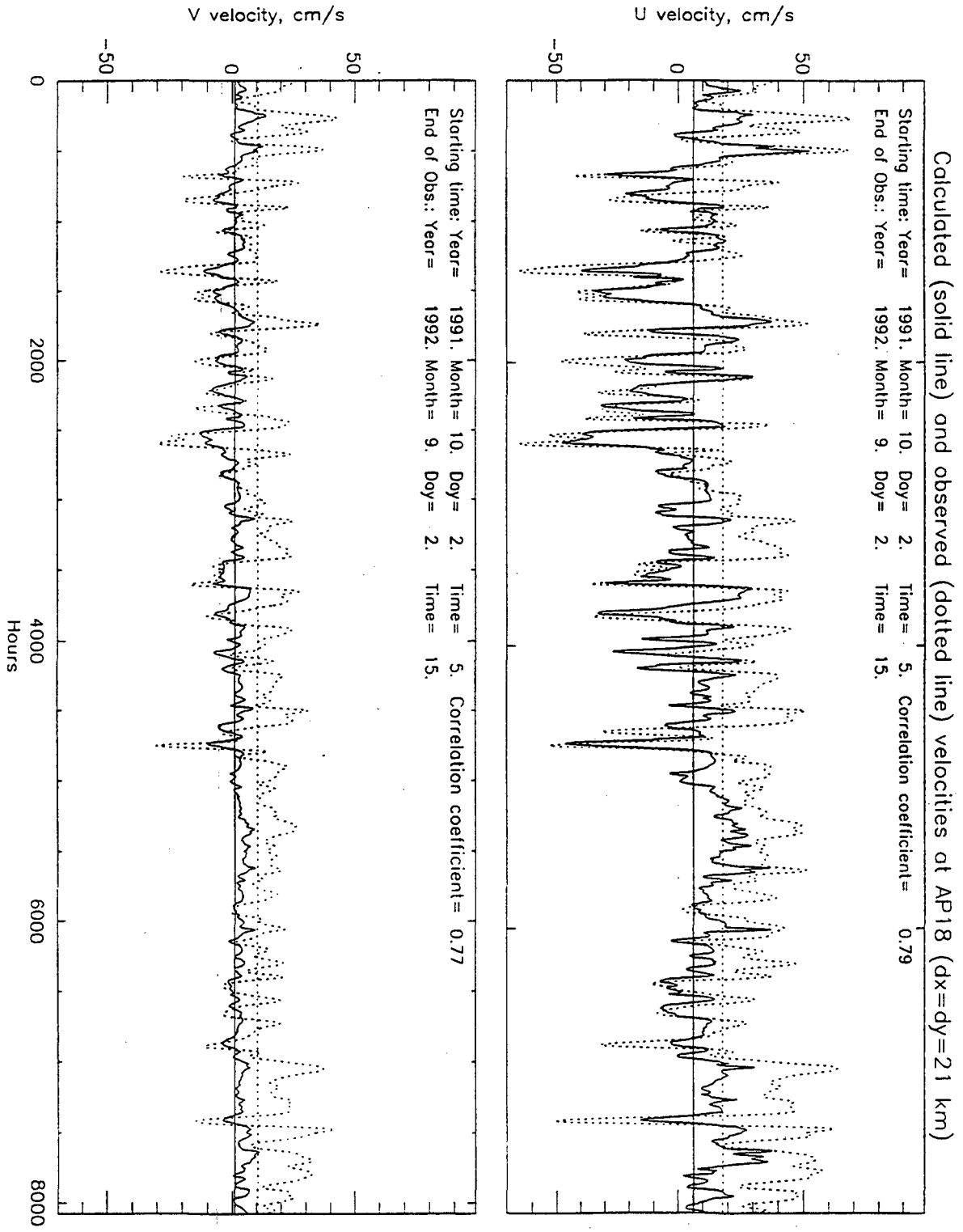

Figure 17. Comparison of the modeled (solid line) and observed (dotted line) current time series using the 21 km grid (a) and the 7 km grid (b) at mooring station AP18. The upper panel in each plot shows the east-west (u) velocity component and the lower panel shows the north-south (v) velocity component.

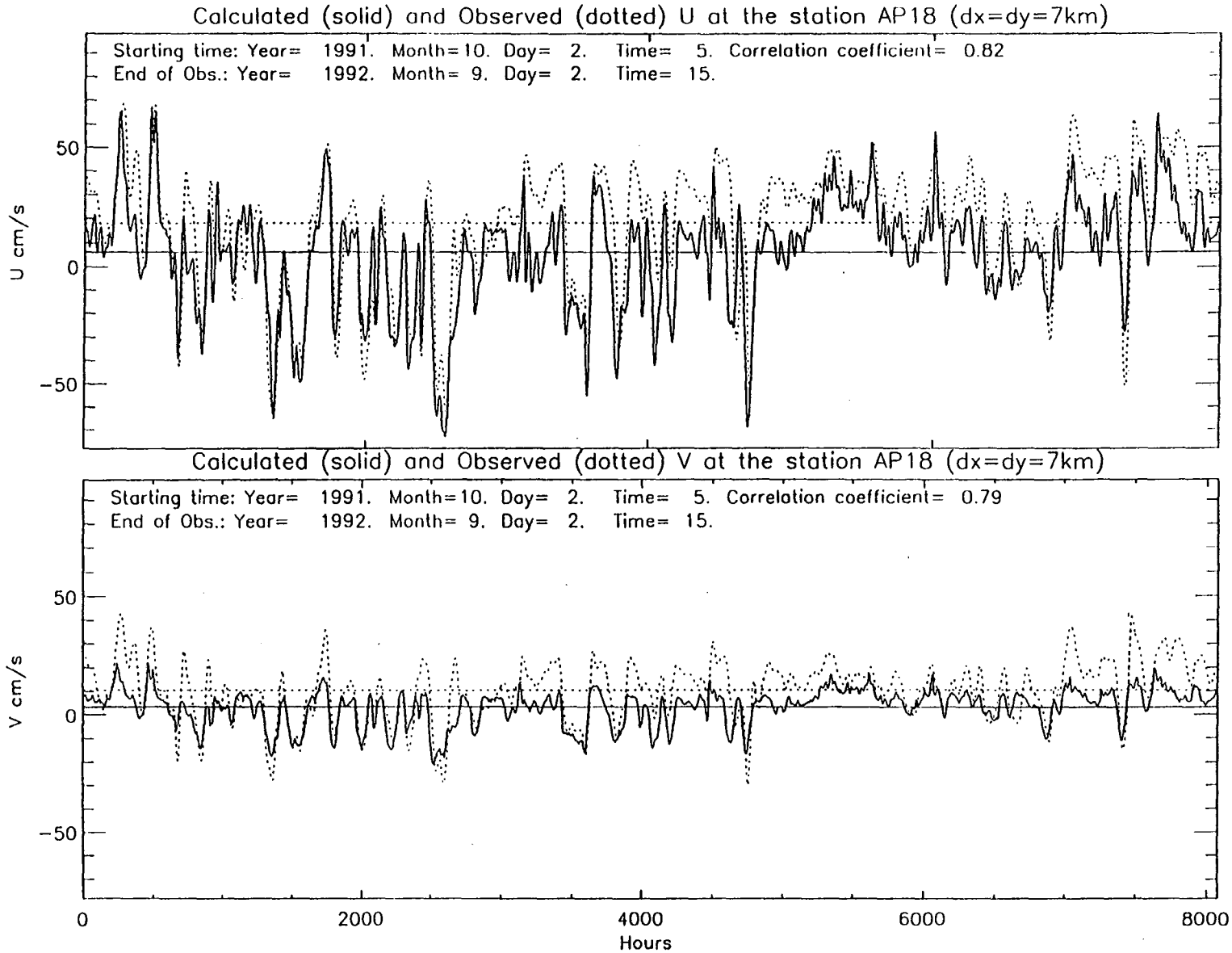

Figure 17b. Station AP18 for the 7 km grid.

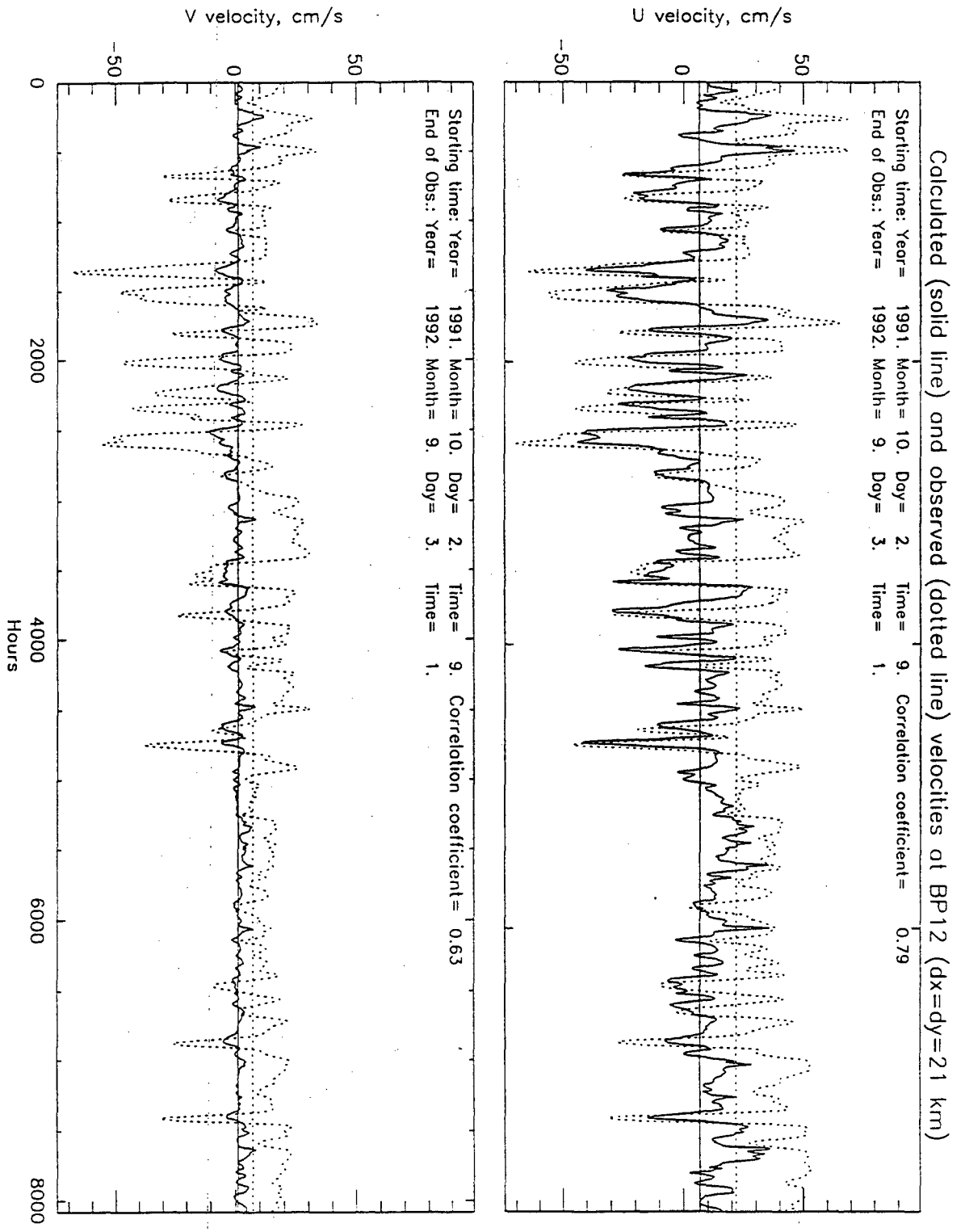

Figure 18. Comparison of the modeled (solid line) and observed (dotted line) current time series using the 21 km grid (a) and the 7 km grid (b) at mooring station BP12. The upper panel in each plot shows the east-west (u) velocity component and the lower panel shows the north-south (v) velocity component.

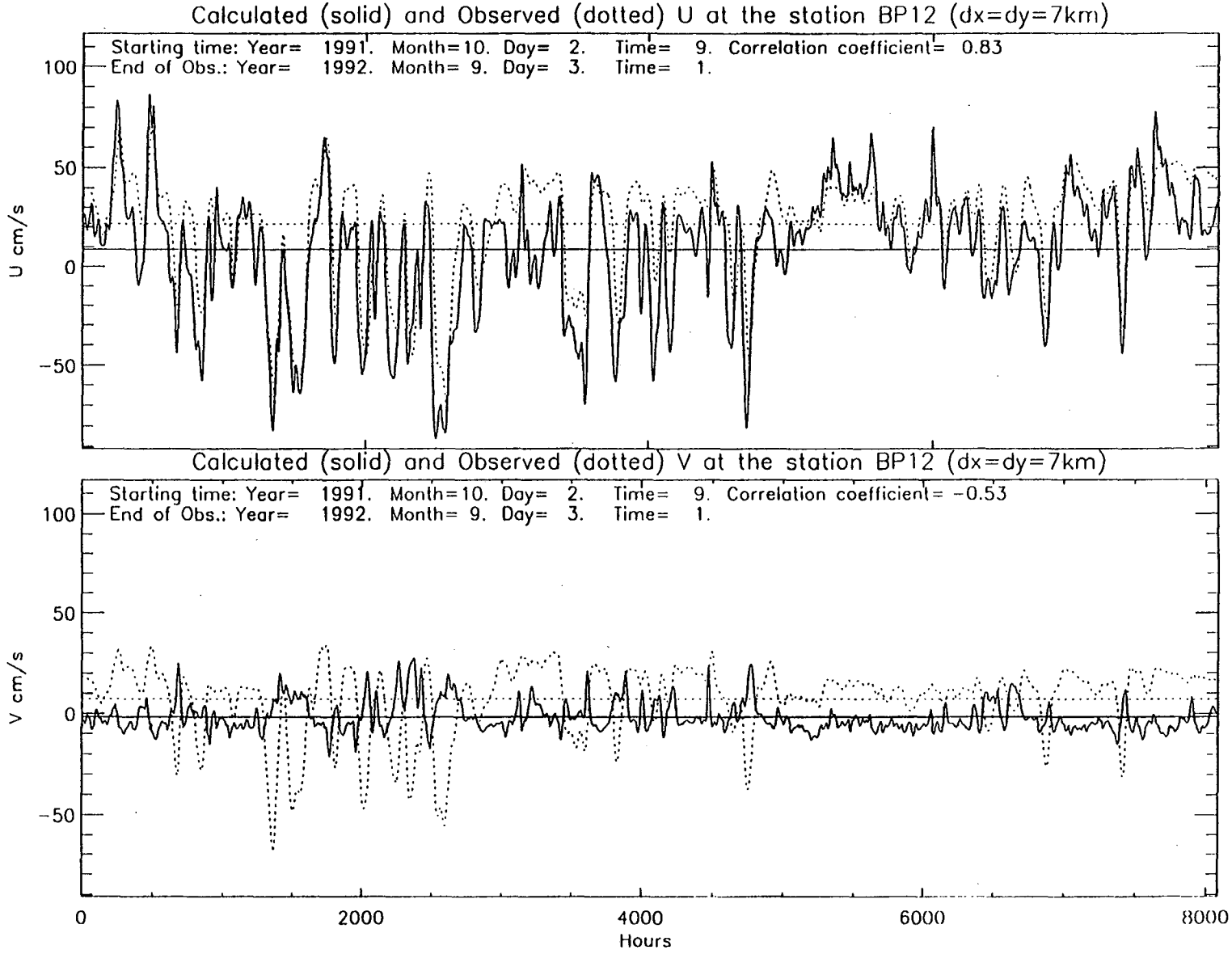

Figure 18b. Station BP12 for the 7 km grid.

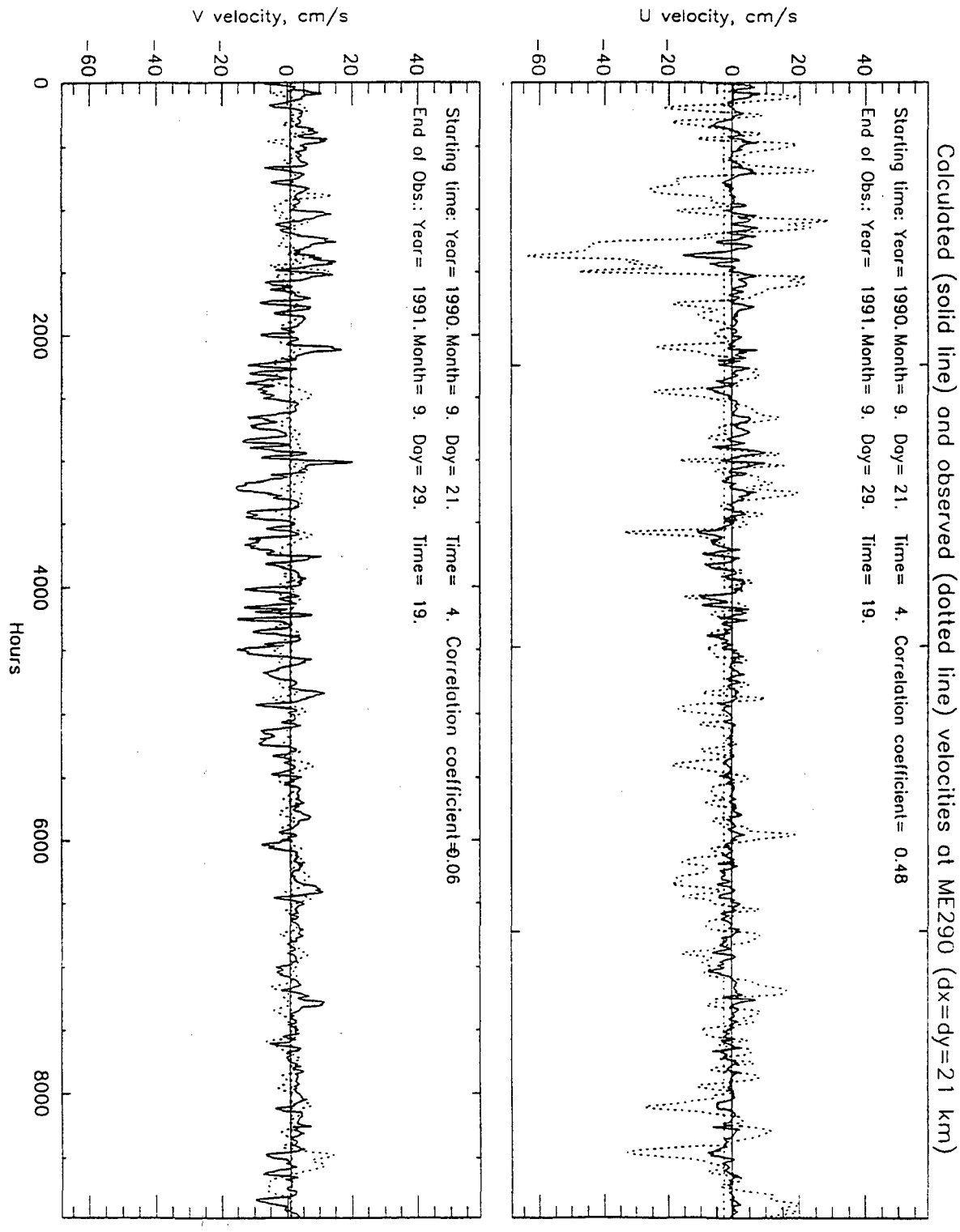

Figure 19. Comparison of the modeled (solid line) and observed (dotted line) current time series using the 21 km grid (a) and the 7 km grid (b) at mooring station ME290. The upper panel in each plot shows the east-west (u) velocity component and the lower panel shows the north-south (v) velocity component.

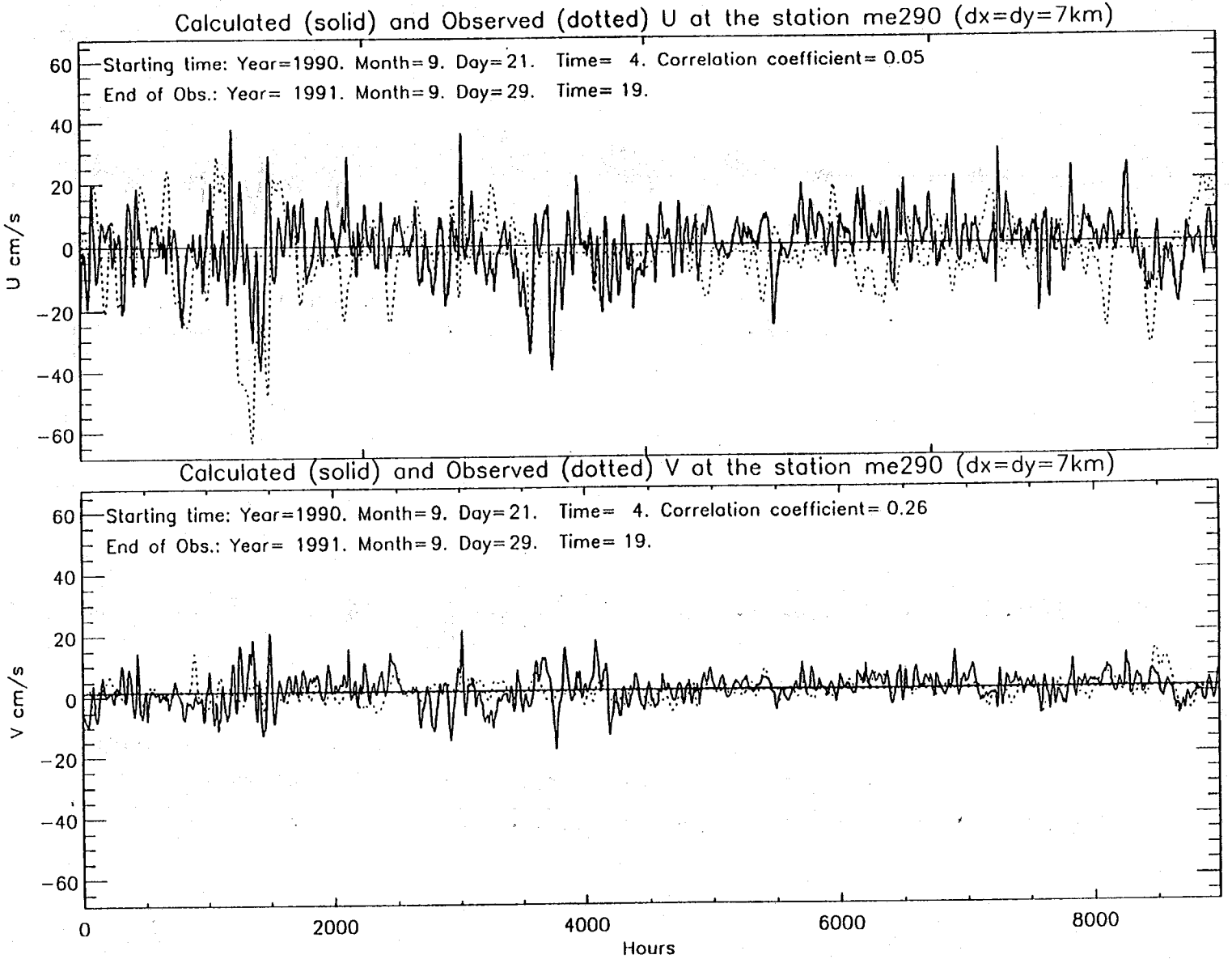

Figure 19b. Station ME290 for the 7 km grid.

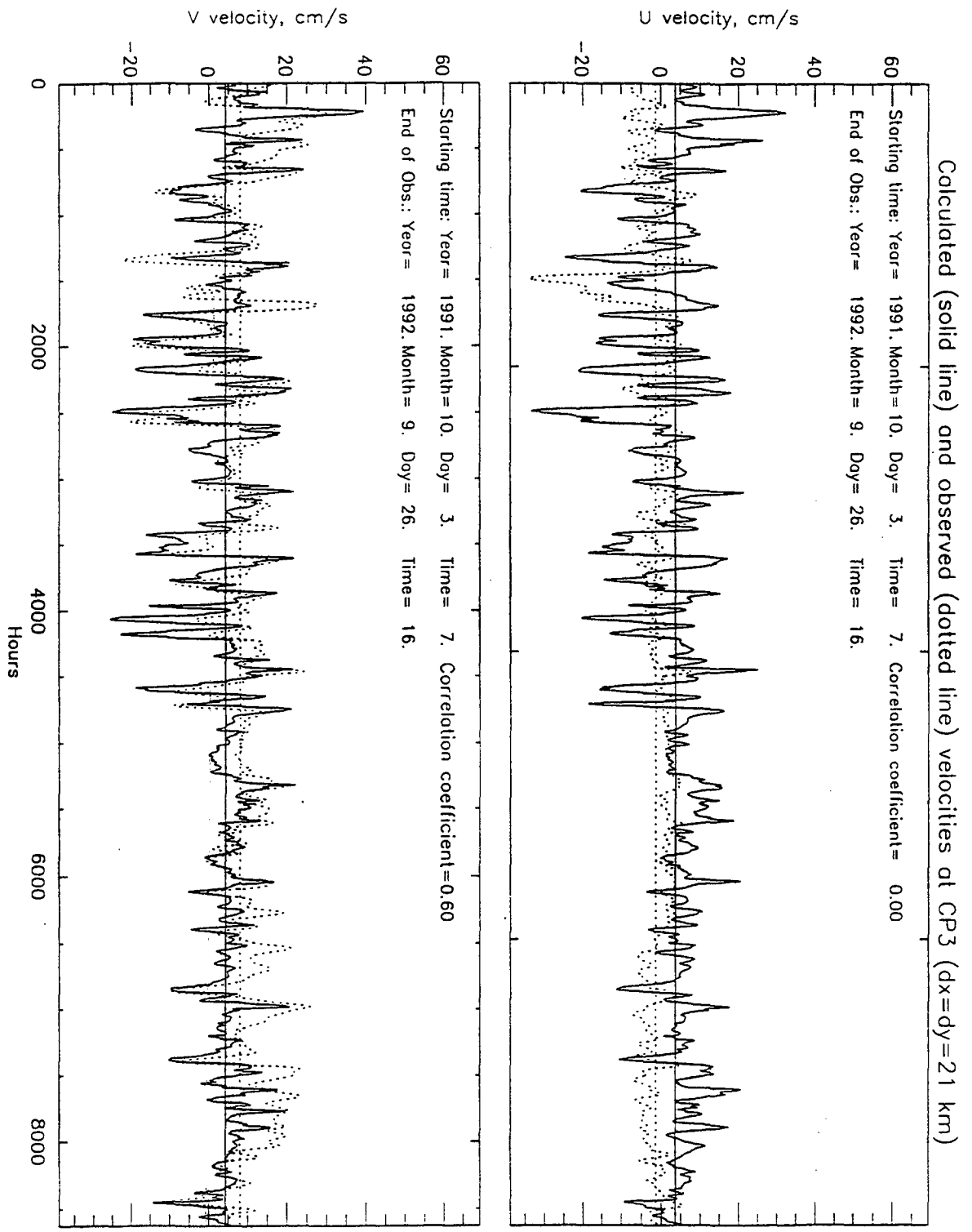

Figure 20. Comparison of the modeled (solid line) and observed (dotted line) current time series using the 21 km grid (a) and the 7 km grid (b) at mooring station CP3. The upper panel in each plot shows the east-west (u) velocity component and the lower panel shows the north-south (v) velocity component.

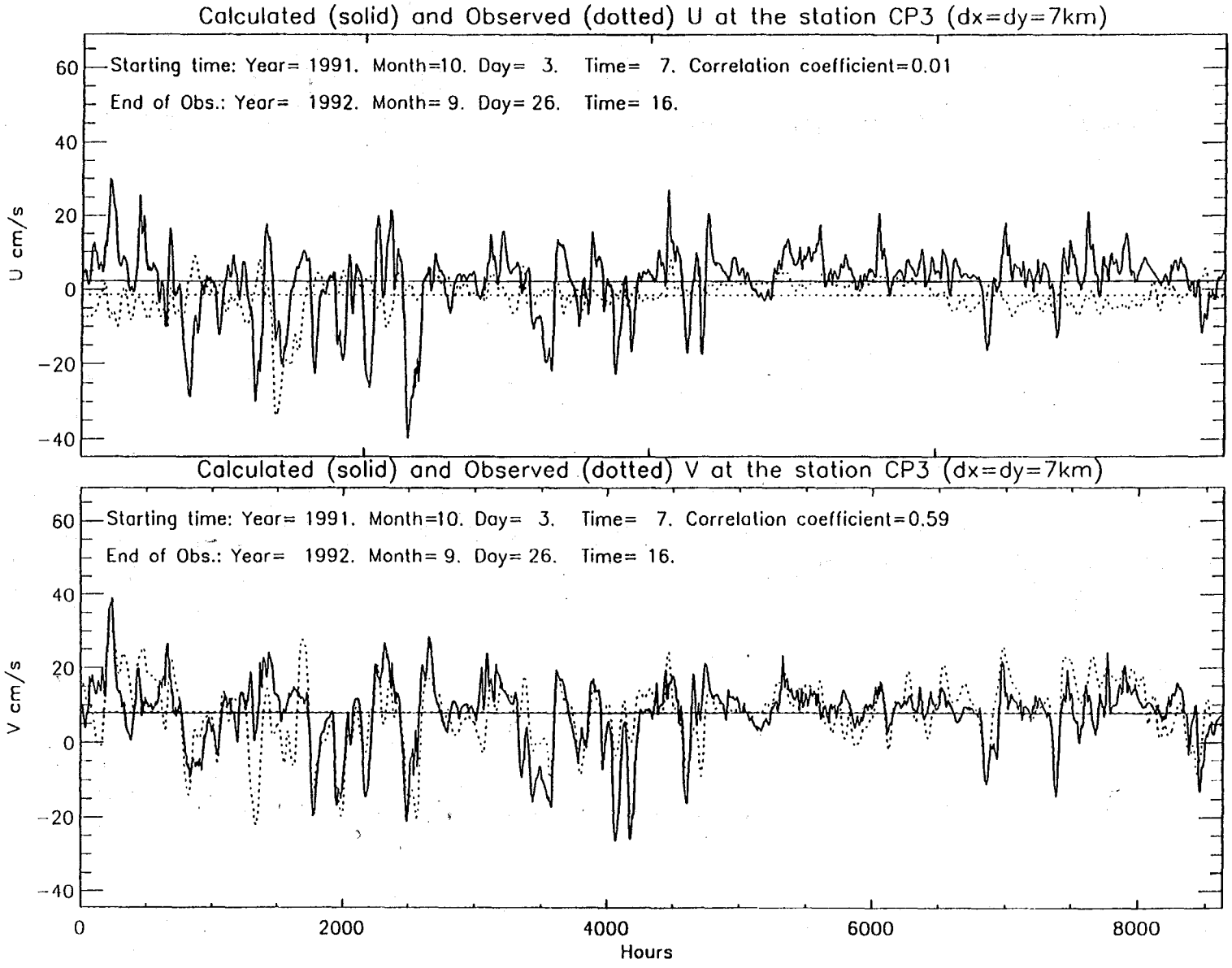

Figure 20b. Station CP3 for the 7 km grid.

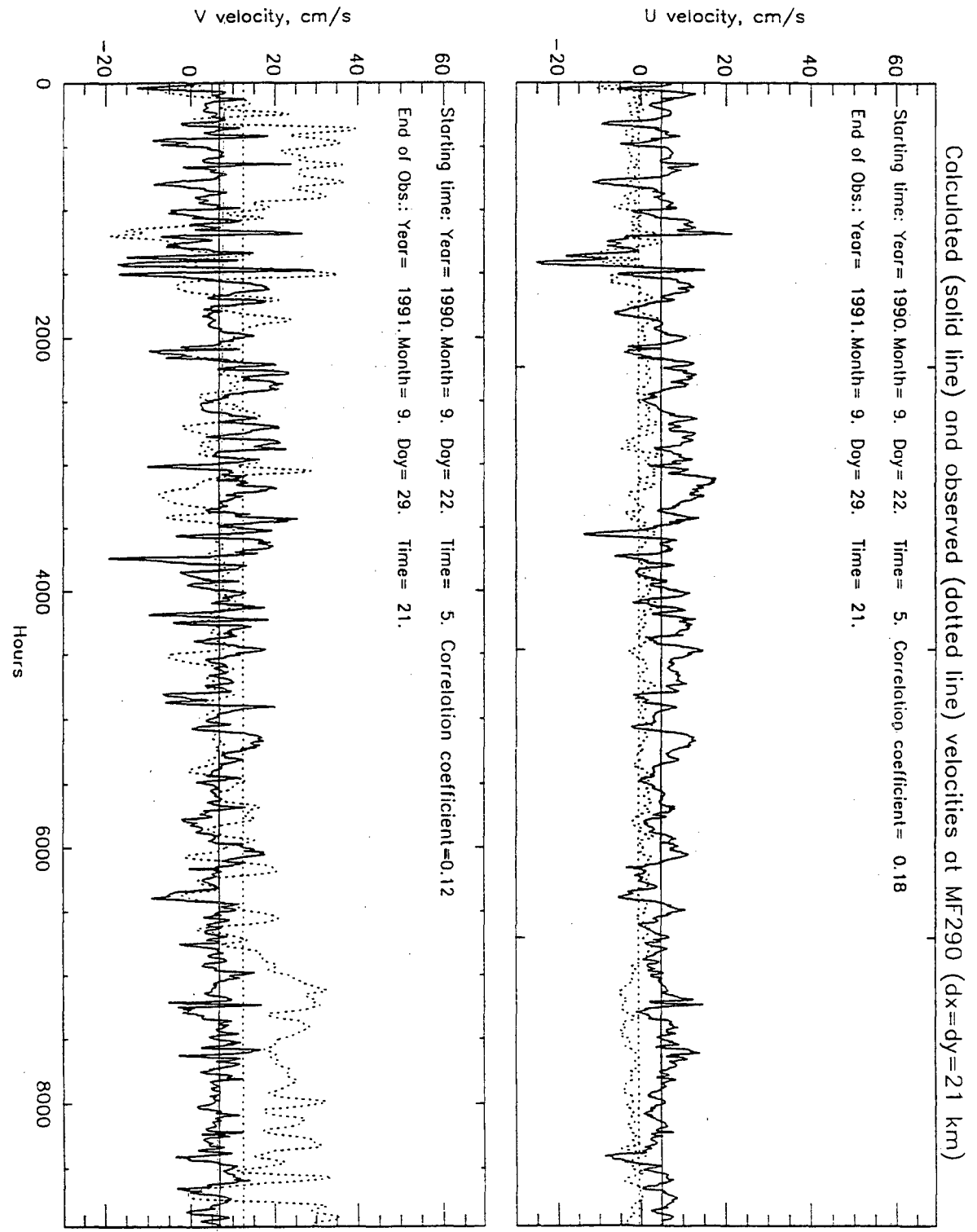

Figure 21. Comparison of the modeled (solid line) and observed (dotted line) current time series using the 21 km grid (a) and the 7 km grid (b) at mooring station MF290. The upper panel in each plot shows the east-west (u) velocity component and the lower panel shows the north-south (v) velocity component.

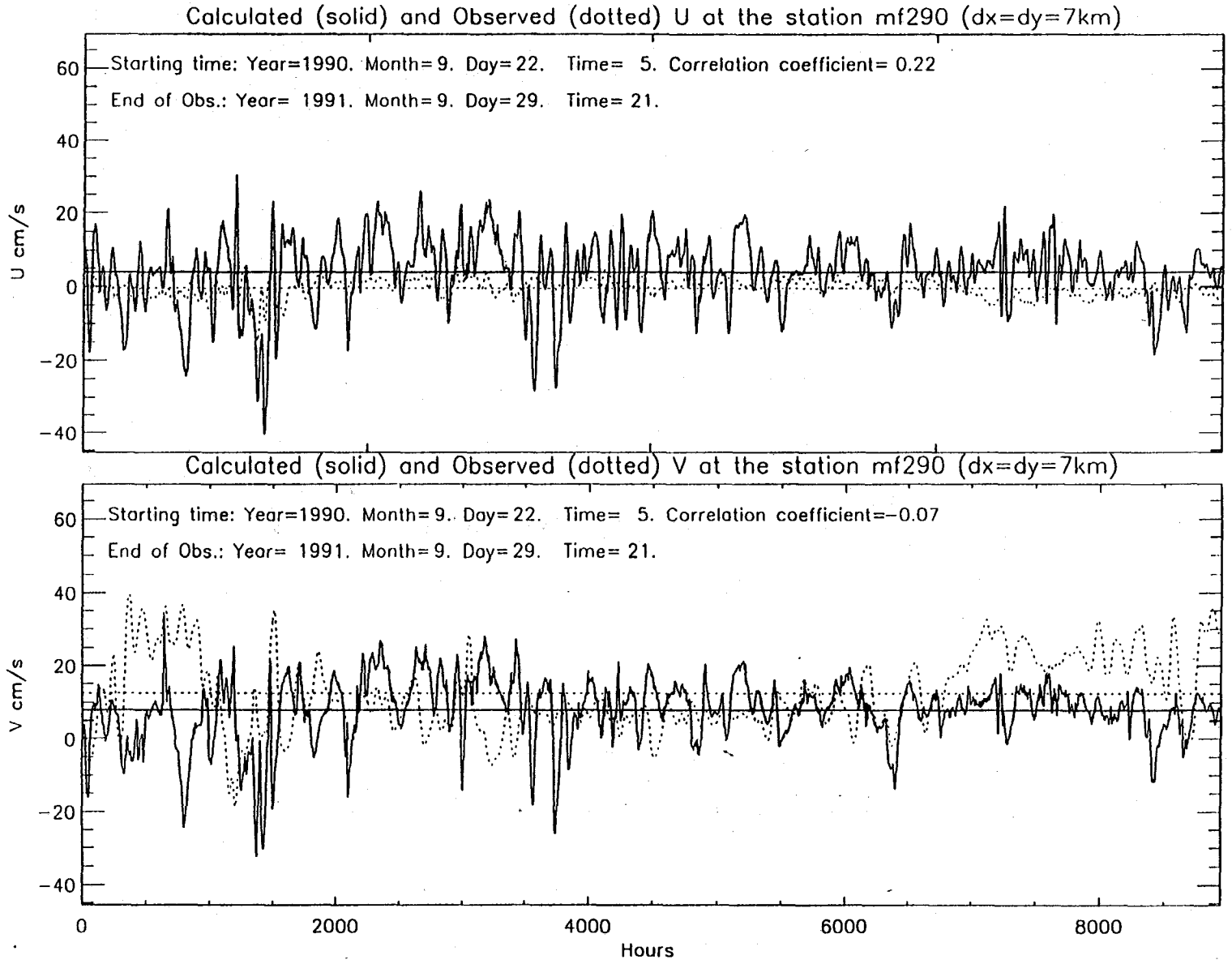

Figure 21b. Station MF290 for the 7 km grid.

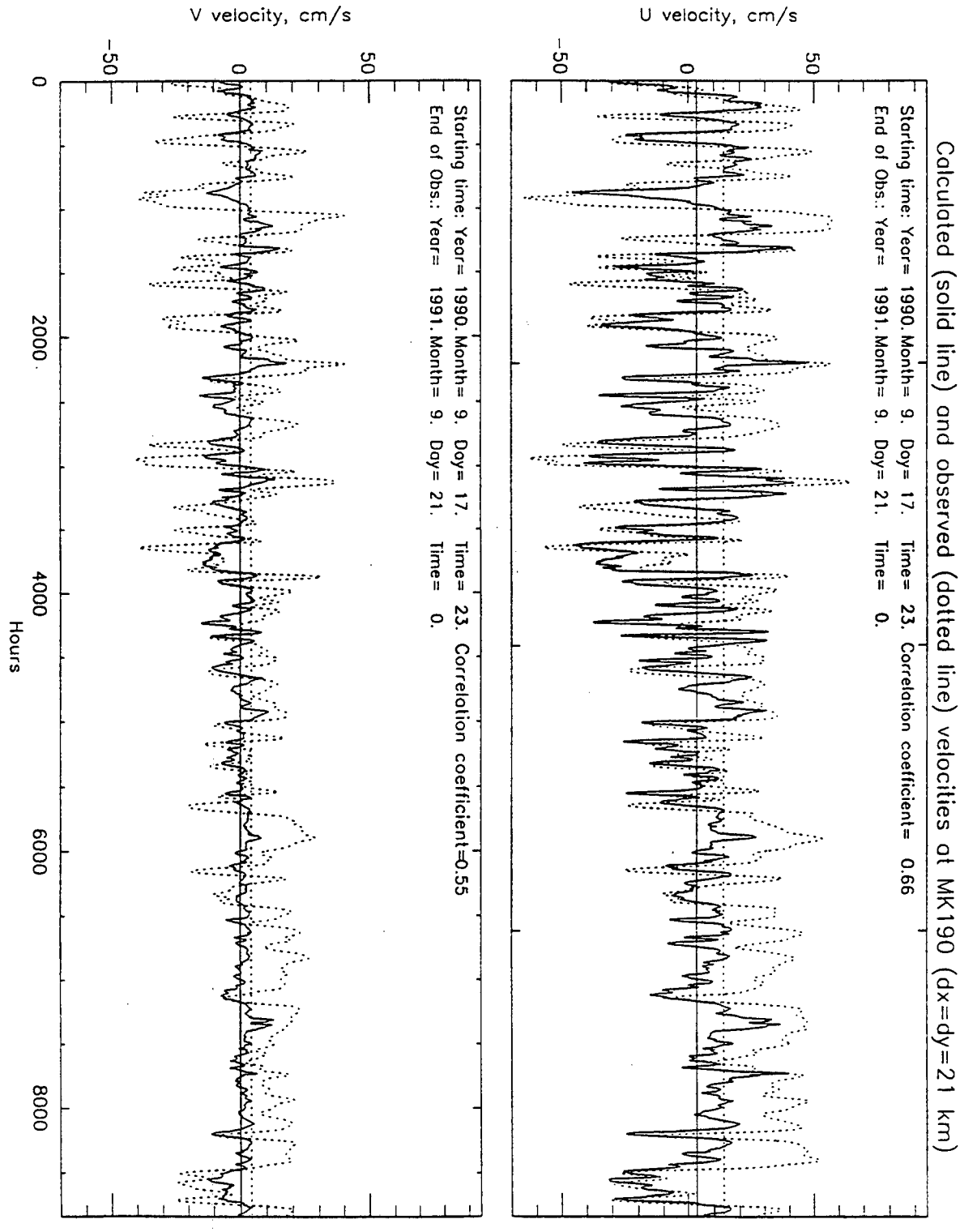

Figure 22. Comparison of the modeled (solid line) and observed (dotted line) current time series using the 21 km grid (a) and the 7 km grid (b) at mooring station MK190. The upper panel in each plot shows the east-west (u) velocity component and the lower panel shows the north-south (v) velocity component.

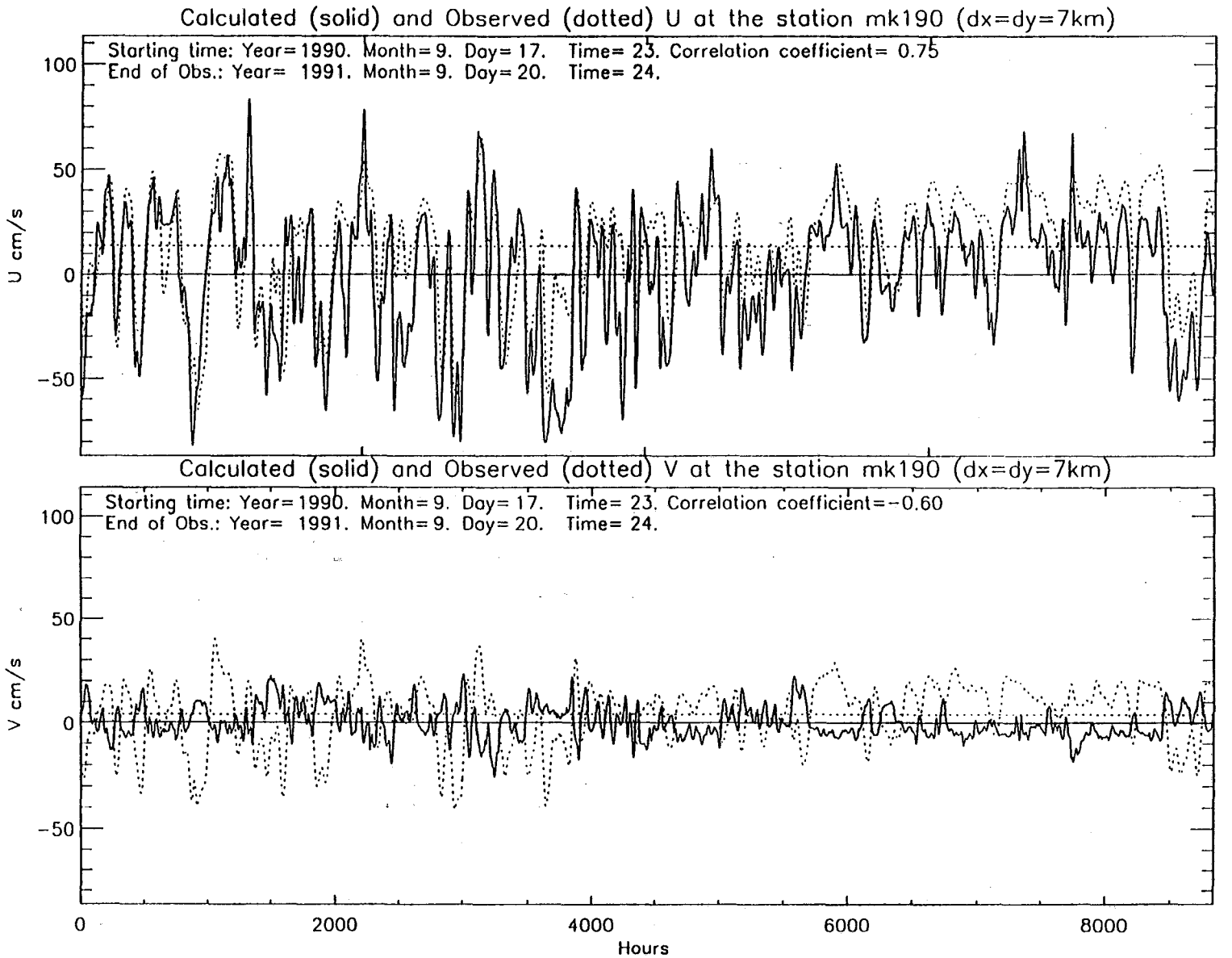

Figure 22b. Station MK190 for the 7 km grid.

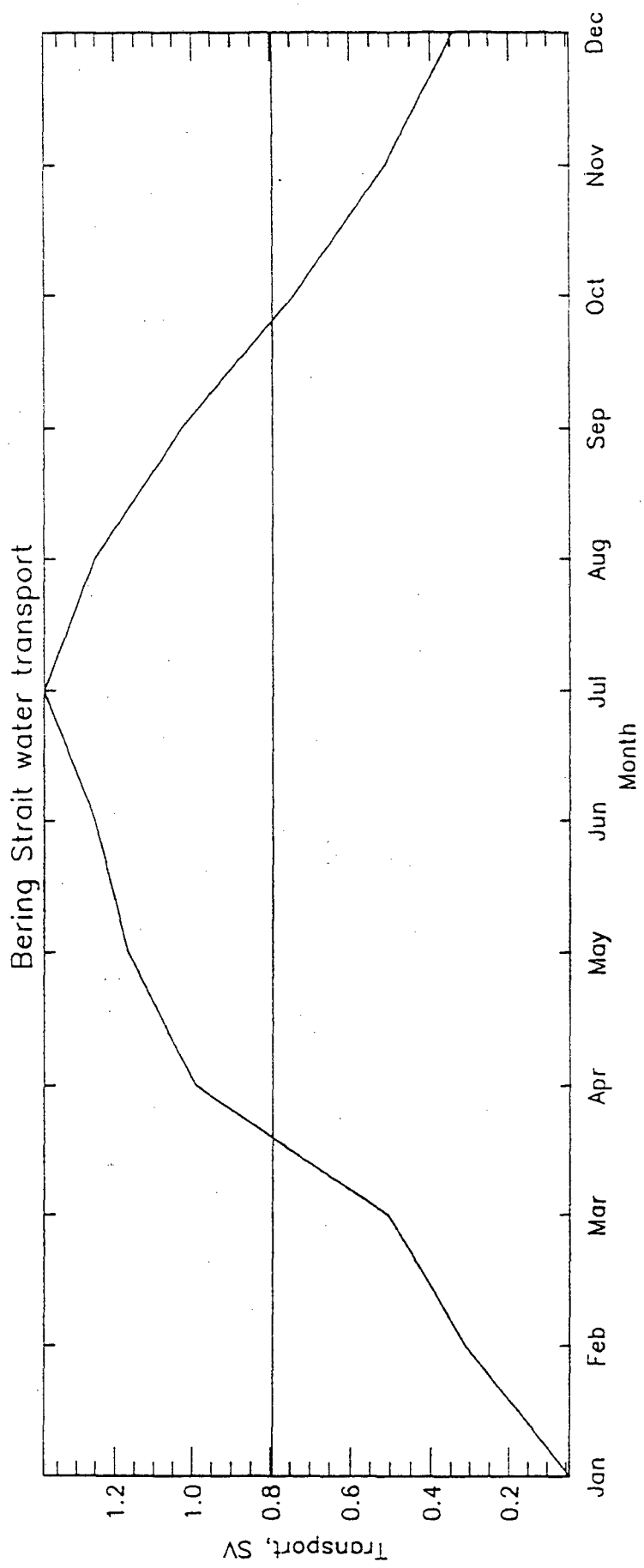

Figure 23. Mean monthly transport averaged over the 15 model years in Bering Strait.

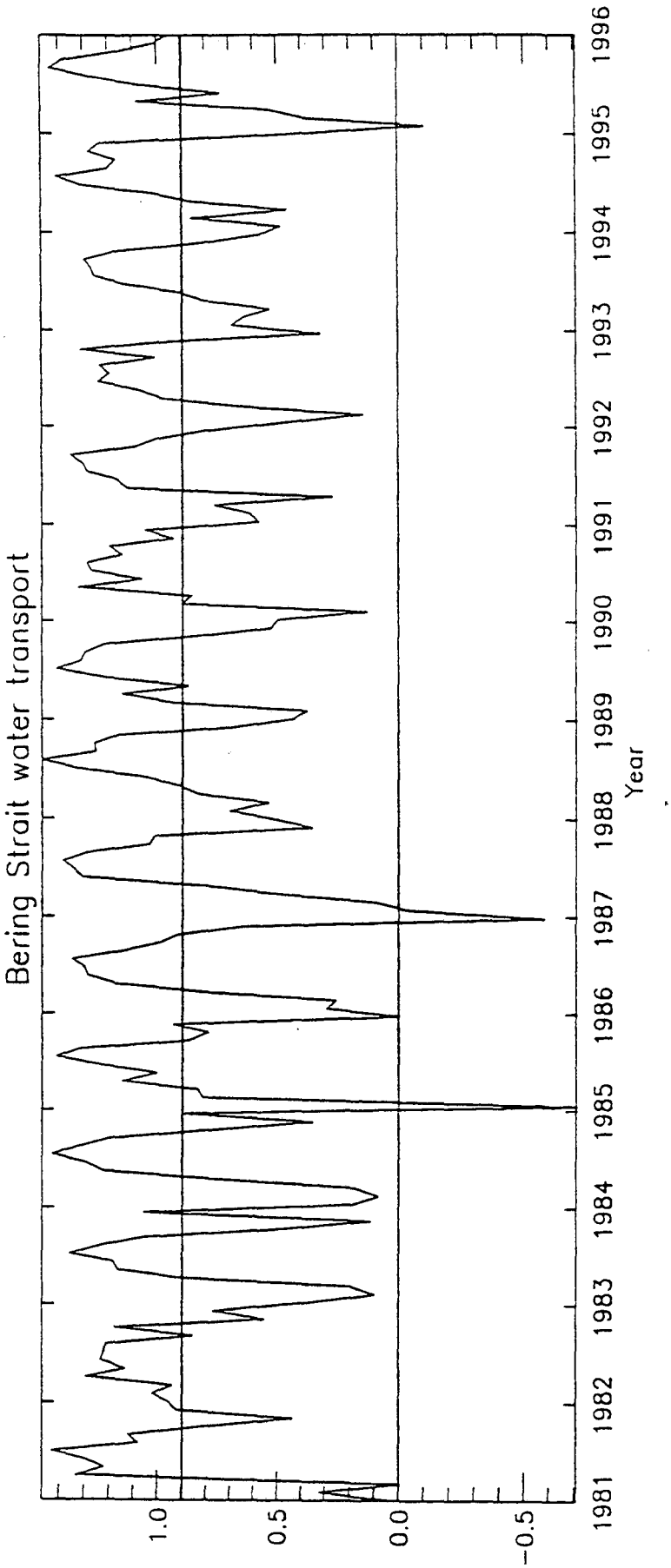

Figure 24. Mean monthly transport for each month of the 15 year run in Bering Strait.

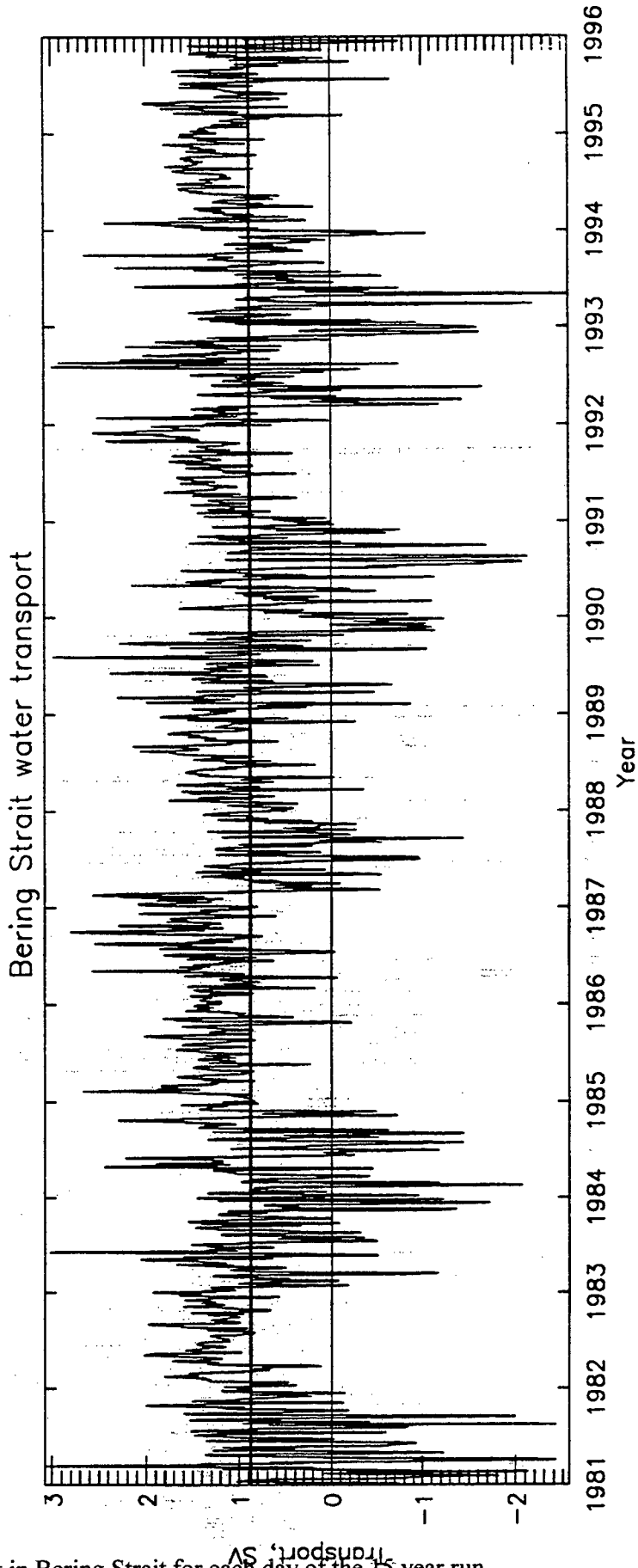

Figure 25. Daily mean transport in Bering Strait for each day of the 15 year run.

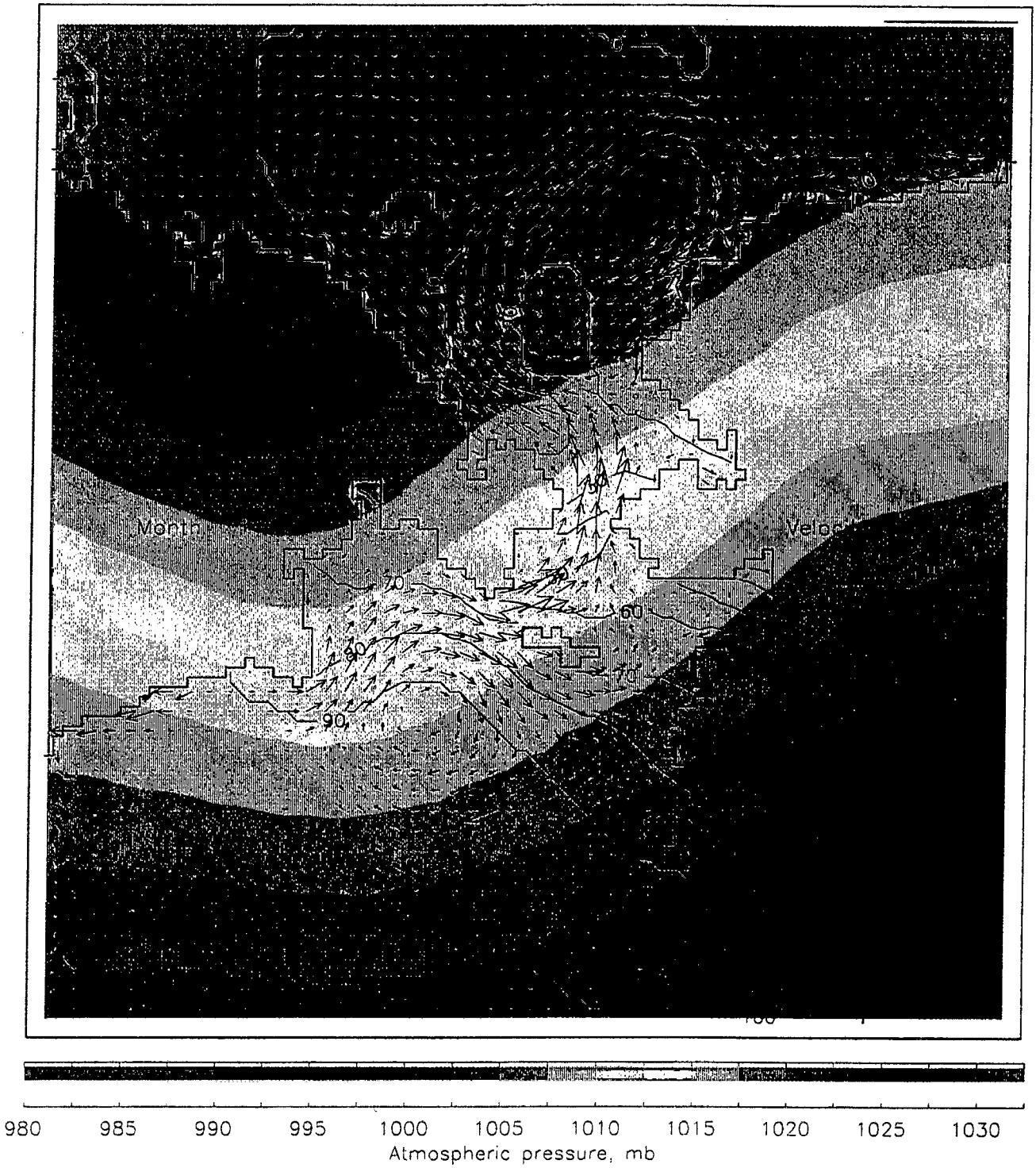

Figure 26. Mean January circulation averaged over the 15 model years using the 21 km grid.

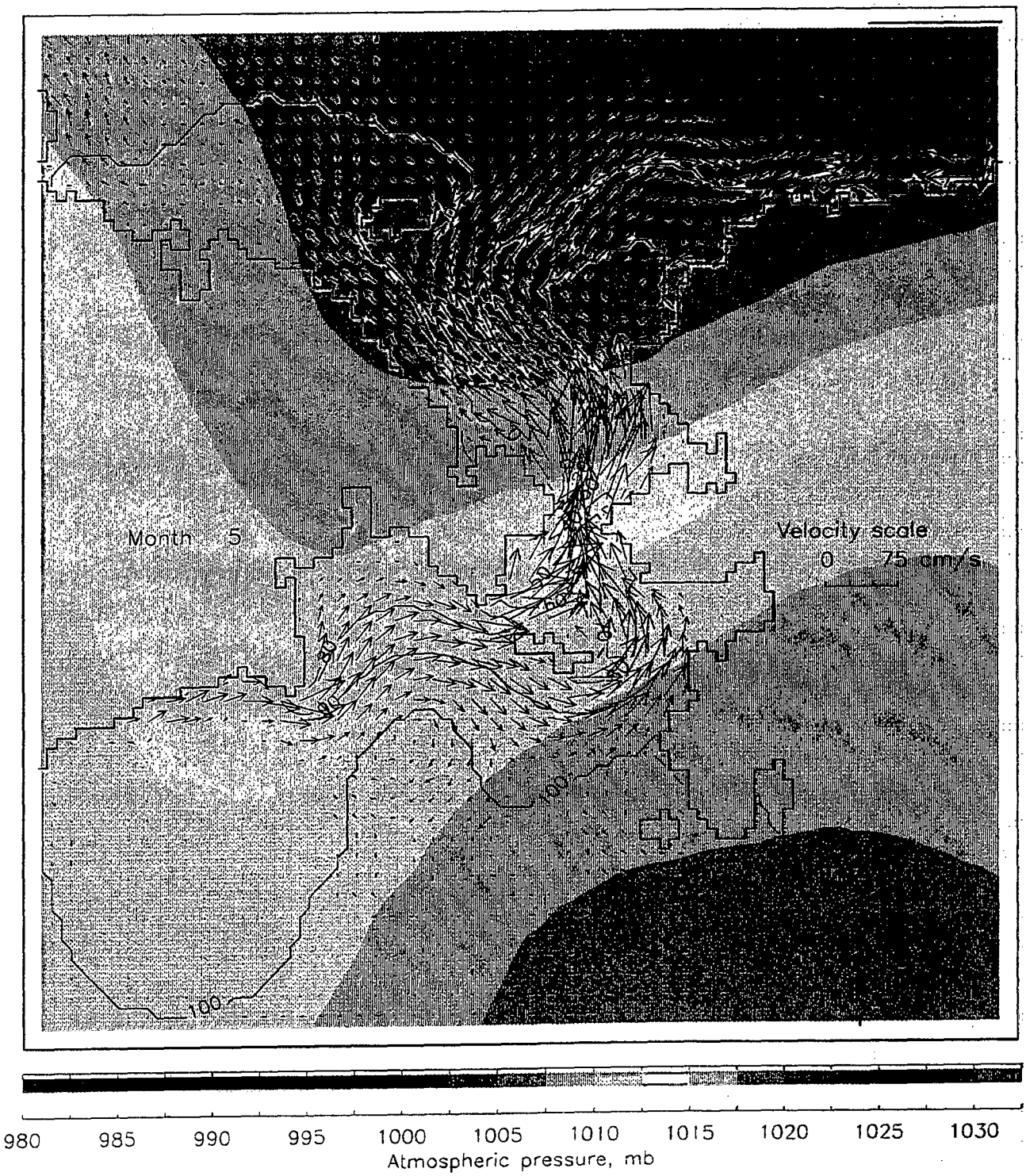

Figure 27. Mean May circulation averaged over the 15 model years using the 21 km grid.

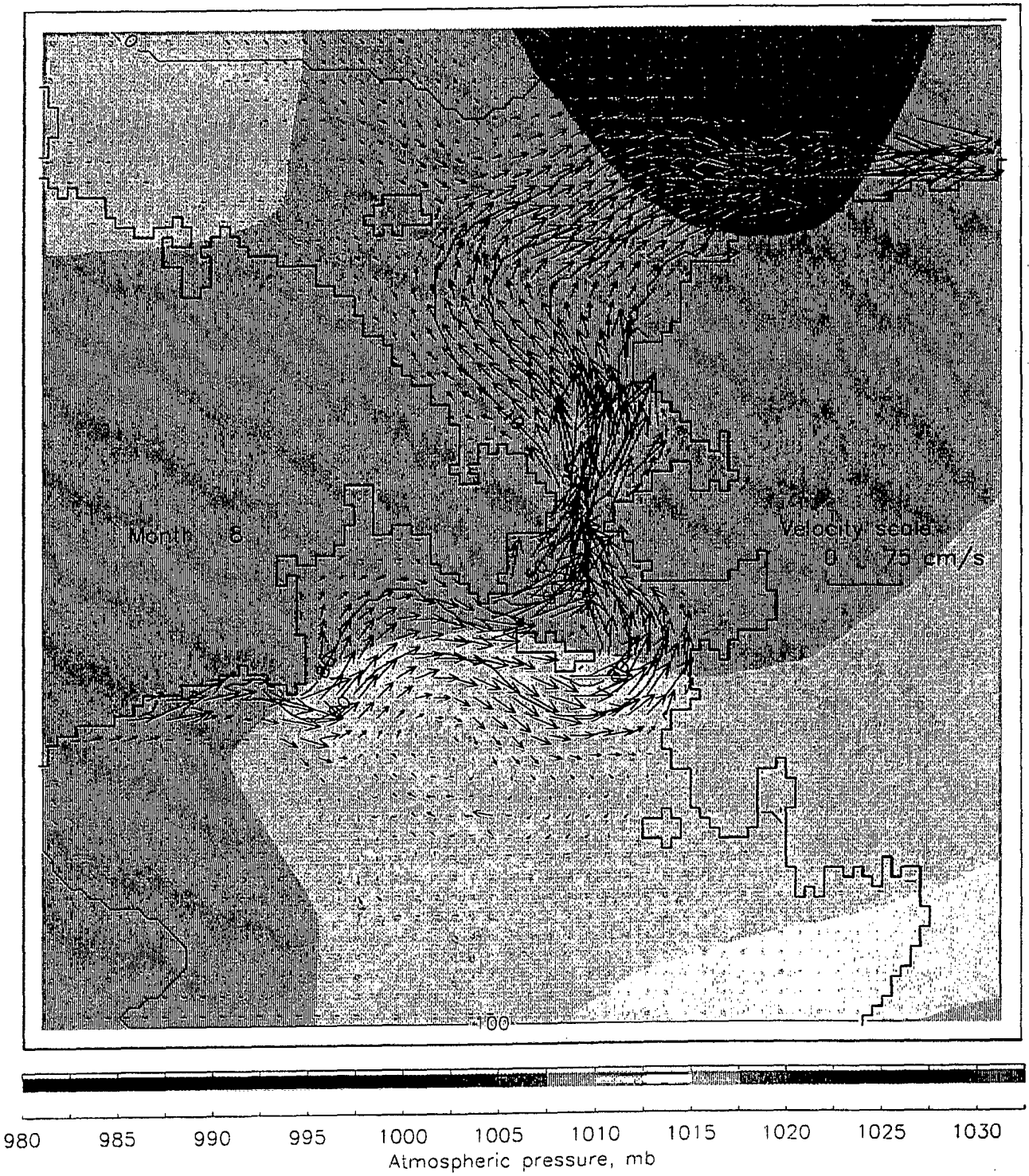

Figure 28. Mean August circulation averaged over the 15 model years using the 21 km grid.

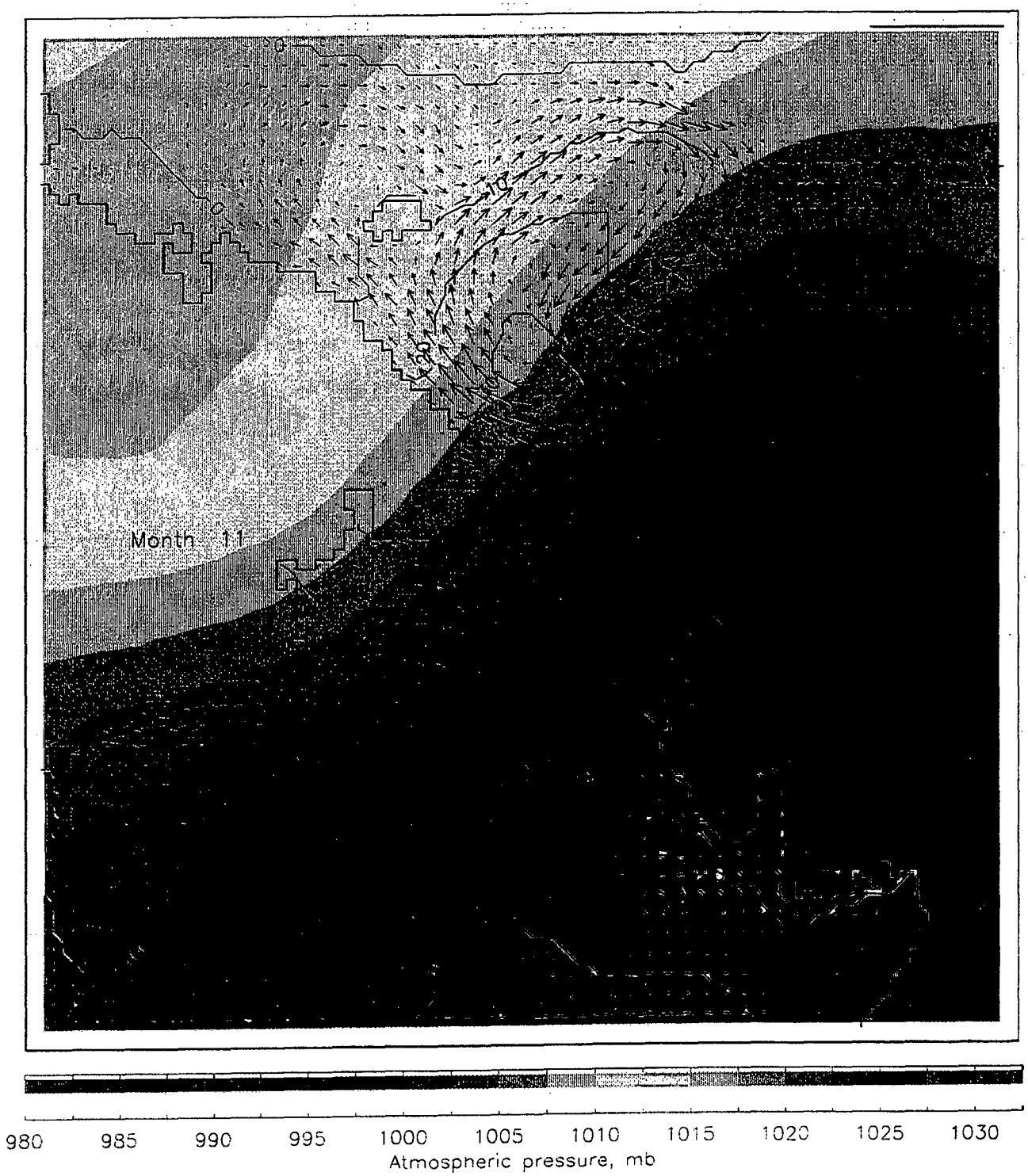

Figure 29. Mean November circulation averaged over the 15 model years using the 21 km grid.

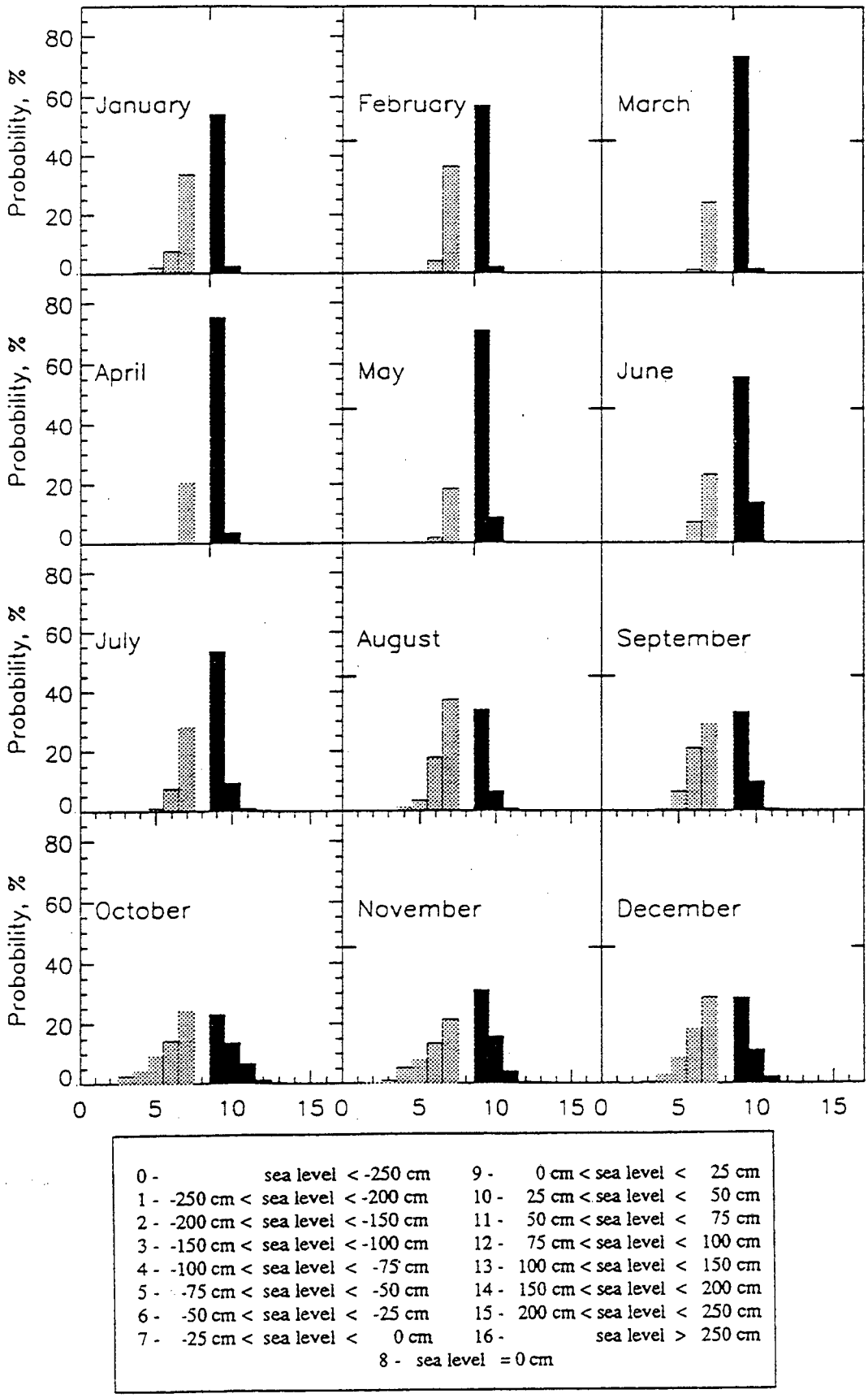

Figure 30. Histograms of coastal sea level for Point Barrow generated from the 15 year model run. Negative values (light shading) indicate a drop in coastal sea level and positive values (heavy shading) indicate an increase in sea level.

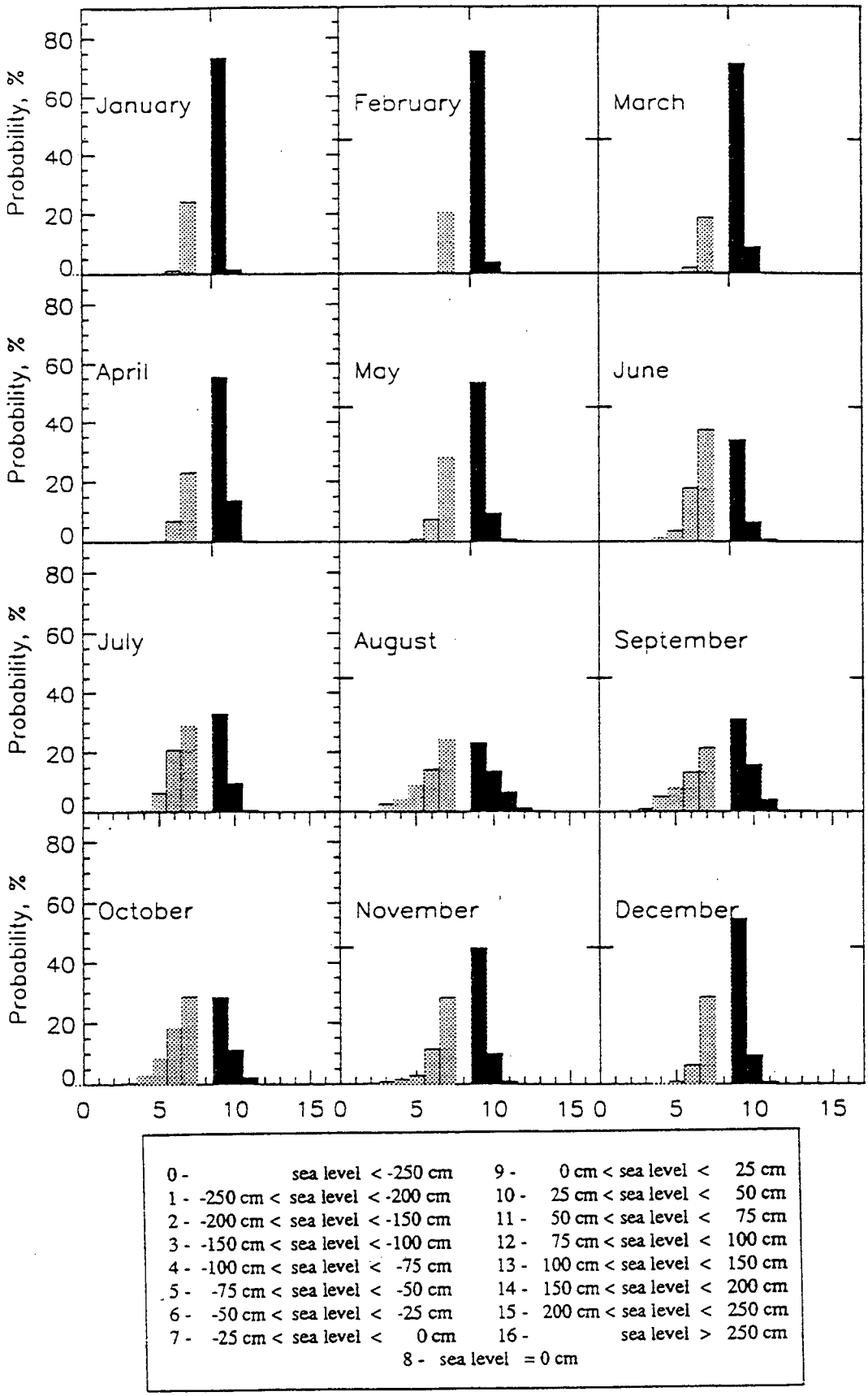

Figure 31. Histograms of coastal sea level for Point Lay generated from the 15 year model run. Negative values (light shading) indicate a drop in coastal sea level and positive values (heavy shading) indicate an increase in sea level.

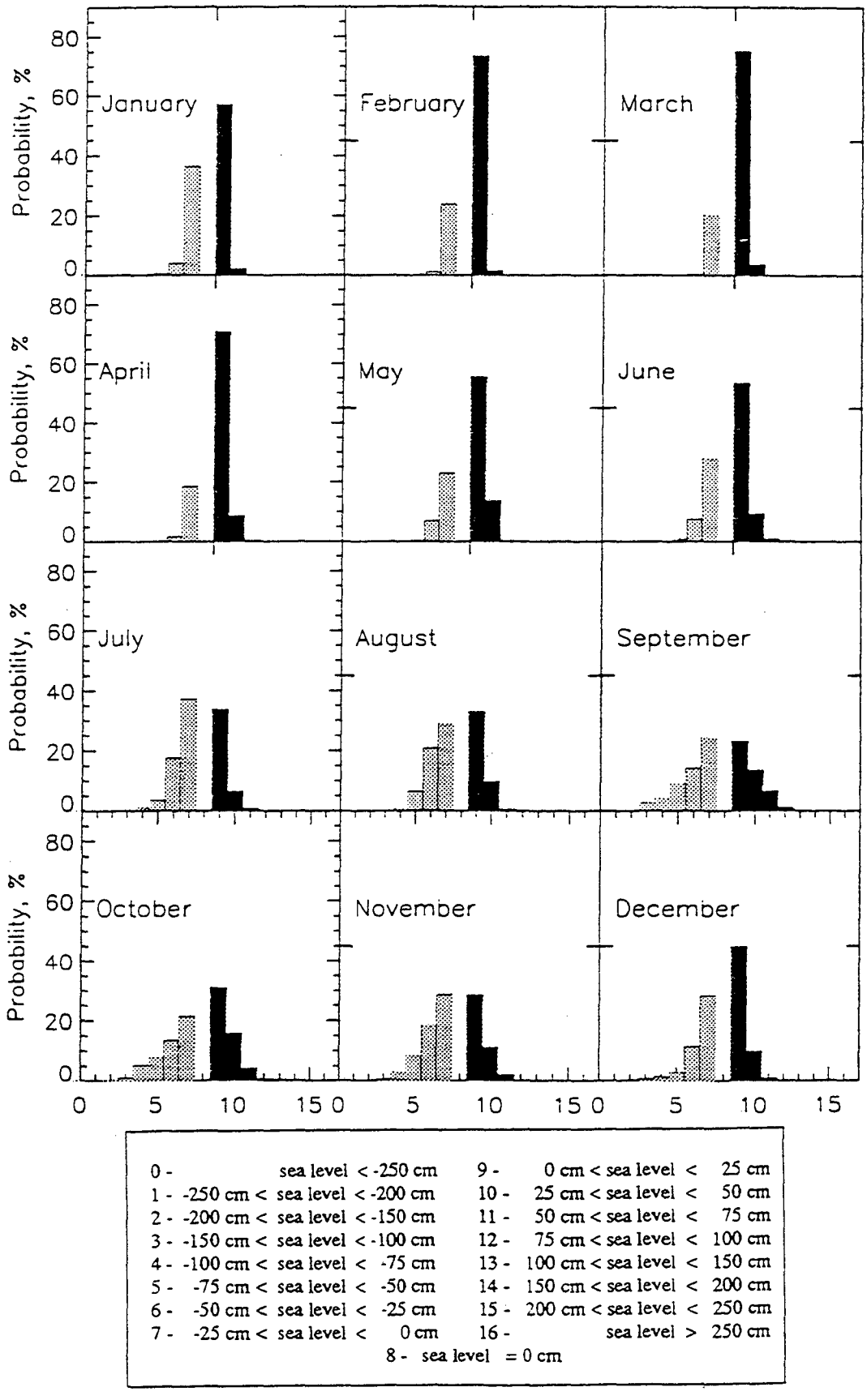

Figure 32. Histograms of coastal sea level for Point Hope generated from the 15 year model run. Negative values (light shading) indicate a drop in coastal sea level and positive values (heavy shading) indicate an increase in sea level.

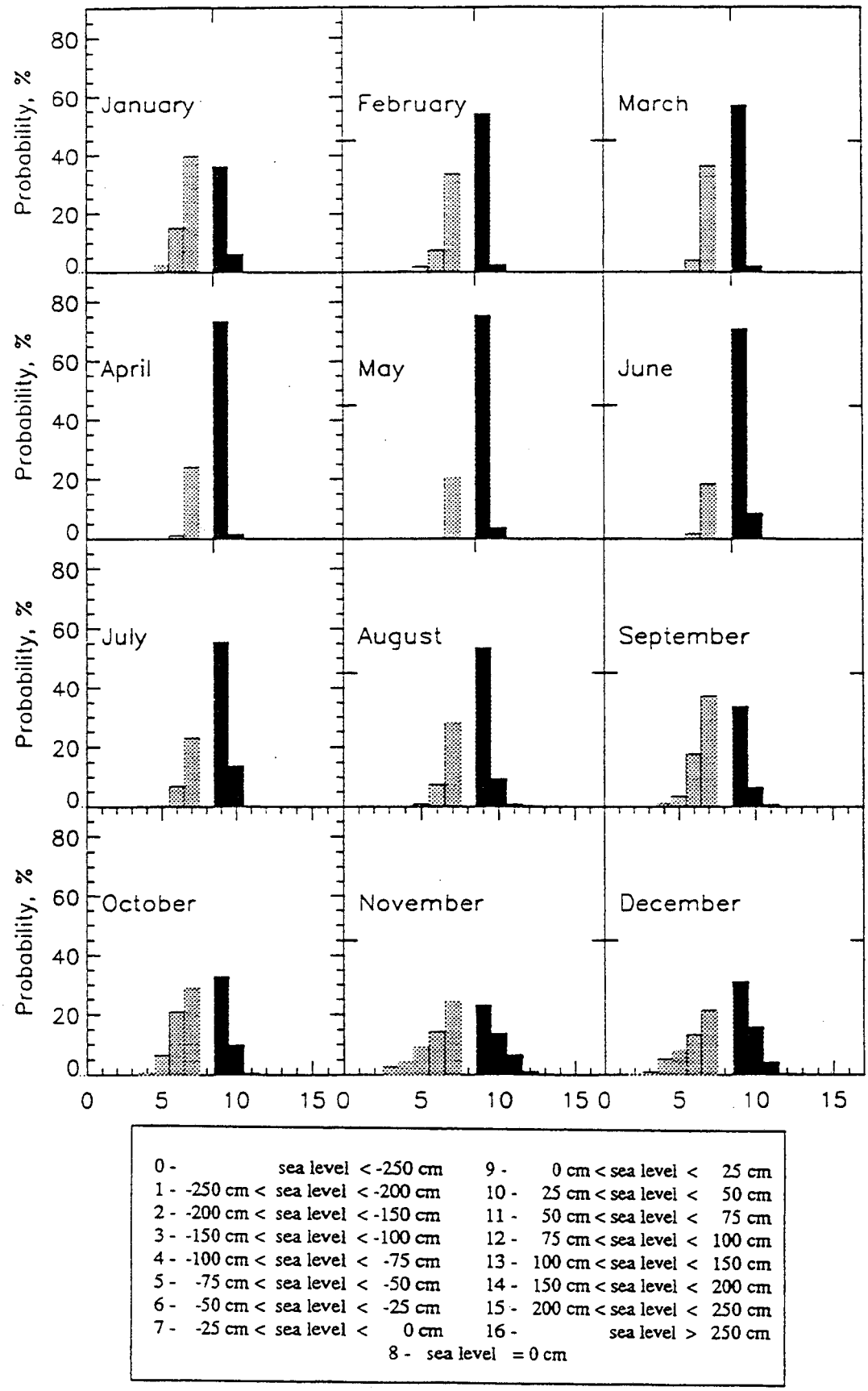

Figure 33. Histograms of coastal sea level for Kivalina generated from the 15 year model run. Negative values (light shading) indicate a drop in coastal sea level and positive values (heavy shading) indicate an increase in sea level.

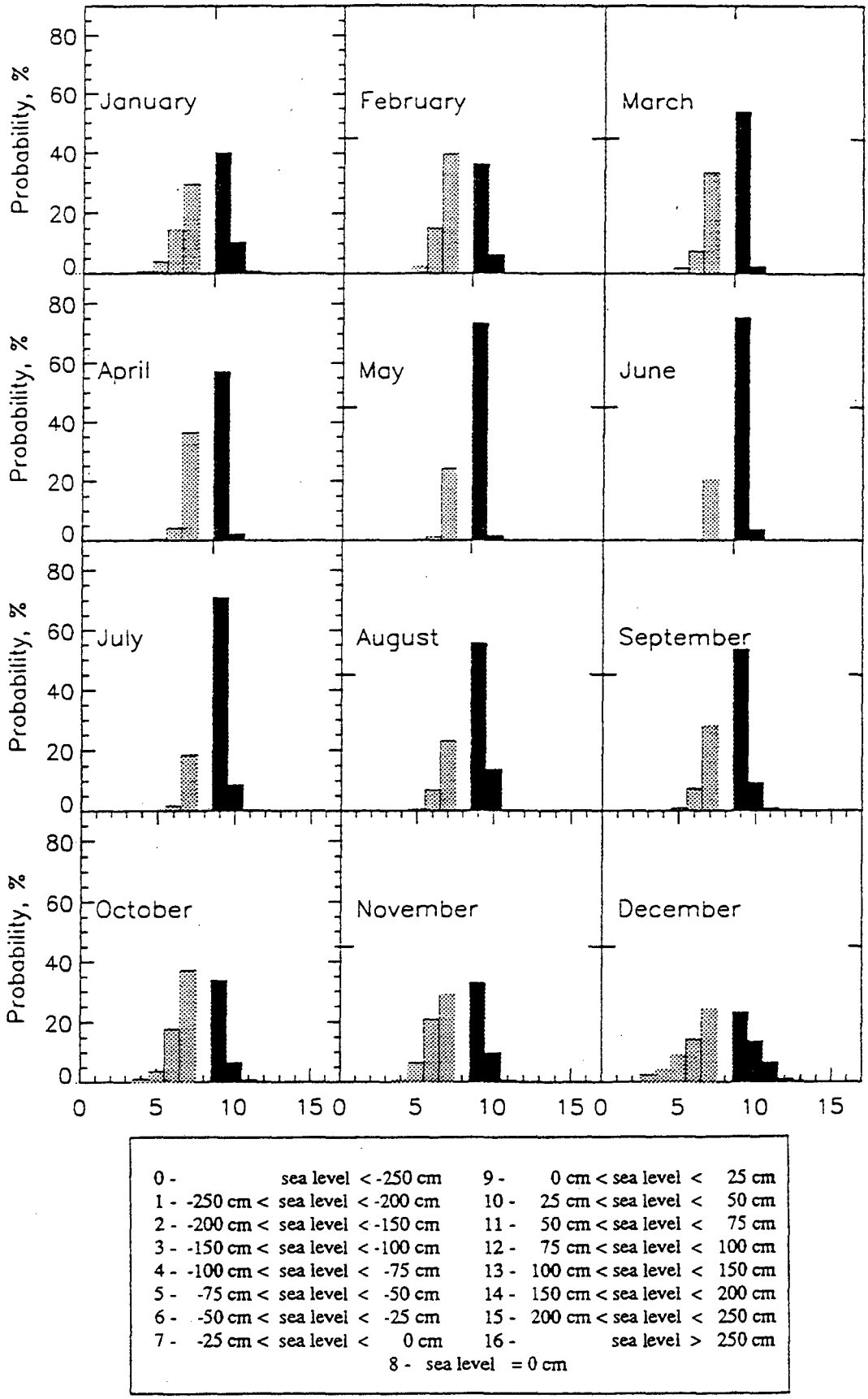

Figure 34. Histograms of coastal sea level for Shishmaref generated from the 15 year model run. Negative values (light shading) indicate a drop in coastal sea level and positive values (heavy shading) indicate an increase in sea level.

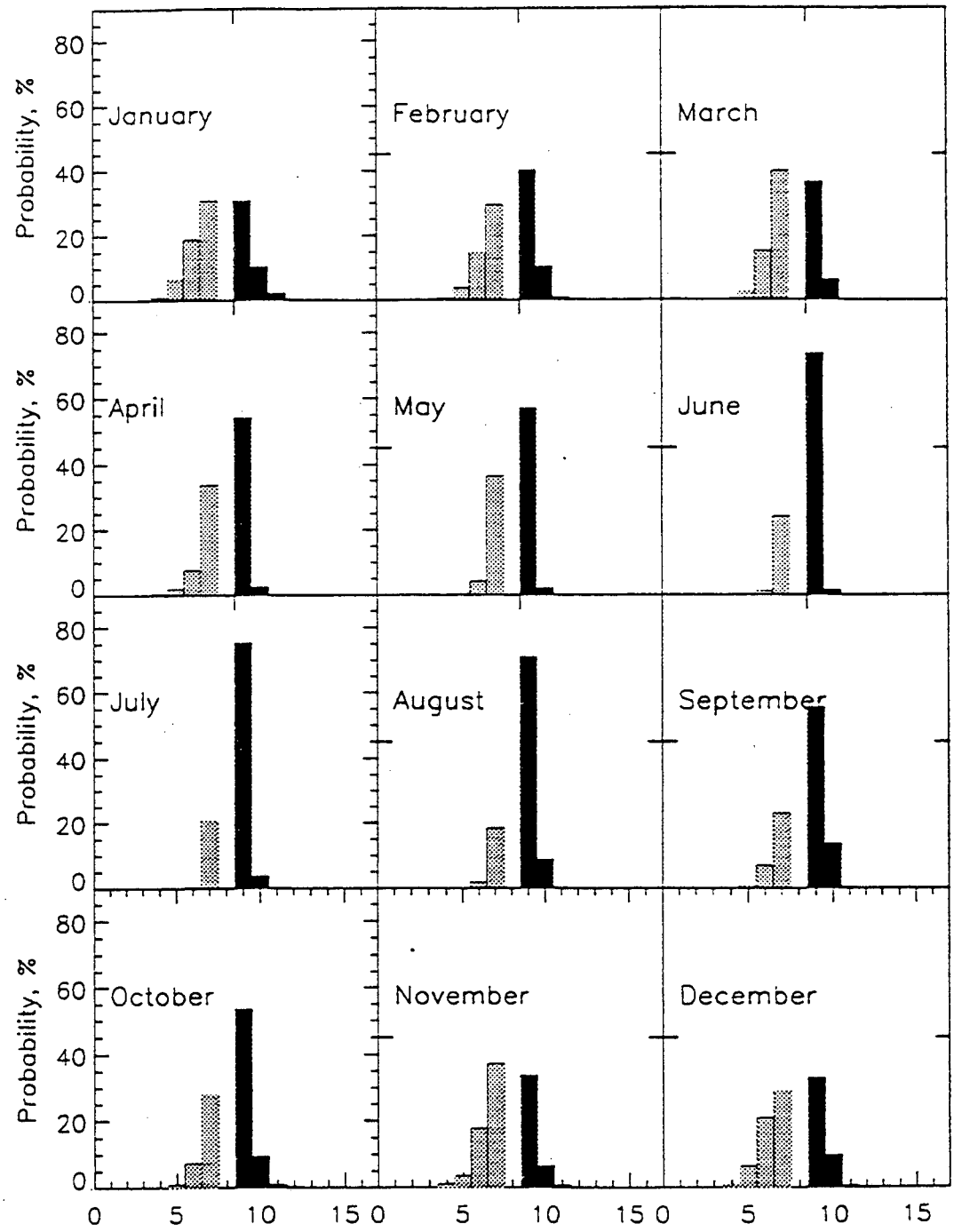

0 -	sea level < -250 cm	9 -	0 cm < sea level < 25 cm
1 -	-250 cm < sea level < -200 cm	10 -	25 cm < sea level < 50 cm
2 -	-200 cm < sea level < -150 cm	11 -	50 cm < sea level < 75 cm
3 -	-150 cm < sea level < -100 cm	12 -	75 cm < sea level < 100 cm
4 -	-100 cm < sea level < -75 cm	13 -	100 cm < sea level < 150 cm
5 -	-75 cm < sea level < -50 cm	14 -	150 cm < sea level < 200 cm
6 -	-50 cm < sea level < -25 cm	15 -	200 cm < sea level < 250 cm
7 -	-25 cm < sea level < 0 cm	16 -	sea level > 250 cm
	8 - sea level = 0 cm		

Figure 35. Histograms of coastal sea level for Wales generated from the 15 year model run. Negative values (light shading) indicate a drop in coastal sea level and positive values (heavy shading) indicate an increase in sea level.

The Department of the Interior Mission

As the Nation's principal conservation agency, the Department of the Interior has responsibility for most of our nationally owned public lands and natural resources. This includes fostering sound use of our land and water resources; protecting our fish, wildlife, and biological diversity; preserving the environmental and cultural values of our national parks and historical places; and providing for the enjoyment of life through outdoor recreation. The Department assesses our energy and mineral resources and works to ensure that their development is in the best interests of all our people by encouraging stewardship and citizen participation in their care. The Department also has a major responsibility for American Indian reservation communities and for people who live in island territories under U.S. administration.

The Minerals Management Service Mission

As a bureau of the Department of the Interior, the Minerals Management Service's (MMS) primary responsibilities are to manage the mineral resources located on the Nation's Outer Continental Shelf (OCS), collect revenue from the Federal OCS and onshore Federal and Indian lands, and distribute those revenues.

Moreover, in working to meet its responsibilities, the **Offshore Minerals Management Program** administers the OCS competitive leasing program and oversees the safe and environmentally sound exploration and production of our Nation's offshore natural gas, oil and other mineral resources. The MMS **Royalty Management Program** meets its responsibilities by ensuring the efficient, timely and accurate collection and disbursement of revenue from mineral leasing and production due to Indian tribes and allottees, States and the U.S. Treasury.

The MMS strives to fulfill its responsibilities through the general guiding principles of: (1) being responsive to the public's concerns and interests by maintaining a dialogue with all potentially affected parties and (2) carrying out its programs with an emphasis on working to enhance the quality of life for all Americans by lending MMS assistance and expertise to economic